Non-linear Magnetohydrodynamic Instabilities In Advanced Tokamak Plasmas

Rachel McAdams

Doctor of Philosophy

University Of York

Physics

September 2014

Abstract

Dwindling fossil fuel resources, and the undesirable environmental effects associated with their use in power generation, are a powerful impetus in the search for clean, reliable and inexpensive methods of generating electricity. Fusion is a process wherein light nuclei are able to fuse together, releasing large amounts of energy. Magnetic Confinement Fusion is one concept for harnessing this energy for electricity production. The tokamak reactor confines the plasma in a toroidal configuration using strong magnetic fields to minimise particle and heat losses from the plasma. However, this plasma can become unstable, resulting in loss of plasma confinement, or plasma disruption.

In particular, the instability known as the Resistive Wall Mode (RWM) is of concern for operating scenarios which are designed to optimise the fusion process, yet lie close to mode stability boundaries. The RWM is a global instability, which can cause plasma disruption. The mode is so named because it is only present when the plasma is surrounded by a resistive wall. Theoretical and experimental studies have found that plasma rotation is able to stabilise the RWM; yet in projected operating scenarios for ITER, the plasma rotation will fall below the levels found in present tokamaks. Understanding the stability of the RWM in 'advanced' scenarios is crucial, and requires non-linear physics to incorporate all the characteristics of the mode.

In this thesis, the Introduction describes the need for the development of fusion energy, and why the RWM is an important consideration in planning for future experimental programmes. The Literature Review summarises the current state of knowledge surrounding the RWM and its stability in tokamak plasmas. In Chapter 3, an analytic study of the RWM is presented. In this study, the mode is coupled to a different mode, known as the Neoclassical Tearing Mode. A system of non-linear equations describing the coupling of the modes in a rotating plasma is derived. In Chapter 4, these equations are solved for limiting solutions, and solved numerically, to show how the RWM may be responsible for an observed phenomenon called the triggerless NTM. Chapter 5 and Chapter 6 focus on simulations of RWMs. Chapter 5 describes the implementation of a resistive wall in the non-linear MHD code JOREK, carried out by M. Hölzl. This implementation is benchmarked successfully against a linear analytic formula for the RWM growth rate. In Chapter 6, initial simulations using the resistive wall in JOREK are carried out. These simulations are carried out in ITER geometry, with the resistive wall modelling the ITER first wall. Chapter 7 summarises the conclusions of the research chapters and lays out future work which could be undertaken in both analytic modelling and simulations.

Contents

List of Figures

Acknowledgements

I would like to thank my supervisors, Prof H. R. Wilson at the University of York, and Dr I. T. Chapman at Culham Centre For Fusion Energy. I would also like to express my gratitude to Matthias Hölzl, Stanislas Pamela, and Guido Huysmans for their assistance with JOREK: and also Yueqiang Liu for advice with linear RWM models. Thank you also to Michael and my family.

Declaration of Authorship

I, Rachel McAdams, declare that this thesis titled, 'Non-linear Magnetohydrodynamic Instabilities In Advanced Tokamak Plasmas' and the work presented in it are my own. I confirm that:

- This work was done wholly or mainly while in candidature for a research degree at this University.
- Where any part of this thesis has previously been submitted for a degree or any other qualification at this University or any other institution, this has been clearly stated.
- Where I have consulted the published work of others, this is always clearly attributed.
- Where I have quoted from the work of others, the source is always given. With the exception of such quotations, this thesis is entirely my own work.
- I have acknowledged all main sources of help.
- Where the thesis is based on work done by myself jointly with others, I have made clear exactly what was done by others and what I have contributed myself.

Work described in this thesis has previously been published or presented at conferences. A presentation was given at the 2012 Annual Plasma Physics Conference, Institute of Physics Conference (Oxford 2012). Posters were presented at the 39th European Physical Society Conference on Plasma Physics, Stockholm 2012, and the 55th Annual Meeting of the American Physical Society Division of Plasma Physics (Denver 2013). Results from Chapters 3 and 4 were previously published as "Resistive wall mode and neoclassical tearing mode coupling in rotating tokamak plasmas" Rachel McAdams, H. R. Wilson and I. T. Chapman, Nucl. Fusion 53(8) 083005, 2013. Results from Chapter 5 were published in "Coupling JOREK and STARWALL Codes for Non-linear Resistive-wall Simulations" M. Hölzl et al, J. Phys.: Conf. Ser. 401 012010, 2012.

Chapter 1

Introduction

1.1 Energy crisis and projections

The International Energy Agency (IEA) publishes the annual World Energy Outlook (WEO), discussing the projections for energy demand and usage. The IEA analyses the future of energy production and consumption, and the impact on the global climate of these trends.

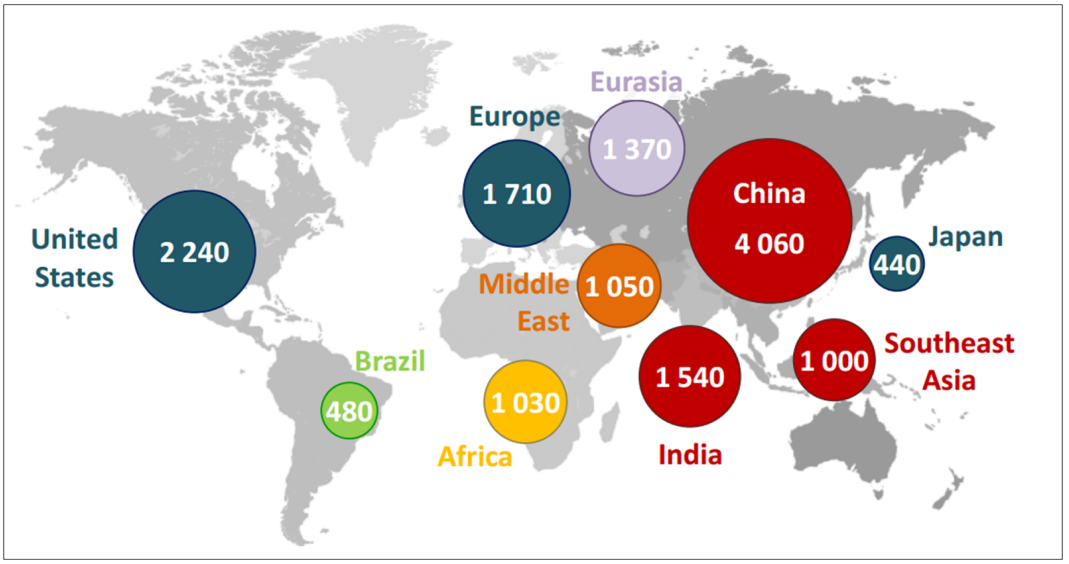

FIGURE 1.1: Primary energy demand in Mtoe (Million Tonnes Of Oil Equivalent) predictions for 2035 [1].

The WEO in 2012 [2] collected data on the global energy demand, in order to predict future consumption. Unsurprisingly, the global energy demand, as shown in Figure 1.1, is predicted to increase by over one third, from 12380 Mtoe (Million Tonnes of Oil Equivalent) in 2010 to 16730 Mtoe in 2035, as China and South Asia become the

main drivers of energy demand. This drastic increase in energy demand is necessary for the continued development of many countries, but places increasing strain on global resources.

With 82% of energy currently generated by burning fossil fuels, the necessity for governments to secure diminishing supplies of fossil fuels - and to invest in unconventional sources such as fracking for shale gas - is unavoidable. The proportion of energy generated by fossil fuels is the same as 25 years ago- and is projected to drop only as far as 75% in 2035 [1]. The growth of renewables, shown in Figure 1.2, is not sufficient to enable emancipation from traditional sources of energy production. Renewable energy sources, such as wind and solar power, may be unreliable or unable to produce energy in the required amounts to satisfy demand without usage of fossil fuels. On the other hand, nuclear power, although generally reliable, may cause concern about its environmental impact.

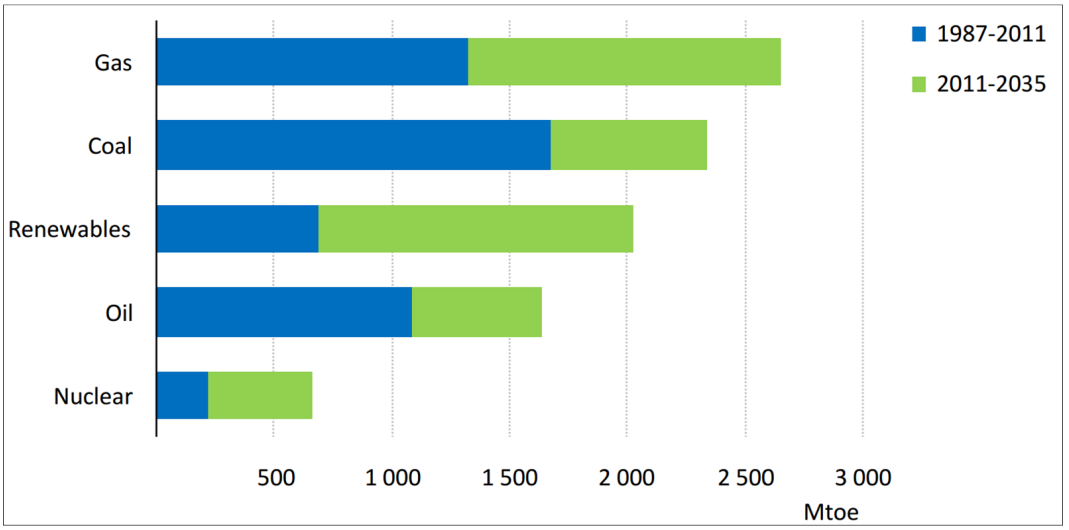

FIGURE 1.2: Predictions for growth in total primary energy demand from the World Energy Outlook 2013. Demand for fossil fuels is set to grow, but still dominates growth in renewables.

Although efforts are being made globally to increase dependence on renewable sources of energy, the growth of renewables is not sufficient to achieve emissions guidelines. Figure 1.3 shows that the remaining carbon budget, designed to restrict the global temperature rise to 2^o, is disproportionally weighted to 2012-2035.

As fossil fuels become harder to procure, it is also to be expected that energy prices will rise. The limited impact that renewable energies are predicted to make on fossil fuel dependence, and the diminished likelihood of meeting climate protection goals, imply that a new approach to energy production will be necessary.

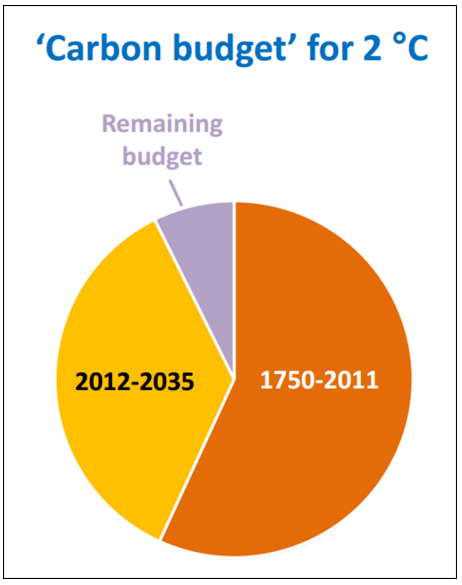

FIGURE 1.3: The carbon budget [1] shows that efforts to minimise climate change have not significantly impacted dependence on fossil fuels enough to prevent large global temperature rises.

1.2 Fusion energy

Nuclear power currently uses the fission of heavy elements to generate electricity. However, at the other end of the binding energy curve, lighter elements which fuse together release energy. The lighter the element, the more energy is released.

Fusion reactions with the lightest element, hydrogen, occur in the plasma core of the Sun, producing 3.8×10^{26}W. The amount of energy released per hydrogen fusion reaction is substantial, but fusion reactions must involve at least two hydrogen nuclei. These nuclei must overcome the Coulomb barrier (or, enough of the barrier to increase the probability of quantum tunnelling) in order to fuse together. Hence fusion reactions require the involved nuclei to acquire sufficient energy to fuse- in the Sun, the temperature in the core is over 15 million Kelvin. The fusion environment is one of the most extreme on Earth.

1.2.1 The Fusion Reaction

To achieve fusion on Earth, it is sensible to choose the fusion reaction with the highest cross-section, but at achievable energies.

Considering isotopes of hydrogen, there are several fusion reactions which are possible:

$$D^2 + T^3 \rightarrow He^4 + n^1 + 17.6 \text{ MeV} \tag{1.1}$$

$$D^2 + D^2 \rightarrow He^4 + n^1 + 3.27 \text{ MeV} \tag{1.2}$$

$$D^2 + D^2 \rightarrow T^3 + H^1 + 4.03 \text{ MeV} \tag{1.3}$$

$$D^2 + He^3 \rightarrow He^4 + H^1 + 18.3 \text{ MeV} \tag{1.4}$$

Deuterium (D^2) consists of one proton and one neutron, tritium (T^3) of one proton and two neutrons. The fusion products generally consist of an isotope of helium. The energy released in each reaction is divided between the velocities of the fusion products. The cross-sections of these reactions are shown in Figure 1.4.

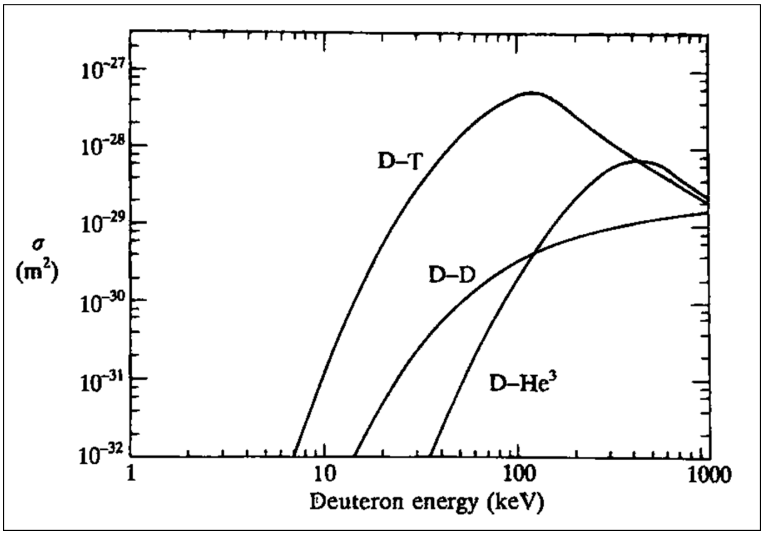

FIGURE 1.4: Cross-sections for various fusion reactions as a function of energy [3]. Both D-D reaction cross-sections are combined.

The figure shows clearly that the D-T reaction has the highest cross-section, with the peak around 100keV. The other reactions have comparable cross-sections only at much higher energies, which would be even more difficult to obtain in any sort of reactor.

Deuterium is found in 0.014-0.015% of natural hydrogen compounds, and is plentiful. Tritium, on the other hand, is rare and radioactive, with a short half-life of 12.3 years. However, the neutron produced from the preferred fusion reaction Eq. 1.1 can be used in a reaction with lithium

$$Li^6 + n^1 \rightarrow He^4 + T^3 \tag{1.5}$$

in order to produce tritium. Thus, in an operational fusion reactor, tritium can be manufactured on site.

1.2.1.1 Plasma Confinement

The plasma thermal energy W is given by

$$W = \int \frac{3}{2} k(n_e T_e + (n_D + n_T) T_I) dV \tag{1.6}$$

where k is the Boltzmann constant, $n_{e,D,T}$ the electron, deuterium and tritium number densities, and $T_{e,I}$ the electron and ion temperatures. Assuming that the plasma consists of equal densities of deuterium and tritium, and that $T_e = T_I$, then $W = 3nTV$, where $n_D = n_T = n/2$.

The power generated by the fusion reactions, P_F, is the product of the number of fusion reactions N_F, and the energy released by each fusion reaction, E_F.

$$N_F = \int n_D n_T \overline{\sigma v}(T) dV \tag{1.7}$$

where $\overline{\sigma v}(T)$ is the reaction cross-section. For the assumptions above, $P_F = n^2/4\overline{\sigma v}(T) E_F V$.

The energy balance in the plasma can be written

$$\frac{dW}{dt} = P_\alpha + P_{ext} - P_{losses} \tag{1.8}$$

where P_α is the power transferred to the plasma by the alpha particles (which are the product of fusion), P_{ext} is the external heating power provided to the plasma, and P_{losses} is the power lost from the plasma by conductive or radiative processes.

For a steady-state plasma, $dW/dt = 0$ and the power losses from the plasma can be characterised by τ_E, the plasma confinement time- the characteristic time of decrease in plasma energy: $P_{losses} = W/\tau_E$.

$Q = P_F/P_{ext}$ is the amplification factor of the plasma. $Q = 1$ is 'break-even', where the fusion power matches the external power, and the heating of the plasma can be aided by alpha particles. When $Q = \infty$, the plasma requires no external heating and is self-sustaining. For $E_{F,\alpha}$ the energy released by the fusion reaction and the energy of an alpha particle respectively,

$$n\tau_E = \frac{12kT}{\overline{\sigma v}(T)E_F\left(\frac{E_\alpha}{E_F} + \frac{1}{Q}\right)} \tag{1.9}$$

Measuring energy and temperature in keV, $E_F = 17.6\text{MeV}$, $E_\alpha = 3.6\text{MeV}$ and taking with $Q = \infty$ for a self-sustaining plasma, the Lawson criteria [4] can be derived. The cross section of the D-T fusion reaction between 10-20 keV is $\sim 1.1 \times 10^{-24}\text{T}^2\text{m}^{-3}\text{s}^{-1}$. Thus,

$$nT\tau_E = 2.6 \times 10^{21}\text{keVm}^{-3}\text{s}^{-1} \tag{1.10}$$

Achieving this value of the triple product $nT\tau_E$ is complicated by the fact that attempting to increase either n, T or τ_E may result in a deleterious effect on the other variables. Progress in fusion research can be demonstrated by the value of $nT\tau_E$ achieved in various fusion experiments. In magnetic confinement fusion, the research focus has been on increasing the confinement time τ_E.

1.3 Magnetic Confinement Fusion

Due to the high temperatures required for the fusion reaction cross-section to reach usable levels, the D-T gas will become ionised and the fusion reactions will take place within a D-T plasma. Thus material walls would be ineffectual for confinement of the plasma.

In a magnetic field, charged particles gyrate around the magnetic field line, as shown in Figure 1.5. This provides a means of confinement for the plasma particles, which are constrained (to first order) to follow the magnetic field lines.

1.3.1 Flux Surfaces

In a tokamak, the plasma is confined by the magnetic field structure. The tokamak is shaped like a torus: the magnetic field lines loop around the torus in a helical manner. The magnetic field topology is created by two field components: toroidal and poloidal.

In a conventional tokamak, the toroidal field is generated by toroidal field coils positioned around the plasma. However, the toroidal field alone is not sufficient to confine the plasma. The curvature of the tokamak, and the gradient in the magnetic field causes a tokamak with purely toroidal magnetic field to lose particles (ions and electrons), which

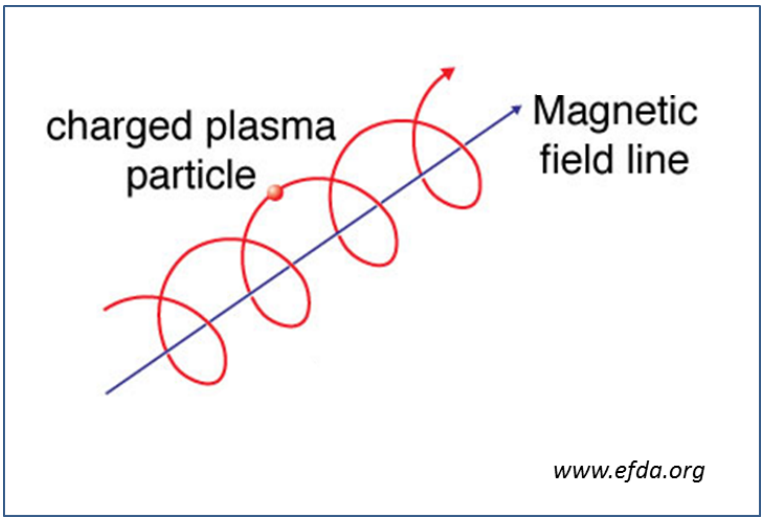

FIGURE 1.5: Charged particles in a magnetic field gyrate around the field line whilst following its trajectory. (Taken from www.efda.org)

drift out of the tokamak. By imposing a poloidal magnetic field, the drifts average to zero over one poloidal circuit of the plasma. The poloidal magnetic field is generated by a toroidal plasma current. The resultant magnetic field is shown in Figure 1.6.

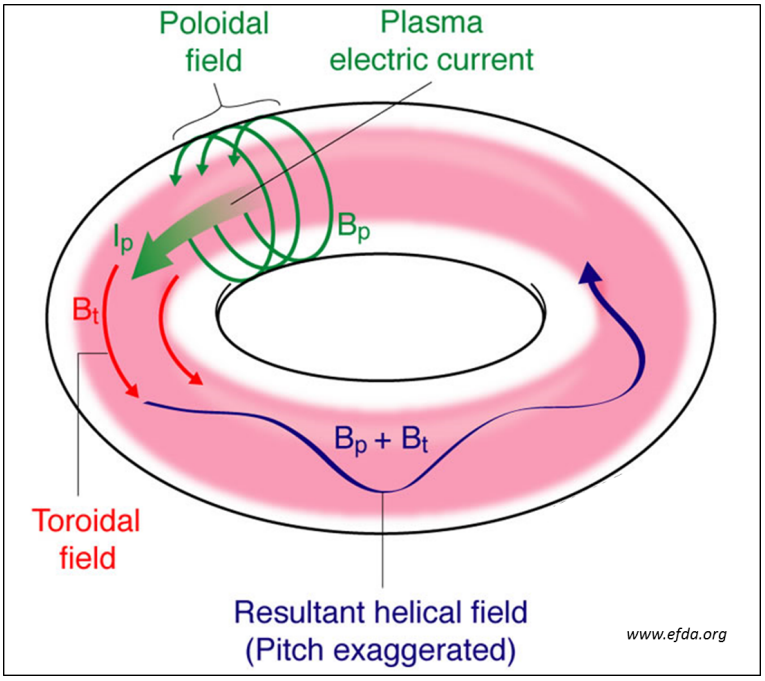

FIGURE 1.6: The combination of toroidal and poloidal magnetic fields results in nested toroidal flux surfaces, with helical magnetic field lines confined to one surface.

The topology of the magnetic field in the tokamak is a set of nested toroidal flux surfaces. The magnetic flux (and plasma pressure) is constant on each surface. Magnetic field

lines are confined to one flux surface, and trace a helical path around the tokamak on that flux surface.

A flux surface can be characterised by the amount of twist a magnetic field line has in its surface: a field line will migrate both poloidally and toroidally. The safety factor, q, is a measure of this twist. For one poloidal circuit, a field line will have travelled $\Delta\phi$, and $q = \Delta\phi/2\pi$. If the safety factor is a rational number, then the particles on that flux surface will, after the requisite number of poloidal and toroidal circuits determined by the safety factor, loop back to their starting points and retrace their paths. In this case, the safety factor can be expressed as a ratio of the number of poloidal and toroidal circuits required to return to the starting point: for example, on a flux surface where $q = 3/2$, a particle on that flux surface will have returned to its starting point after three toroidal and two poloidal circuits. A flux surface with a rational safety factor is known as a rational surface.

The plasma equilibrium is determined by the Grad-Shafranov equation, which is derived from the balance between the pressure gradient, and the cross product of the current density and magnetic field:

$$R\frac{\partial}{\partial R}\left[\frac{1}{R}\frac{\partial\psi}{\partial R}\right] + \frac{\partial^2\psi}{\partial Z^2} = -\mu_0 R^2\frac{dp}{d\psi} - f\frac{df}{d\psi} \tag{1.11}$$

where ψ is the magnetic flux function, $p = p(\psi)$ the plasma pressure, $f = f(\psi) = RB_\phi$ the toroidal field function. R (known as the the major radius, distinct from the minor radius shown in Figure 1.7), Z and the toroidal angle ϕ are shown in the tokamak geometry in Figure 1.7.

Both the plasma pressure $p(\psi)$ and the function $f(\psi)$, along with suitable boundary conditions, are necessary for solving the Grad-Shafranov equation.

Tokamak Current Drive

The toroidal plasma current, which is necessary for particle confinement, can be generated inductively or non-inductively. Inductively, it is generated by changing magnetic flux in the central column, or solenoid, which acts as a transformer. The plasma current is also the method for plasma start-up, and provides initial Ohmic heating of the plasma. However, this method cannot be sustained indefinitely, and is thus unsuited for non-pulsed operation. But toroidal plasma current can be generated non-inductively. Neutral beam injection (NBI) systems which fire energetic particles into the tokamak can drive current, as well as provide heating power for the plasma. Radio-frequency

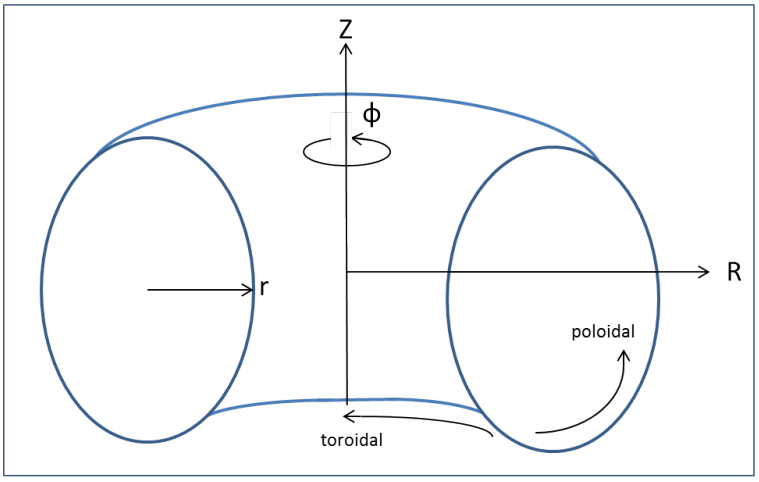

FIGURE 1.7: The geometry of the tokamak, showing the major (R) and minor (r) radii. The tokamak is often assumed to be symmetric in the toroidal direction.

radiation systems at different frequencies are also capable of driving current and heating the plasma.

The most enticing method of driving plasma current is one where the plasma generates its own currents, confining itself. The neoclassical bootstrap current [5, 6] is generated by collisions between trapped and passing particles: passing particles are those particles in the plasma which follow a helical path around the tokamak. Trapped particles have an insufficiently high ratio of parallel to perpendicular components of velocity to traverse magnetic field maxima caused by the toroidal geometry and cannot complete a full orbit. These trapped particles follow so-called 'banana' orbits. The bootstrap current is proportional to the radial pressure gradient, and the maximisation of its contribution to the plasma current would reduce both cost and complexity of a fusion reactor.

Electricity Production

The neutron, as the lighter of the two fusion products, carries 80% of the energy produced - 14.1 MeV. As the neutron is neutral, it is not held in the magnetic fields of the tokamak. As it escapes the device, a 'breeding blanket' containing lithium is able to firstly, absorb the neutron energy and create steam to drive turbines; and secondly, produce tritium in the reaction with lithium. The alpha particle, He^4, is confined in the magnetic fields, and its energy can be used to heat the plasma.

1.4 Magnetohydrodynamics In Fusion Plasmas

A plasma, as a collective movement of individual charged particles, can be studied by using kinetic theory. The distribution function of the particles can be used to investigate the individual particle movement in the plasma. However, kinetic theory is unable to capture the large scale collective behaviour of a tokamak plasma. Many of the instabilities which substantially degrade the plasma confinement stem from this collective, fluid-like behaviour.

In fact, the fluid equations are an obvious starting point for the fluid-like behaviour of a plasma - the one main difference from the treatment of a neutral fluid being the addition of a magnetic field term, and the treatment of different particle species. The magnetohydrodynamic (MHD) equations are derived from velocity moments of the Vlasov equation (in the absence of any sources and neglecting collisions):

$$\frac{\partial f}{\partial t} + (\mathbf{v} \cdot \nabla) f + \frac{1}{m}(\mathbf{F} \cdot \nabla_v) f = 0 \tag{1.12}$$

f is the particle distribution function, $\mathbf{v}$ the particle velocity, and $\mathbf{F}$ the forces on the particle [3].

1.4.1 MHD Equations

The zeroth moment of Eq. 1.12 is the continuity equation

$$\frac{\partial n_j}{\partial t} + \nabla \cdot (n_j \mathbf{u_j}) = 0 \tag{1.13}$$

$j \in \{i, e\}$ for ion and electron species, respectively. $\mathbf{u_j}$ is the flow velocity and n_j the particle density.

The first moment of the Vlasov equation is the force balance equation.

$$m_j n_j \left[\frac{\partial \mathbf{u_j}}{\partial t} + (\mathbf{u_j} \cdot \nabla) \mathbf{u_j} \right] = -\nabla p_j + n_j p_j (\mathbf{E} + \mathbf{u_j} \times \mathbf{B}) \tag{1.14}$$

for an electric field $\mathbf{E}$, a magnetic field $\mathbf{B}$, pressure p_j, and mass m_j.

It is possible to continue taking moments of the Vlasov equation indefinitely, but with each moment, the next highest moment is involved. The zeroth moment involves $\mathbf{u}$, which is solved for in the first moment. However, the first moment then introduces

the pressure p_j. The second moment is an equation for pressure, but then requires the third moment, and so on. In order to close the system, an assumption about one of the moments has to be made. Usually this assumption is about the pressure, which is assumed to be adiabatic: for the ratio of specific heats γ, the system is closed by:

$$\left[\frac{\partial}{\partial t} + (\mathbf{u_j} \cdot \nabla)\right](p_j n_j^{-\gamma}) = 0 \tag{1.15}$$

Combined with the Maxwell equations

$$\begin{aligned} \nabla \cdot \mathbf{E} &= \frac{1}{\epsilon_0}(n_i q_i + n_e q_e) \\ \nabla \times \mathbf{E} &= -\frac{\partial \mathbf{B}}{\partial t} \\ \nabla \cdot \mathbf{B} &= 0 \\ \nabla \times \mathbf{B} &= \mu_0\left[\mathbf{J} + \epsilon_0 \frac{\partial \mathbf{E}}{\partial t}\right] \end{aligned}$$

for species charge q_j and current density $\mathbf{J}$. A closed system for $\mathbf{u_j}, p_j, n_j, \mathbf{B}, \mathbf{E}$ is obtained [3].

Ideal MHD

A simplification of the MHD equations can be made with several assumptions. These assumptions may not be appropriate for all situations, but 'ideal MHD' is appropriate for time-scales much larger than the ion cyclotron times, and length scales much larger than the ion gyro-radius.

Ideal MHD assumes the plasma is a single fluid, combining electrons and ions, and neglects all dissipative effects such as resistivity, viscosity, and any other collisional effects.

With the addition of Ohm's Law

$$\mathbf{E} + \mathbf{u} \times \mathbf{B} = 0 \tag{1.16}$$

the ideal MHD equations are

$$\begin{aligned}
\frac{\partial \rho}{\partial t} + \nabla \cdot (\rho \mathbf{u}) &= 0 \\
\rho\left[\frac{\partial \mathbf{u}}{\partial t} + (\mathbf{u} \cdot \nabla)\mathbf{u}\right] &= -\nabla p + \mathbf{J} \times \mathbf{B} \\
\frac{\partial p}{\partial t} + (\mathbf{u} \cdot \nabla)p &= -\gamma p \nabla \cdot \mathbf{u} \\
\nabla \times \mathbf{B} &= \mu_0 \mathbf{J} \\
\frac{\partial \mathbf{B}}{\partial t} &= -\nabla \times \mathbf{E}
\end{aligned}$$

1.4.2 MHD Instability

Ideal MHD can be used to analyse the (linear) stability of a plasma. The ideal MHD equations are perturbed and linearised. The perturbation can be expressed as a displacement ξ.

The stability of the plasma is found by examining the plasma energy ∂W. If $\partial W > 0$ for all displacements, then the plasma is stable. If $\partial W < 0$ for any displacement ξ, then the plasma is unstable. Marginal stability corresponds to $\partial W = 0$.

∂W is comprised of three components: plasma, vacuum, and surface terms. The vacuum component is always stabilising.

The plasma component ∂W_p can be further decomposed into five terms [3]:

$$\partial W_p = \frac{1}{2}\int d^3\mathbf{x}\left[\frac{|B_1^2|}{\mu_0} + \frac{B^2}{\mu_0}|\nabla\cdot\xi_\perp + 2\xi_\perp\cdot\kappa|^2 + \gamma p_0|\nabla\cdot\xi|^2 - 2(\xi_\perp\cdot\nabla p)(\kappa\cdot\xi_\perp^*) - \mathbf{B_1}\cdot(\xi_\perp\times\mathbf{b})\mathbf{j}_{||}\right] \tag{1.17}$$

for κ the curvature vector, $\mathbf{b}$ the unit magnetic field vector. The equilibrium and perturbation quantities, are differentiated by the subscripts 0 and 1. Vector quantities are decomposed perpendicular and parallel to the magnetic field lines.

The first three terms correspond to the field line bending, magnetic field compression and plasma compression contributions. These are always stabilising. The field line bending term is minimised around flux surfaces with a rational safety factor - hence MHD instabilities are often localised around rational surfaces. The fourth term is the driving term for pressure-driven instabilities, and the fifth term the driving term for current-driven instabilities. The instabilities considered in this thesis are current-driven.

Ideal And Resistive Modes

In ideal MHD, the plasma is assumed to be ideal and have no resistivity. This assumption leads to a significant conclusion: that the plasma and the magnetic field are 'frozen' together.

The magnetic field lines and the plasma must evolve in order to conserve flux. This implies that a change of magnetic topology is not permitted. Magnetic field lines cannot break and reconnect in an alternate configuration.

If the plasma is permitted to be resistive, then the magnetic field lines can break and reconnect in a different topology. Additional MHD instabilities are then possible. Instabilities in ideal MHD tend to be the fastest growing and most violent MHD instabilities, but resistive MHD instabilities usually grow much more slowly and on timescales which allow for active feedback and mitigation. Tearing modes are resistive MHD instabilities localised at a rational flux surface.

Internal And External Modes

MHD instabilities can also be categorised by their effect on the plasma boundary. Internal modes are only present inside the plasma, and the plasma boundary remains stationary. External modes also affect the boundary of the plasma, which can be distorted. For example, the external kink distorts the flux surfaces and requires motion of the boundary.

1.5 ITER

The next-step international fusion device, ITER [7], being constructed in the south of France aims to achieve a net output of fusion power. The success of ITER is vital for the future of fusion power.

ITER will have a tokamak chamber volume eight times that of any previous tokamak, a major radius $R = 6.21$m and a minor radius of $r = 2.0$m, and a schematic is shown in Figure 1.8. ITER will make significant progress towards the necessary value of the fusion triple product (Eq. 1.10), as in Figure 1.9.

The dual aims of ITER [8] are, firstly, to demonstrate an amplification factor of $Q \geq 10$ for a range of operational scenarios, over a sufficiently long duration; and secondly, to demonstrate steady-state scenarios with non-inductive current drive for $Q \sim 5$. In order to achieve these goals, ITER will have to produce plasma dominated by alpha particle

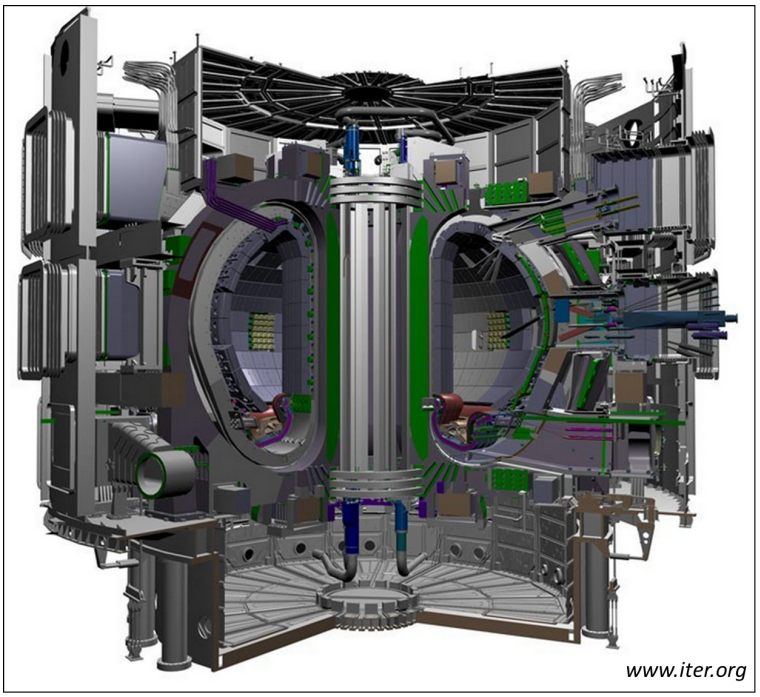

FIGURE 1.8: ITER will be the largest magnetic confinement fusion device, currently to begin operations in 2020

heating. ITER also offers the opportunity to investigate reactor technologies, such as the blanket for breeding tritium, divertor technologies for exhaust removal, and improved neutral beam technology.

The baseline ITER operating scenario is H-mode [9]- a mode where confinement is improved by a large pressure gradient at the edge of the plasma. This is projected to achieve $Q = 10$ from current scaling laws, and satisfy the first aim of ITER, but is not capable of providing a substantial proportion of non-inductive current.

1.5.1 ITER Advanced Scenarios

Advanced scenarios [10, 11] are designed to maximise the non-inductive current in the plasma. Non inductive current can be driven by neutral beam particle injection, radio frequency radiation systems or the self-generated plasma current known as the bootstrap current [5]. Advanced tokamak scenarios generally have a range of non-monotonic q profiles, as shown in Figure 1.10, with magnetic shear $s = (r/q)dq/dr$ often negative in the core of the plasma.

There are two main types of advanced scenario: 'steady state' and 'hybrid'. Steady state scenarios [12–15] are designed to reach the second goal of ITER, achieving $Q \geq 5$ with fully non-inductive current. These discharges typically have reversed shear safety factor

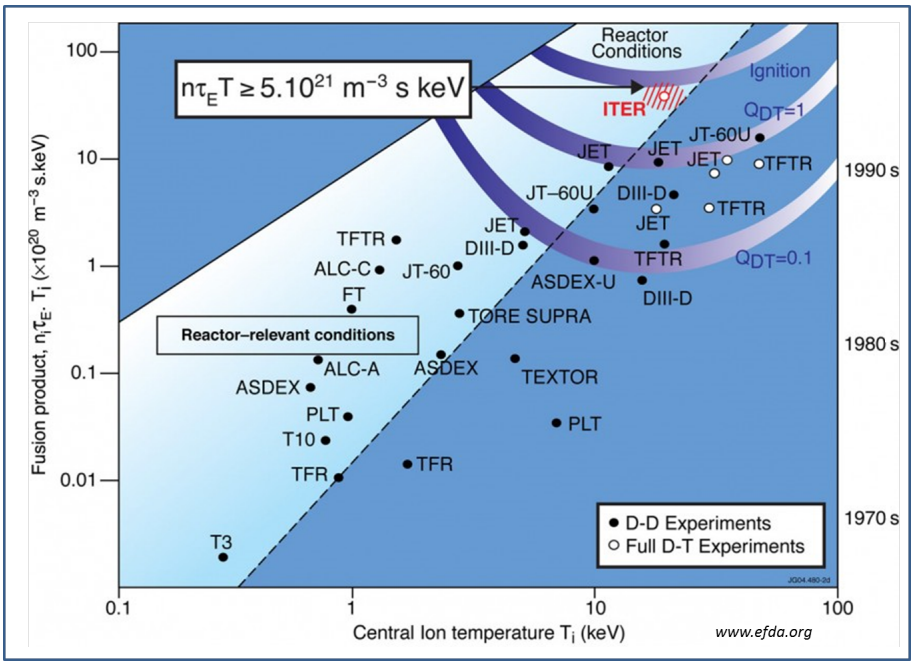

FIGURE 1.9: Throughout the fusion programme, the value of the triple product (Eq. 1.10) has increased towards the goal of ignition. ITER is predicted to achieve conditions close to those required in a reactor.

profiles in the core of the plasma, which lead to the formation of internal transport barriers (ITBs) [16], improving confinement. The ITBs allow sufficient generation of bootstrap current [17] for non-inductive current drive. Reversed shear safety factor profiles are formed transiently by hollow current density profiles, where current is driven off-axis. Positive reinforcement after formation of the ITB can sustain the q profile, as the local bootstrap current is driven more strongly locally, maintaining the negative magnetic shear. In hybrid scenarios, the safety factor profile is very flat and has very weak, or zero, magnetic shear in the core of the plasma [18–20]. The hybrid scenario is not expected to be steady state but operates at a lower plasma current than the ITER baseline scenario, with weaker ITBs than the advanced steady state scenario [21].

The fusion power P_F scales with the plasma pressure squared [7]. The ratio of plasma pressure to magnetic field pressure is characterised by the parameter $\beta = \langle p \rangle / B_T^2 / 2\mu_0$, where $\langle\rangle$ signifies a plasma-averaged quantity. Optimising the plasma pressure for a given magnetic pressure is essential for power generation. Comparisons between machines are often made in terms of $\beta_N = \beta(\%) a B_T / I_p$ where B_T is the toroidal magnetic field, I_p the plasma current in MA, a the plasma minor radius and p the plasma pressure. Maintaining plasma performance at a lower, non-inductive plasma current means operating at a higher β_N. However, this implies that advanced scenarios, which have by necessity strongly peaked plasma pressure, will be operating near MHD stability limits. External kinks driven by steep local pressure gradients and associated strong current

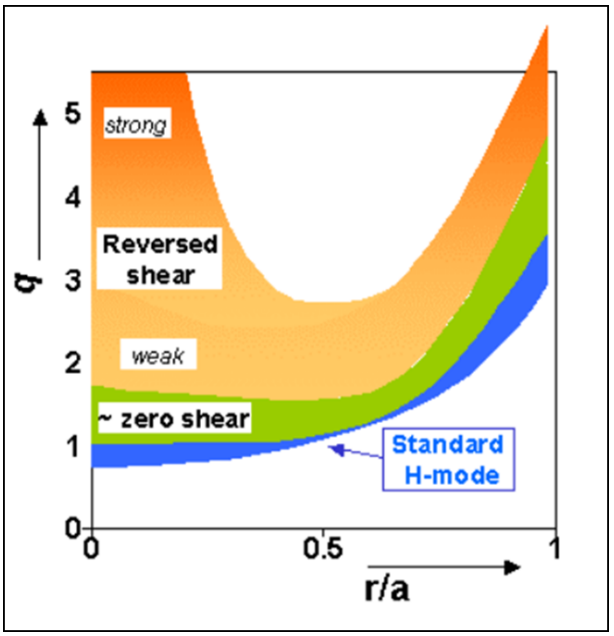

FIGURE 1.10: A wide range of q profiles can be obtained in the tokamak. Profiles with reversed magnetic shear in the core of the plasma are associated with advanced scenarios of operation[11]

density can be destabilised. Kink stability limits achievable β_N in a reactor, and hence the fusion performance. Figure 1.11 shows an external kink mode in JET [22], mapped by the soft x-ray signals. Figure 1.11a) shows the plasma discharge through phase space: the plasma crosses the no-wall beta limit and moves towards the ideal wall-wall limit. This destabilises the external kink mode, the reconstruction of the soft x-ray emissions profile is in Figure 1.11b) compared to ideal MHD calculations in c).

The external kink is destabilised when $\beta_N > 4l_i$, in the absence of a resistive wall, where l_i is known as the plasma inductance, and $4li_i$ is often used as an experimental proxy for the external kink stability limit. The stability limit is measured by the plasma β_N: if a plasma has no surrounding wall, then the β_N at which the external kink becomes unstable is known as the no-wall limit. If the plasma is surrounded by a superconducting wall, then the external kink can be stabilised over a wider range of β_N by bringing the superconducting wall sufficiently close to the plasma. This raises the stability limit to the ideal-wall limit: $\beta_N^{ideal-wall} > \beta_B^{no-wall}$. If the wall is resistive, then an unstable mode is still present and is known as the Resistive Wall Mode [23]. The mode is unstable for β_N greater than the no-wall limit, but the presence of the resistive wall slows its growth to a rate dependant on the resistivity of the wall. Reversed shear plasmas have a plasma inductance of $l_i \sim 0.8$, severely limiting the achievable β_N.

Fig 1.12 shows experimental progress in reversed shear scenarios- $H_{89}\beta_N/q_{95}^2$ is a measure of plasma performance, with ITER reference scenarios' performances indicated [11]. H_{89}

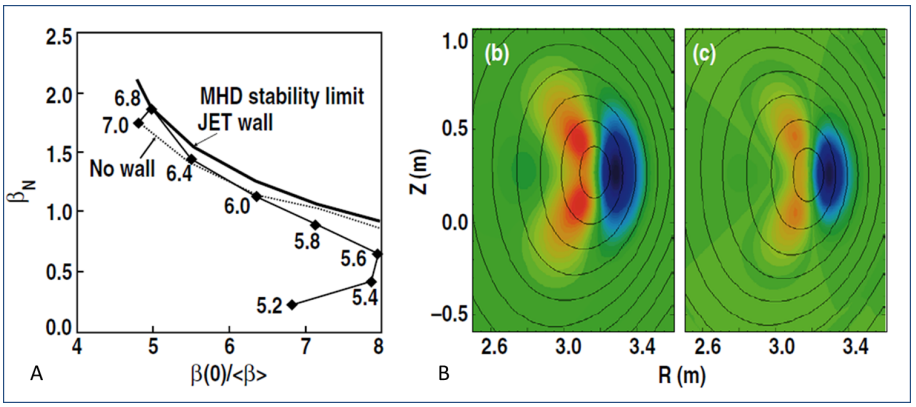

FIGURE 1.11: External kink mode in JET. A shows the plasma stability evolution; whilst B shows the n=1 perturbation reconstructed from the SXR profile [22].

is the confinement enhancement factor, relative to scaling laws detailed in [7]. Transient discharges are often able to achieve performance greater than ITER scenarios, which cannot be maintained for sufficiently long periods of time. Pulse durations on the time scale of ITER have yet to be achieved (ITER would be $110/\tau_E$ on this scale), as duration of pulse is limited by machine capabilities (heating systems etc).

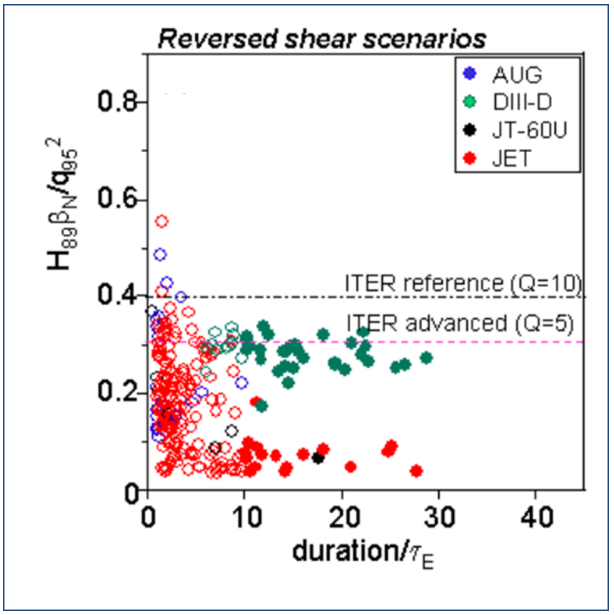

FIGURE 1.12: Collated experimental data from reversed shear scenarios shows that ITER performance can be reached by current tokamaks for short durations. Longer duration ITER-like discharges remain elusive [11].

Figure 1.13 shows that for increased pressure peaking, the maximum attainable β_N is decreased [22]. 80% of the reversed shear scenarios achieved this performance only transiently.

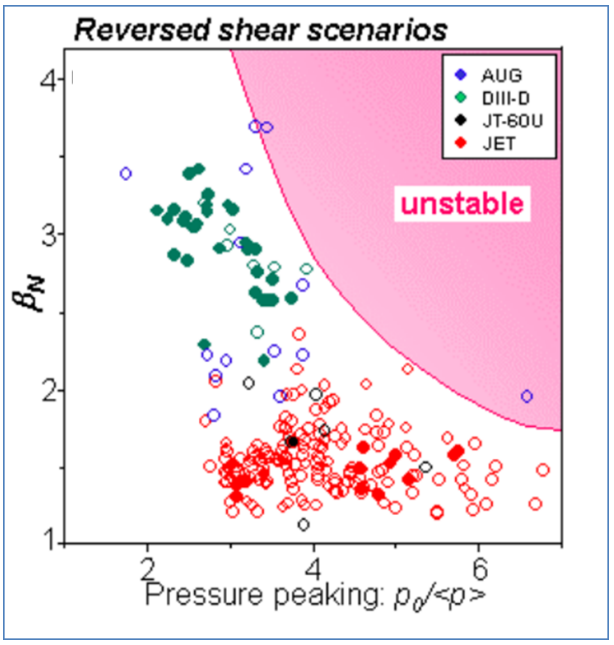

FIGURE 1.13: Worldwide experimental data indicated that MHD instability to external kinks, driven by peaked pressure, severely limits the achievable β_N. [11]

Clearly, in order to operate a fusion reactor with non-inductive current and yet optimise fusion power by maximising β, a method of routinely obtaining discharges above the no-wall beta limit in order to avoid external kinks and resistive wall modes, is necessary.

1.6 Scope Of The Thesis

Initially, this project was intended to focus only on the large scale computer simulation of non-linear magnetohydrodynamic instabilities, more specifically, the Resistive Wall Mode. This was to be carried out using the non-linear code JOREK, coupled to the wall code STARWALL, as described in Chapter 5. At the beginning of the project, the process of coupling JOREK to STARWALL, carried out by my collaborators at IPP Garching, was not yet complete. Whilst waiting for the code to become available, I began an analytical investigation into the non-linear analytical coupling of resistive wall modes and neoclassical tearing modes, prompted by experimental observations of so-called trigger-less neoclassical tearing modes. This investigation displayed complex behaviour, and grew into a substantial piece of work in its own right. The analytical model and the conclusions drawn from the solutions are described in Chapters 3 and 4. Once the JOREK-STARWALL coupling was completed, I was invited to take part in benchmarking the coupled code with respect to the instability which I intended to investigate: the resistive wall mode. This benchmarking is detailed in Chapter 5. Simulations of resistive wall modes in ITER-like scenarios were performed: but due to time

restrictions for the completion of this thesis, simulations which investigate the behaviour of neoclassical tearing modes in the RWM-unstable plasma were not able to be included in Chapter 6. Further work would investigate the inclusion of NTMs in these simulations in order to expand the analytical work.

Chapter 2

Literature Review

2.1 Resistive Wall Modes In Tokamak Plasmas

One of the main magneto-hydrodynamic instabilities limiting the achievable β in tokamak plasmas - particularly advanced scenario plasmas - is the external n=1 kink mode, with n the toroidal mode number [10]. The external kink is an ideal MHD mode with global structure, which results in significant plasma displacement at the boundary of the plasma.

2.1.1 Resistive Walls

For an external MHD mode, the plasma boundary is displaced. The flux perturbation associated with the instability extends beyond the plasma boundary into the vacuum region outside the plasma. The presence of an external wall thus has some effect on any external flux perturbation intercepted by the wall.

For an ideal (superconducting) wall, the magnetic flux is unable to diffuse through the wall. This has the effect of 'pinning' the flux perturbation to the wall boundary and providing stabilisation for the mode, as shown in Figure 2.1.

However, tokamak plasmas are not surrounded by superconducting walls. Current walls have finite resistivity. Resistive walls are somewhat stabilising, as some magnetic flux is still able to permeate the wall. This change in boundary conditions causes the growth rate, and the marginal stability of the mode, to change.

It has been found numerically [24] that the tokamak operational envelope was limited by a value of $\beta_N = 2.8$. Above this limit, the plasma was found to be unstable. This limiting

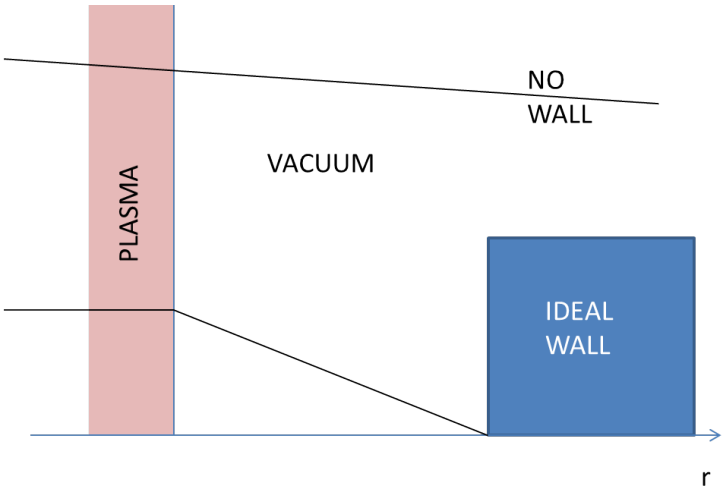

FIGURE 2.1: An ideal wall prevents flux perturbations diffusing through it, providing stabilisation for the mode.

β_N was calculated with the assumption of no external conducting wall. In a steady-state reactor, any wall stabilisation would be ineffective over the discharge lifetime. Experimentally, the β_N limit, shown in Figure 2.2, was found to be $\beta_N^{exp} \sim 3.5$ [25], indicating that the external wall does exert a stabilising influence in current tokamak discharges.

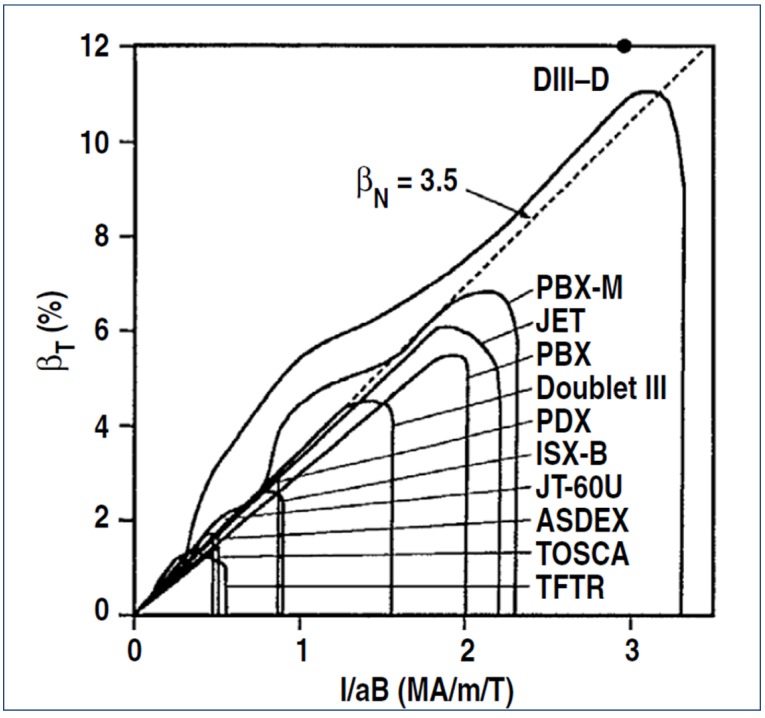

FIGURE 2.2: Comparison of experimental β_T with normalised current. The operational envelope is bounded by $\beta_N = 3.5$ [26]

The radius of the wall location is also crucial in the mode stability. If the plasma, subject to an external kink, is surrounded by a wall at infinity (or sufficiently far from the plasma that it is perceived to be 'at infinity'), then the external kink is unstable for $\beta_N > \beta_N^{no-wall}$. $\beta_N^{no-wall}$ is the stability boundary for the external kink. If an ideal wall is brought towards the plasma, then at a certain radius, the external kink will be stabilised and the stability boundary is raised such that the plasma is additionally stable for $\beta_N^{no-wall} < \beta_N < \beta_N^{ideal}$. The situation is illustrated in Figure 2.3.

Consider now a (non-rotating) plasma which has finite resistivity. It has been proven [27] that any MHD unstable plasma configuration with dissipation-less plasma, surrounded by a vacuum and possibly superconducting walls, cannot be stabilised by adding walls of finite resistivity around the plasma. The growth rate of the mode can only be reduced to τ_w^{-1}, where τ_w is the characteristic time scale for the magnetic flux to diffuse through the wall. This time scale is derived in Section 3.3.1. In DII-D, τ_w is found experimentally to be $5 - 7$ms [28]. Typically, the growth rate without a wall is on the time-scale of the much faster Alfvèn time τ_A.

The Resistive Wall Mode (RWM) is the branch of the external kink instability which is excited when the plasma is surrounded by a wall of finite resistivity, and is **unstable** for $\beta_N^{no-wall} < \beta_N < \beta_N^{ideal}$. Like the external kink, it is a global mode, which additionally has a low frequency. As discussed in Chapter 1, the RWM is likely to be destabilised for advanced tokamak scenarios which need to operate at high β_N, with peaked pressure profiles.

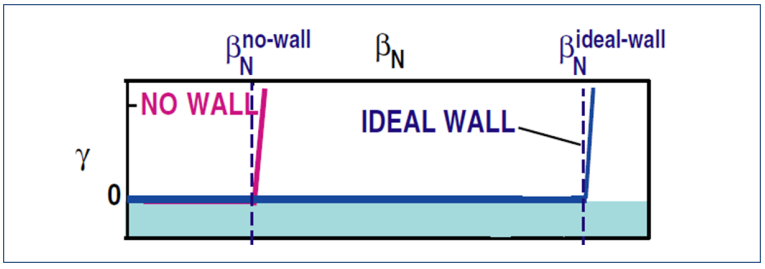

FIGURE 2.3: [29] Stability limits for external kink.

2.2 RWM Dispersion Relation

A useful treatment of the Resistive Wall Mode is using the variational method to derive the dispersion relation for the mode, which can be used to track the mode stability as the boundary conditions are changed. This is demonstrated by Haney and Freidberg in [30]. The derivation of the results is shown in more detail in Appendix A. The dispersion relation

$$\gamma\tau_w = -\frac{\partial W_\infty}{\partial W_b} \tag{2.1}$$

is found, where γ is the (complex) growth rate of the mode, ∂W_∞ is the plasma energy with an ideal wall at infinity, ∂W_b is the plasma energy with the ideal wall at a finite radius sufficient to stabilise the mode, and τ_w is the characteristic time taken for magnetic flux to penetrate the resistive wall.

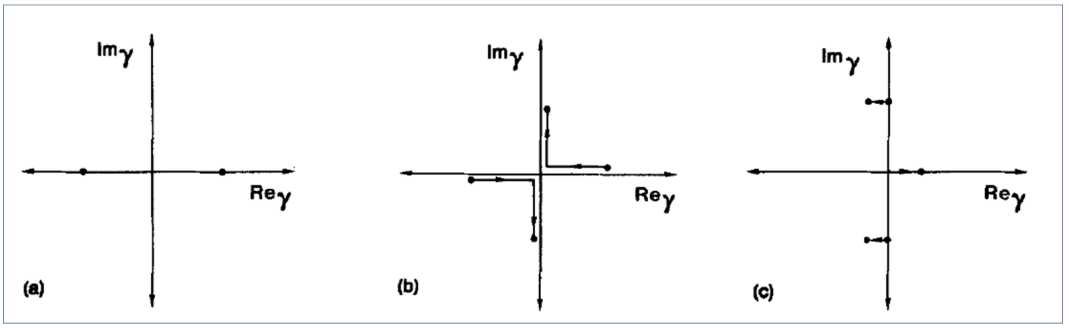

FIGURE 2.4: The spectral plots for a) wall at infinity, b) ideal wall at a finite distance and c) a resistive wall at the same location [30]

The obtained spectral plot is shown in Figure 2.4 [30]. The plots show the mode eigenvalues on the complex plane. Figure 2.4a) predicts two solutions for a wall at infinity (designated by dots on the plot). One of the solutions is an ideal instability, with $Re(\gamma) > 0$. The second solution is a stable mode, with $Re(\gamma) < 0$. In Figure 2.4b), the addition of the ideal wall sufficiently close to the plasma (at a finite radius) moves the eigenvalues on the complex plane from the real axis to the imaginary axis (shown by the directed line on the plot). For the formerly unstable solution in a), $Re(\gamma)$ is now zero, and the mode is at marginal stability. The stable mode is also brought to marginal stability by the addition of the ideal wall. Figure 2.4c) shows the effects if the ideal wall is replaced by a resistive wall. The two ideal wall-stabilised modes are now damped, and move away from purely imaginary solutions on the imaginary axis. However, a new third solution is found which is shown moving from the origin along the positive real axis. This is the Resistive Wall Mode.

2.3 Experimental Resistive Wall Modes

This section will introduce the relationship between the RWM and the rotation of the plasma, as demonstrated by an experimentally observed RWM in DIII-D, shown in 2.5 and described below.

2.3.1 Resistive Wall Modes And Plasma Rotation

The RWM has a complex, non-linear relationship with the plasma rotation, and RWM theory has centred around rotational stabilisation in dissipational plasmas in many models. If the wall surrounding the plasma is ideal, then due to the conservation of flux in an ideal medium, the perturbed magnetic flux cannot penetrate the ideal wall. If the wall is resistive, the flux is then able to penetrate the wall. However, if the plasma and the resistive wall can be made to rotate relative to each other, any single location on the wall will experience a constantly changing phase in the perturbed magnetic flux. The magnetic flux does not have the opportunity to penetrate the wall. In the plasma frame of reference, the wall appears to be ideal and is stabilising. Hence, in Figure 2.5, the crucial destabilising factor is the loss of plasma rotation.

A typical, reproducible RWM discharge in DIII-D is shown in Figure 2.5 [31].

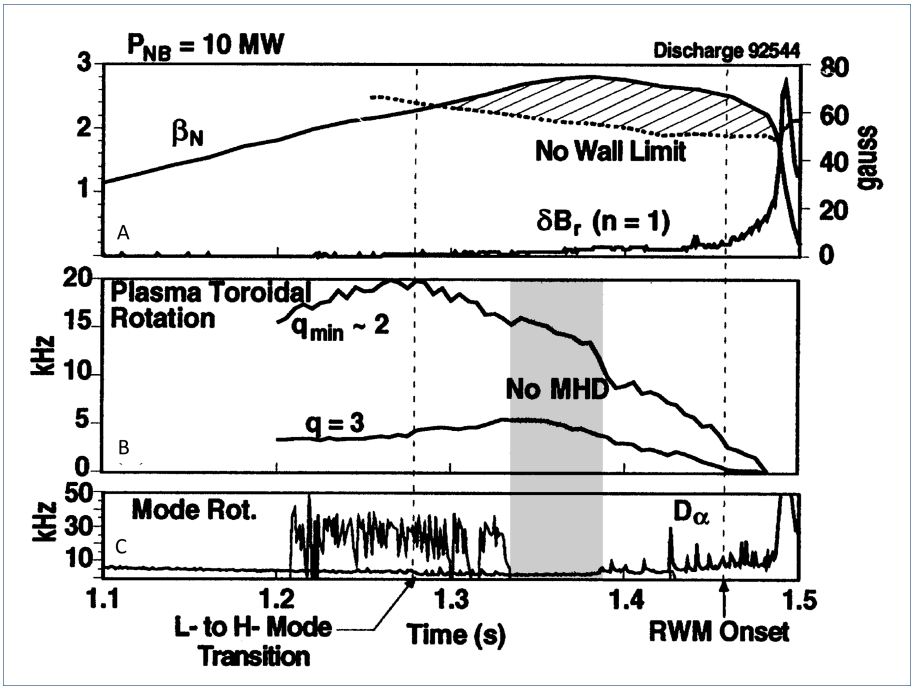

FIGURE 2.5: RWM discharge in DIII-D showing A:β_N relative to computed $\beta_N^{no-wall}$ and saddle loop δB_r amplitude of the RWM; B: plasma rotation at $q = q_{min}$ and $q = 3$; and C: MHD activity measured in Mirnov coils and photodiodes [31]

The plasma is stable until the plasma rotation at the $q = 3$ flux surface location falls beneath 1-2kHz, whereupon the RWM is unstable. The n=1 saddle loop amplitude is a direct measurement of the n=1 flux through the vessel. The growth time of the mode is 8ms and the mode rotates at 60Hz. The discharge ends in a disruption.

Analytical models often predict that a modest amount of plasma rotation is sufficient to stabilise the RWM [29, 31–33]. If there is a relative rotation frequency between the

mode and the wall, then in the frame of reference of the mode the wall appears as an ideal wall. Thus the magnetic flux perturbations do not penetrate the wall. Conversely, both experiment and theory show that drag associated with the RWM will damp plasma rotation [31, 34]. This is due to the eddy currents induced in the resistive wall by the magnetic perturbations.

2.4 Resistive Wall Modes And Nonlinear Effects

Although the RWM can be analysed linearly, as will be described in Chapter 5, it is the non-linear contributions to RWM stability that are found to be extremely important. The non-linear interaction with the toroidal plasma rotation is an important stabilisation mechanism. Non-linear-coupling to other MHD modes is also a factor in RWM stability.

2.4.1 Plasma Rotation

In Resistive Wall Mode theory, RWM stabilisation by plasma rotation Ω relative to the resistive wall is characterised in three ways by Gimblett and Hastie [35]

1. A stability window in plasma rotation, $\exists\, \Omega_1, \Omega_2$ such that the RWM is stable for $\Omega_1 < \Omega < \Omega_2$
2. A critical rotation Ω_{crit} such that the RWM is stable for $\Omega > \Omega_{crit}$
3. The RWM is never stabilised, only mitigated

Theoretical models which seek to calculate the stabilisation of the external kink provided by resistive walls require a source of dissipation in the plasma.

2.4.2 Theoretical RWM Stabilisation Models

Numerical Study Of Bondeson And Ward

The first study of rotational stabilisation was Bondeson and Ward [36].

The numerical study proposed that low n, pressure driven external kink modes could be fully stabilised when the plasma rotates at some fraction of the sound speed. The mechanism for transferring momentum from the plasma to the mode is toroidal coupling to sound waves, via ion Landau damping. Two modes were found, the plasma mode

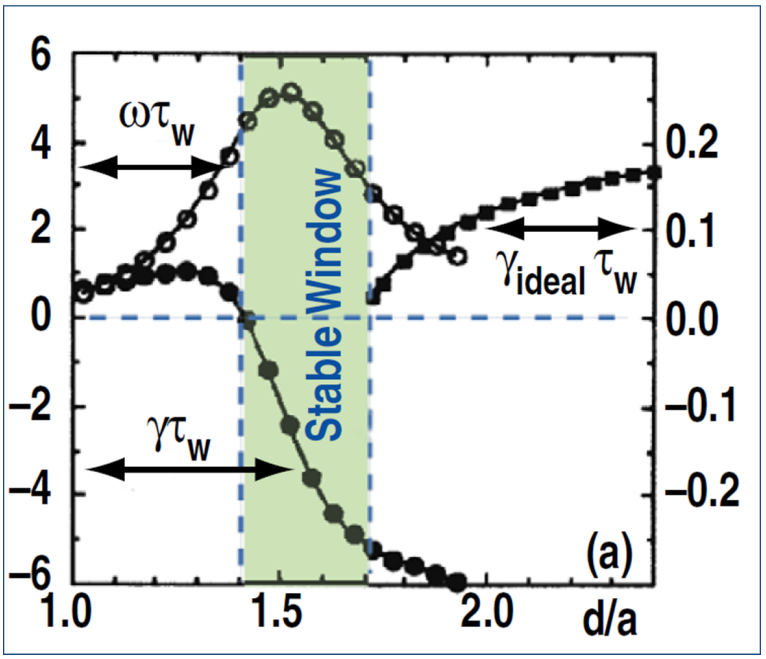

FIGURE 2.6: A stability window for a rotating plasma appears such that both the ideal plasma mode and the resistive mode are stable [29, 36].

rotating with the plasma, and the resistive mode penetrating the wall and nearly locked to it. A window of stability for both modes appears. The resistive mode is more stable as the resistive shell moves further from the plasma boundary, whereas the plasma mode is more stable if the shell approaches the plasma. The stability of the modes can be seen in Figure 2.6 for a plasma pressure 30% above the no-wall limit, rotating at $\Omega/\omega_A = 0.06$, where Ω is the plasma rotation frequency, and ω_A is the Alfvèn frequency. When the frequency of the RWM with respect to the wall is large, the RWM is stabilised. For the minor radius a, and wall radius d, the stability window for a resistive wall is $1.4 < d/a < 1.7$.

[36] gives the following explanation for RWM stabilisation. If the plasma is rotating, then the energy flux [37]

$$\partial W_p = \frac{1}{2}\int_{S_p} \xi \frac{\partial \xi}{\partial x} dS \tag{2.2}$$

is complex. This means that the perturbed radial and poloidal magnetic field components have a relative phase shift. The perturbed flux is proportional to the displacement, so the idea of energy flux can be expressed in terms of the perturbed flux ψ. The magnetic flux function ψ is defined by $\mathbf{B}_r = -\frac{1}{R}\frac{\partial \psi}{\partial Z}$ and $\mathbf{B}_Z = \frac{1}{R}\frac{\partial \psi}{\partial R}$. In linear stability analyses, the necessary quantity is the logarithmic derivative of ψ. At the plasma boundary $r = a$, [36] requires

$$\left.\frac{\psi'}{\psi}\right|_a = -\frac{m}{a}(1 + x + iy) \tag{2.3}$$

where m is the poloidal mode number. The real part, $\sim (1+x)$ means that the perturbed magnetic field transfers energy through the plasma boundary, where 1 signifies marginal stability, and x signifies an excess or a deficit of energy. The imaginary component represents the angular momentum carried by the perturbed field through the boundary. If the plasma is stationary, then $\psi^{'}/\psi \rightarrow \infty$ at the ideal wall stability boundary. If the plasma is rotating, then $\psi^{'}/\psi$ must remain finite and complex at any wall distance. The rotation of the plasma separates the plasma and the resistive modes from each other. In a rotating plasma, the perturbed plasma current I_p would force the perturbed induced wall currents I_w to rotate with respect to the wall. Hence I_p and I_w cannot grow in phase with each other, leading to stabilisation.

One limitation of this model is that the numerical code used to calculate the results modelled a stationary plasma with a rotating resistive shell, so the effect of flow shear could not be explored.

Analytical Studies For Cylindrical Plasmas

Analytical models for the stabilisation of RWMs were also proposed as a reaction to [36]. Betti and Freidberg [38] utilised a cylindrical model where mode resonance with the sound wave continuum opens up a stability window for the RWM, with a cubic dispersion relation. Adding toroidal effects increases the dissipation in the model. These results are able to explain the numerical work in [36].

[39] uses a simple cylindrical model with dissipation provided by edge plasma viscosity. In both [38] and [39], the critical rotation was found to be of the order $k_{||}av_A$, where $k_{||}$ is the parallel wave number of the RWM at the edge of the plasma, and v_A the Alfvèn speed. The external kink is unstable for $k_{||}a << 1$ for low n kink modes, so the critical rotation velocity is only a few percent of the Alfvèn speed - velocities regularly reached by neutral beam injection in tokamaks.

The results in [39] agree well with those in [36, 38] despite the difference in dissipation mechanism. Indeed, once the stability window in β_T, where β_T is the plasma parameter β measured using only the toroidal magnetic field instead of the full magnetic field, is sufficiently large, the dissipation mechanism is unimportant. As long as both plasma rotation and a dissipation mechanism are both present, a stability window exists.

Finn also studied this problem [40], but with a different stabilisation mechanism. In contrast to the previously discussed models, this study includes a resistive plasma. For a cylindrical plasma with infinite aspect ratio, with resistive wall and rigid plasma rotation, an external resonant ideal MHD mode with a rational surface in the plasma is considered.

This ideal mode, unstable with a wall at infinity but stabilised by a conducting wall, can be stabilised by becoming resistive modes, which allow a change in the magnetic topology. The resistive modes can then be stabilised by the resistive wall and bulk plasma rotation. Resistive modes imply the possible development of magnetic islands at the rational surface, which can transfer momentum to the RWM. The critical rotation frequency for stabilisation is lower than the previous models, at $<<$ 1% of the Alfvèn frequency. The use of a resistive plasma was also examined in [41] for a circular plasma.

Confirming the results in [40], [42] looked at a single mode rational surface in the plasma with the resistive kink dispersion relation [43]. The ideal mode can be stabilised by a close wall and plasma rotation on similar time scales to those found in [40], in a small parameter range.

2.4.3 Torque Balance In A Tokamak

The rotation profile in the tokamak plasma is determined by three factors

1. The natural rotation tendency of the plasma [44, 45]
2. External torque input (Neutral Beam Injection or EM interaction with external wall and error fields)
3. Inter-flux surface viscosity

The torque induced by a resistive instability and an external resistive wall is examined in [46]. The importance of the rotation of MHD modes and torque balance between the plasma and the resistive wall in the stability of the plasma was pointed out by Hender et al. [47]. Further studies [48–50] confirmed the importance of torque balance as bifurcated states for the plasma equilibrium were discovered.

2.4.4 Rotation Threshold Experiments

The importance of the inclusion of torque balance in consideration of the rotation threshold for RWM stabilisation can be seen in a series of experiments.

Initially, experiments on DIII-D and JT-60U [31, 51, 52] found relatively high values of plasma rotation were needed to stabilise the resistive wall mode. The experiments are carried out by using Neutral Beam Injection (NBI) to impart torque into the plasma, and magnetic braking (applying an external resonant non-axisymmetric field) to decelerate

the plasma. When the plasma rotation crosses the RWM stabilisation threshold, the RWM begins to grow.

However, other experiments [53, 54] found a much lower rotation threshold. These experiments used a different method to ascertain the rotation threshold, using much less NBI. An example is shown in Figure 2.7. Controlling the NBI torque with a system of co- and counter-rotation beams, non-axisymmetric magnetic braking fields are not needed to brake the plasma. Non-axisymmetric fields are minimised while the initial NBI torque is reduced until the q=2 rotation is at the level of $\Omega\tau_A \sim 0.3\%$. This is a much lower threshold than found in previous experiments with braking fields and fixed NBI injection. Varying the NBI also has a significant effect on the rotation profiles in Figure 2.7d), such that rotation at just one rational surface may not be sufficient information to analyse the stabilisation of the RWM.

The reconciliation of these different rotation thresholds lies in the torque balance of the plasma. At the mode rational surface (q=2) in external braking experiments, it has been noticed that firstly there was a slow deceleration in rotation with an increase in the external field. After this initial slow phase, a rapid drop in rotation where the magnetic perturbation transitions to a higher growth phase is noticed: the transition from slow to fast RWM growth is illustrated in Figure 2.8.

The transition between slow and fast RWM growth was thought to be the RWM rotation stabilisation threshold. In fact, it is due to a bifurcation in the torque balance equilibrium where the rotation jumps from a high to a low value. The actual RWM threshold may be in the intervening band of rotation values. The bifurcation phenomenon is explained in [50]. The rotational drag caused by the applied field has a non-monotonic dependence on the plasma rotation, due to electromagnetic shielding of the error field at the rational surface as the rotation increases. This results in greater RWM stabilisation and a smaller response from the applied field. If the plasma is subjected to high NBI torque, then there is a high unperturbed plasma rotation value, and hence a higher value of rotation at the upper entrance to the forbidden rotation band. At the bifurcation point, the eddy currents on the rational surface no longer shield the plasma from the static applied field, and there is a transition from the shielded to the fully penetrated braking field. The rotation collapses to near locking values.

In plasma shots where there is a large initial plasma rotation, the plasma rotation will undergo the bifurcation when the magnetic braking is applied. In DIII-D, the strong NBI torque and the large unperturbed plasma rotation combined with the strong magnetic braking causes the bifurcation in the torque balance. This leads to sudden decreases in rotation and increases in RWM amplitude. With initially small NBI torque and no magnetic braking, the plasma should be able to reach the true MHD stability boundary.

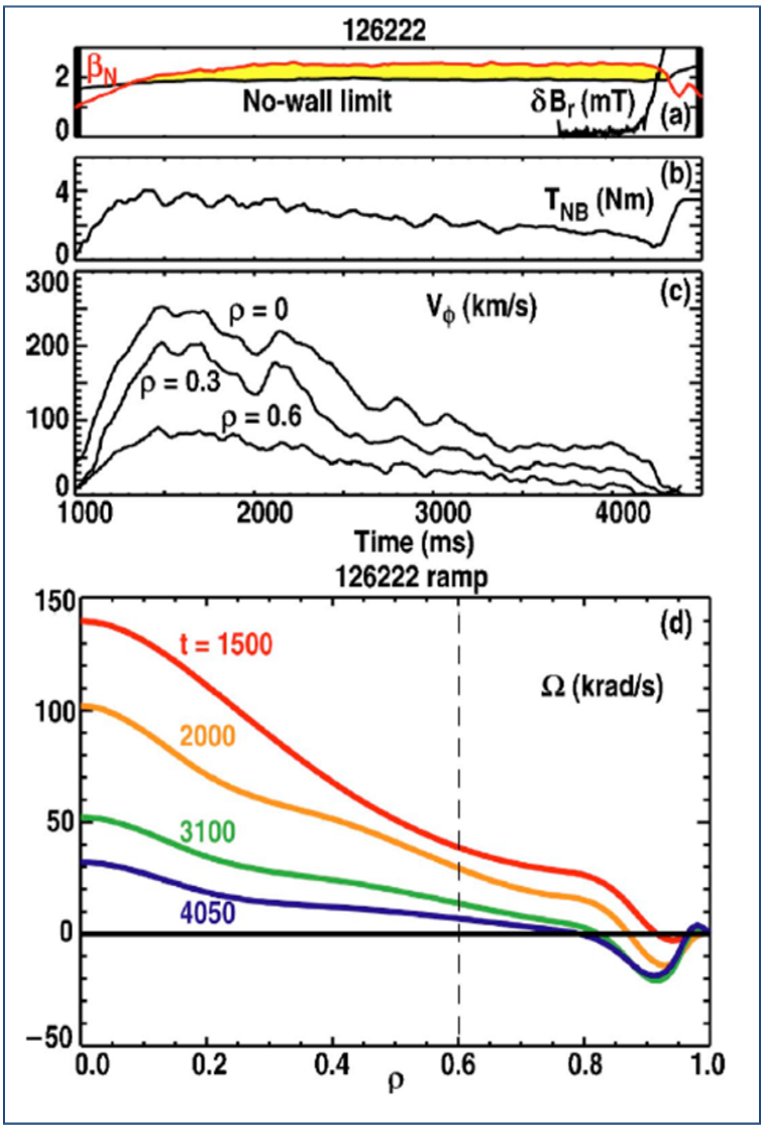

FIGURE 2.7: [53]a) shows β_N and ∂B_r amplitude of the non-rotating n=1 RWM, b) NBI torque, c) toroidal velocity at several $\rho = r/a$ locations and d) rotation profiles at various discharge times.

Hence, there is a certain level of uncertainty in the exact value of the rotation threshold for RWM growth, both experimentally and theoretically. Different models predict different thresholds, and even different approaches to braking and reduction of plasma torque in experiments yields different results. The threshold for rotational RWM stabilisation is thus also very machine dependant, which makes predictions of performance in future machines, such as ITER, challenging.

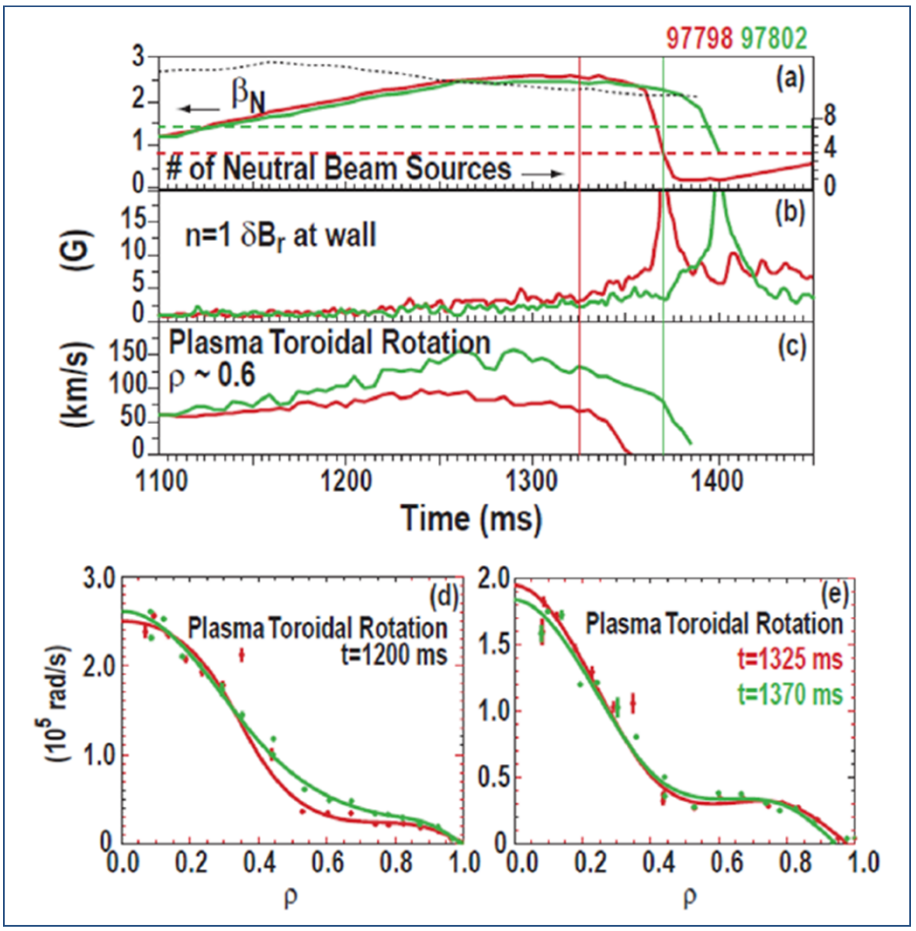

FIGURE 2.8: [34] Two experimental discharges in DIII-D with differing initial NBI torque. The figure shows a)β_N (solid curve), the no-wall limit approximation and the number of NBI sources, b) n=1 ∂B_r amplitude at the sensor loops, c) plasma toroidal rotation at $r/a \approx 0.6$ and d) rotation profiles at t=1.2s shows faster initial rotation for the discharge with greater torque input, while in e) at the transition to fast RWM growth and slow plasma rotation (vertical lines in a,b,c) the profiles are identical in both discharges. The discharge with greater initial torque survives longer before the transition from slow to fast RWM growth.

2.4.5 Torque Balance Models For The RWM

It was noticed experimentally that reducing error fields could lengthen discharges, as the drag on the plasma was reduced and rotation increased [31]. This (non-linear) effect on the plasma can be captured analytically by including the torque balance of the plasma. However, in the previous studies mentioned, the plasma rotation was not included self-consistently in the models.

In [55], Gimblett and Hastie used the Finn model [40] to show the magnetic island transferring momentum between the wall and the plasma: this provides a means to self consistently include, in a non-linear way, the plasma rotation in the model. In terms of RWM stability, the necessity of allowing the growth of the magnetic island is mitigated

by a larger region in parameter space where the RWM is stable. Self-consistent torque balance for external error fields was also studied by Fitzpatrick in [56].

In [35], torque balance was used to analyse a plasma affected by error fields (fields caused by misaligned coils). A braking effect on the plasma rotation caused by the error field is shown, and that reducing the error field amplitude will lengthen plasma discharges, which agrees with the experimental work on DIII-D [31]. Variants of this model also help understand the forbidden bands of rotation seen in [57].

The work described in [35, 55] is notable here because the structural mathematical framework which is used is similar that used in 3. A short summary of the model is included in Appendix B.

2.4.6 Other Effects On Resistive Wall Modes

External Fields

If the RWM is destabilised, it is possible to stabilise the plasma by implementing a feedback system. This was initially suggested in [58]. The principle is to replenish the magnetic flux lost through the wall using external coils. The feedback system tries to mimic an ideal wall [58], or simulate a rotating wall [59, 60].

Codes which are suitable for studying the magnetic feedback problem include STARWALL [61], which will be discussed in Chapter 5.

Kinetic Effects On The RWM

Although the Resistive Wall Mode is an MHD instability, kinetic effects can also alter the dispersion relation. A numerical study [62] analysed the potential energy δW_k associated with the MHD displacements of particles in a high temperature plasma [29]. In comparison to the purely MHD dispersion relation in 2.4, an extended dispersion relation including these effects can be written as:

$$\gamma\tau_w = -\frac{\partial W_\infty + \partial W_k}{\partial W_b + \partial W_k} \tag{2.4}$$

Effects considered included the bounce and transit resonances, and diamagnetic and magnetic drift resonances of the particles. The diamagnetic and magnetic drift resonances provide additional stabilisation for the mode, and trapped particle compressibility and resonance between the mode and precession drift frequency improves β stability limits. Slow plasma rotation is predicted to stabilise the RWM up to the ideal β limit in this model. These kinetic effects will not be considered in this thesis.

Nonlinear Coupling To Other Modes

In a low rotation regime, such as in ITER, resistive wall modes can be an issue. Even if the rotation threshold is low for RWM stabilisation [53, 54, 63, 64], other high-β MHD events can trigger RWM instability. Resistive wall modes have been observed which have been triggered by ELMs [65] and fishbones [66]. Near the no wall stability limit, the MHD modes and the RWM can couple together. The RWM driven by MHD events can remain marginally stable yet have large amplitude. However its decay can last tens of milliseconds, which is sufficiently long to cause β_N to collapse.

The MHD-driven RWM has been studied in several tokamaks, such as JT-60U [66, 67], DIII-D [68], and NSTX [69–71]. An example is shown in Figure 2.9. In this case, the plasma rotation is kept large to avoid the RWM. Since β_N is also large, additional MHD instabilities are destabilised. These are identified as an n=1 bursting mode and another slowly growing mode. The subsequent reduction of the rotation shear at $q = 2$ destabilises the RWM - the rotational shear at the rational surface is clearly also important in RWM stability.

Linear MHD can only examine the location of stability boundaries: non-linear MHD is needed to analyse mode amplitudes, saturation and mode coupling, as illustrated in Figures 2.10. The added difficulty inherent in non-linear MHD is suited for large, complex codes such as JOREK. JOREK is discussed in Chapter 5.

2.5 RWM Control In ITER

Since the baseline scenario for ITER is not an advanced tokamak scenario, avoidance and control of the RWM was not a priority in the design of ITER. Control of Edge Localised Modes is of higher importance, but it has been proposed that the ELM control coils could be used as RWM (and error field) control coils [73].

Figure 2.11a) shows the preliminary ITER resistive wall design, and b) shows the pattern of the eddy current caused by the RWM on the 3D resistive vessel [74].

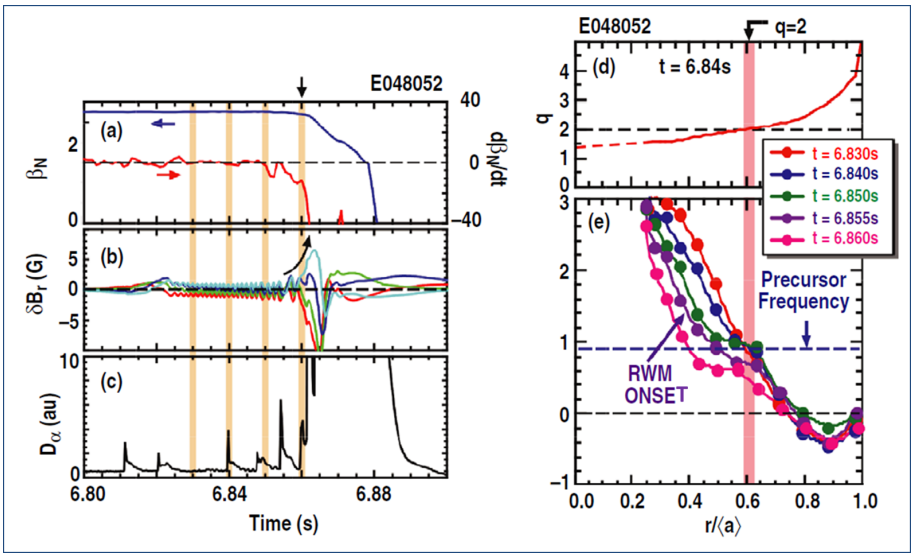

FIGURE 2.9: Details of an MHD driven RWM in JT-60U [66]. a) shows β_N and $d\beta_N/dt$ b) shows the n=1 magnetic perturbation and c) shows the D_α emission. As a function of minor radius, d) shows the safety factor profile and e) the toroidal rotation profile at different times. The RWM drags the plasma rotation inside the $q = 2$ surface.

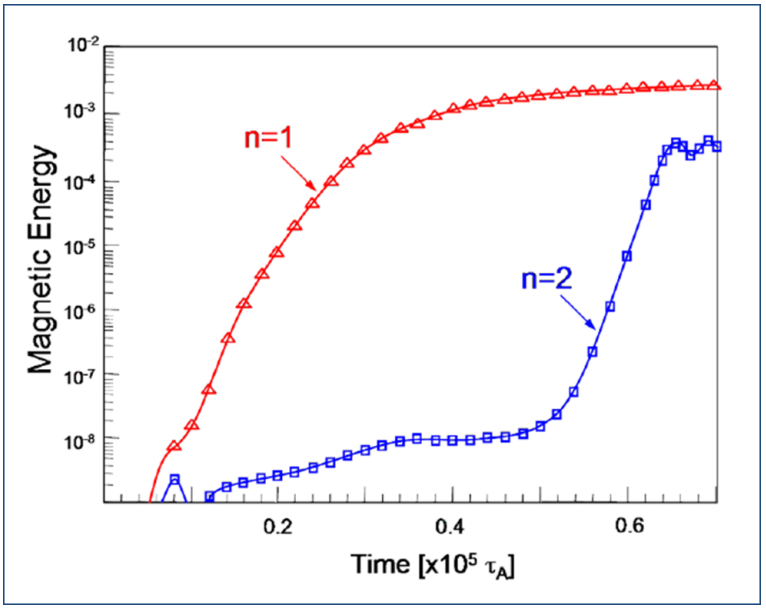

FIGURE 2.10: Nonlinear MHD is needed to examine interactions between different MHD modes. In this figure [72], changes in the current profile at the $q = 3/2$ rational surface due to the 2/1 RWM drive the 3/2 internal mode.

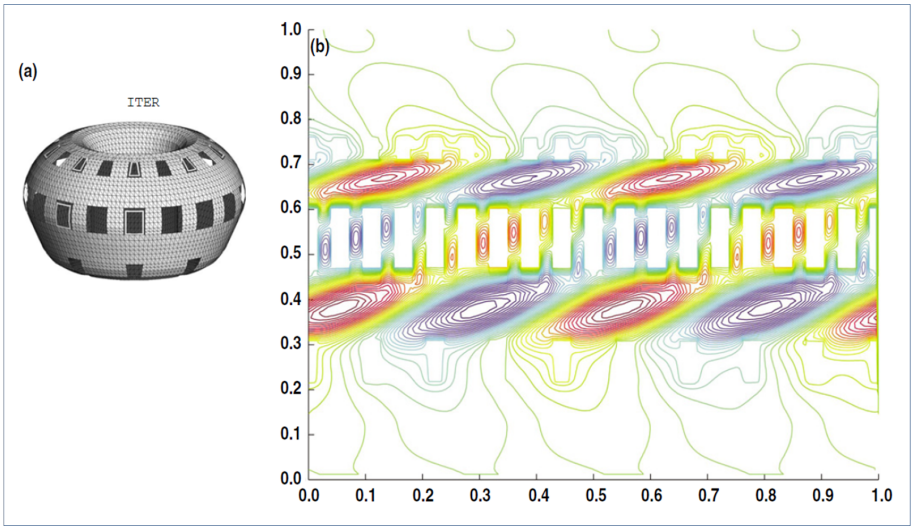

FIGURE 2.11: a) shows the ITER wall design, and b) shows the eddy current pattern generated by the RWM on the resistive wall [74].

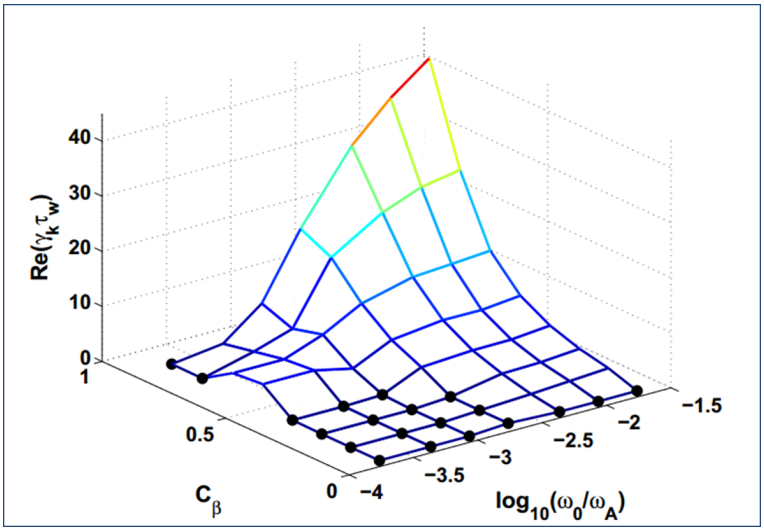

FIGURE 2.12: RWM growth rates in ITER as a function of plasma rotation frequency ω_0 and C_β. Stable RWMs are shown by black dots [75].

The rotational stabilisation of the RWM in ITER has been analysed, and is shown in Figure 2.12 [75]. The figure shows the real part of the RWM eigenvalue calculated by self-consistent kinetic calculations. The growth rate is a function of plasma rotation frequency ω_0 and $C_\beta = (\beta_N - \beta_N^{no-wall})(\beta_N^{ideal-wall} - \beta_N^{no-wall})$. Stabilisation of the mode is predicted for slow plasma rotation and low pressure. For a plasma with ITER-like parameters, only partial stabilisation is achieved. The level of rotation in ITER is not expected to be large. This is due partly to the use of negative ion-based neutral beam injection systems, which will impart less momentum to the plasma than systems using positive ions: for a given power, higher energy beams will have less momentum than low

energy beams.

Chapter 3

Neoclassical Tearing Modes and Coupling to Resistive Wall Modes in Rotating Plasmas

The Resistive Wall Mode is an ideal plasma instability, influenced by the external resistive wall. However, other MHD instabilities are predicated upon resistive plasma. In ideal MHD, the magnetic geometry is frozen into the plasma, whereas the presence of the resistivity in the plasma allows magnetic reconnection, and thus the alteration of the magnetic geometry. In terms of a tokamak plasma, the magnetic reconnection that can occur alters the nested toroidal flux surfaces required for optimal confinement.

The tearing mode instability results in a chain of magnetic islands which break the axisymmetric magnetic configuration, as seen in Figure 3.1. The increase in radial particle and energy flux across the islands due to the large distance around the island travelled by a magnetic field line degrades the overall confinement of the plasma. These magnetic islands form at rational surfaces, where the plasma resistivity becomes important. The first observations of Neoclassical Tearing Modes (described in Section 3.1.2) were made [76] after their analytic prediction.

3.1 Theory Of Neoclassical Tearing Modes

Since the tearing mode is localised to the rational surface, the analytical treatment can be simplified by two assumptions. Firstly, that the linear MHD equations are valid in the plasma away from the rational surface where the magnetic island is located; and

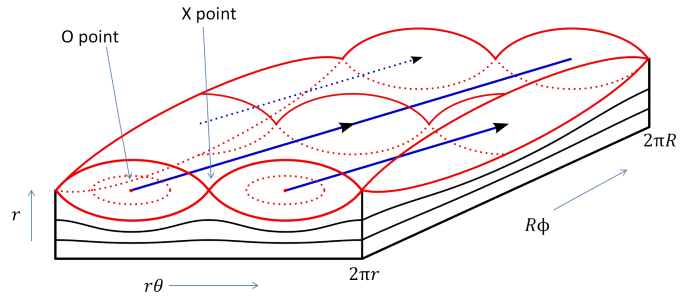

FIGURE 3.1: Magnetic islands form on a rational flux surface. The O- and X-points of the island are labelled.

secondly, that the plasma resistivity is only important at the rational surface, such that ideal MHD can be used in the bulk of the plasma.

Solving the linear ideal MHD equations for the magnetic flux function $\psi(r)$, integrated from the centre of the plasma to the rational surface, and from the edge to the rational surface, assuming continuity of the magnetic flux at the rational surface, results in a discontinuity in the radial derivative of the magnetic flux across the rational surface. This discontinuity is caused by the current sheet formed at the rational surface.

$\Delta^{'}$ [77] is defined by

$$\Delta^{'} = \frac{1}{\psi}\left[\left.\frac{d\psi}{dr}\right|_{r_s^+} - \left.\frac{d\psi}{dr}\right|_{r_s^-}\right] \tag{3.1}$$

where ψ is the magnetic flux function, and $\Delta^{'}$ parameterises this radial discontinuity. In order to analytically explore the island evolution, the resistive MHD equations can then be solved in a narrow region around the rational surface, and the layer solution matched to the outer, ideal MHD solution at the edge of the layer domain. $\Delta^{'}$ is a property of the global plasma equilibrium, and represents the free energy available in the current density profile to drive island growth.

3.1.1 Classical Tearing Modes

The classical tearing mode [78] is driven by the free energy in the plasma current distribution, which is a property of the global plasma equilibrium. This free energy is represented by the parameter $\Delta^{'}$, defined in Equation 3.5.

In the rational layer, Ampère's Law describes the relation between the magnetic flux function ψ and the current parallel to the magnetic field

$$\frac{1}{R}\frac{d^2\psi}{dr^2} = \mu_0 J_{||} \tag{3.2}$$

The simplest model for the current is that of an induced current only [78], such that the current has a dependence on $\frac{d\psi}{dt}$.

Integrating Equation 3.2 across the rational layer, we obtain the classical Rutherford tearing mode equation [78]

$$a_1 \tau_r \frac{dw}{dt} = r_s^2 \Delta^{'} \tag{3.3}$$

where $a_1 = 0.82$ is derived from the island geometry and $\tau_r = \mu_0 r_s^2/\eta$, where η is the plasma resistivity and w is the half width of the magnetic island. The magnetic island half width w is proportional to $\psi^{1/2}$, which means that $w \propto B_R^{\frac{1}{2}}$ - $B_R^{\frac{1}{2}}$ is the perturbed radial magnetic field. There is no contribution from $\nabla\phi$, where ϕ is the electrostatic potential, to the parallel electric field- the term will average to zero over a flux surface in the absence of perpendicular drifts due to the requirement that $\nabla \cdot \mathbf{J} = 0$.

Equation 3.3 shows that the island is expected to grow linearly with time if $\Delta^{'} > 0$. However, additional effects which stem from the island region itself can also have an effect on the island growth (recall that $\Delta^{'}$ is a property of the global equilibrium).

3.1.2 Neoclassical Effects On Tearing Mode Theory

The inclusion of only the induced current in the analysis of $J_{||}$ is not sufficient to model all the characteristics of tearing modes observed in tokamaks. Additional contributions to $J_{||}$ include threshold physics that describes more accurately the time evolution of the magnetic islands.

The perturbation to the neoclassical bootstrap current, previously mentioned in the Introduction chapter, is a key part of the neoclassical tearing mode physics. As discussed previously, the bootstrap current is proportional to the pressure gradient, and flows along magnetic field lines. The structure of the magnetic island, which increases the radial energy flux, flattens the pressure profile at the island location, as in Figure 3.2. The removal of the pressure gradient in the vicinity of the island further perturbs the bootstrap current, which enhances the perturbation of the current density. This provides a feedback mechanism for continued island growth.

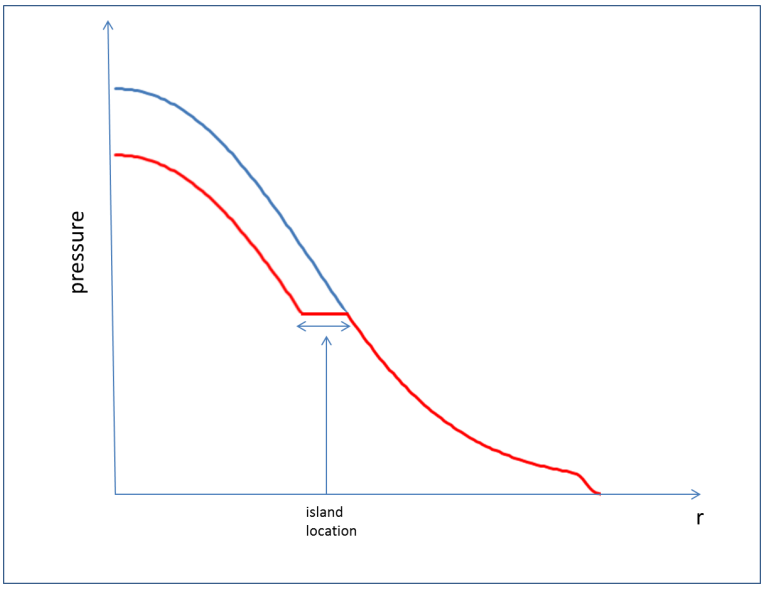

FIGURE 3.2: At the vicinity of a magnetic island, the pressure is flattened as the change in magnetic topology allows for increased radial fluxes. This results in a loss of pressure in the core of the plasma.

In fact, the bootstrap drive is often larger than the classical Δ' drive, such that even if the tearing mode is classically stable, the bootstrap current drive can drive a tearing mode- this is the *neoclassical tearing mode*.

The addition of the bootstrap drive to the neoclassical tearing mode theory leads to a conclusion that islands will grow until they saturate at a large island width. This saturated width can be comparable to the minor radius of the tokamak, and would thus cause the plasma to terminate in a disruption. As discussed in Section 1.4.2, MHD instabilities localise at rational surfaces. Rational surfaces are the flux surfaces in the plasma where the safety factor is a rational number: that is, the safety factor as expressed as the ratio of the number of toroidal turns to the number of poloidal turns necessary for a particle following the magnetic field line to return to the same location in the plasma. A neoclassical tearing mode will form a magnetic island on a rational surface. This theory predicts that all NTMs with rational surfaces in the plasma are unstable, and so the tokamak as a confinement device would be useless. However, since the tokamak is indeed feasible, there must be further effects which need to be considered. These are effects which are important at very small island widths.

Two effects which significantly alter NTM behaviour at small island widths are radial diffusion [79, 80] and finite orbit width effects.

Since the presence of the magnetic island causes pressure flattening, this implies that transport parallel to the magnetic field lines dominates. However, for small islands,

perpendicular transport cannot be neglected, and the pressure gradient is not fully removed from within the island. Thus the bootstrap current is only partially removed, and the neoclassical drive is ineffective. Thus an expression for a critical island width, below which the perpendicular transport is not negligible, can be derived.

Finite orbit width effects [81–86] lead to a different contribution to the current perturbation. An electrostatic potential is associated with each small magnetic island (comparable to the ion banana width), caused by the differing behaviour of ions and electrons at the perturbed magnetic surfaces. This potential leads to a current flowing perpendicular to the magnetic field lines: this is the neoclassical polarisation current. The divergence of this current is not zero, so a parallel current must also flow [87].

The addition of radial diffusion and the parallel current existing due to the polarisation current - which is generally supposed to be stabilising- leads to the introduction of an additional equilibrium point in the NTM island evolution. A sketch of the characteristic neoclassical island evolution is shown in Figure 3.3.

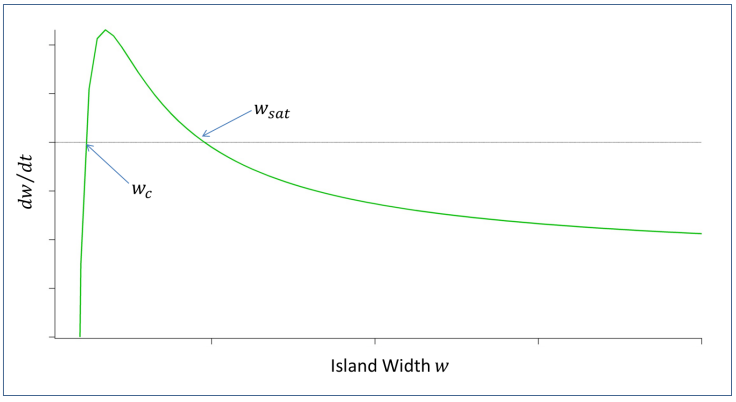

FIGURE 3.3: This sketch shows the NTM growth rate for varying island widths. The growth rate is positive for island sizes $w_c < w < w_{sat}$.

As discussed above, as the island grows, it will saturate at a large island width, w_{sat}. Furthermore, only islands above a certain critical island width w_c will have $dw/dt > 0$ and be able to grow [76, 79, 83]. Islands smaller than w_c will shrink as $dw/dt < 0$. This resolves the previous problem where all NTMs are found to be unstable, since only sufficiently large islands are in fact able to grow. In addition, the plasma must have sufficiently high poloidal beta β_θ (which is the ratio of plasma pressure to poloidal magnetic field pressure) in order to grow, otherwise $dw/dt < 0$ for all island widths.

If only sufficiently large islands are able to grow, the initial 'seed' island for an NTM must be created by other magnetic activity [88, 89]. This can include Edge Localised Modes [90], fishbones [91], and sawteeth [91–94].

3.2 Triggerless NTMs

Although NTM theory tells us that an initial 'seed' island, of sufficient size, must be created for the NTM to grow and saturate, experimental observations of NTMs which do not seem to have been seeded in the manner described above, have been made [31, 91, 95, 96]. These are known as *triggerless* or *spontaneous* NTMs.

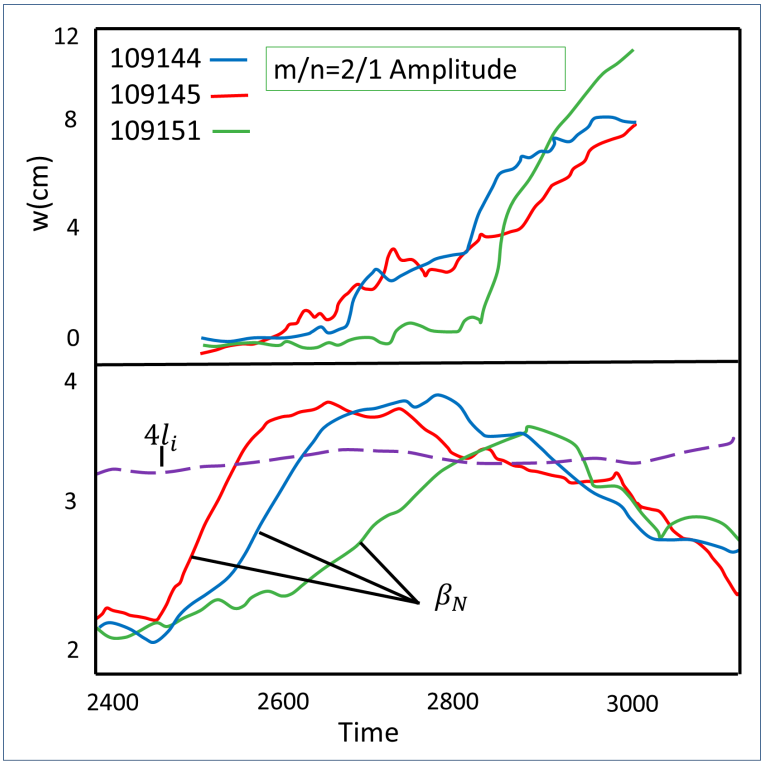

FIGURE 3.4: Triggerless NTM experiments in DIII-D [96] show magnetic islands growing from extremely small magnetic islands.

Data from three experiments on DIII-D, designed to investigate triggerless NTMs, is shown in Figure 3.4. Approaching the no-wall limit, which is approximated experimentally by $4l_i$ (the plasma inductance), the amplitude of the islands increases. The island width is interpolated from magnetic probe signals received from toroidally separated probes. However, in these plasma discharges, there is no discernable seeding process. Ordinarily, the seed island width would be expected to be around a centimetre [96] but in this figure it can be clearly seen that the magnetic islands are found to grow from a smaller size than the seed island width. For comparison, [96] also describes experiments where an NTM is destabilised by MHD instabilties.

Understanding the processes which lead to the growth of these *triggerless* NTMs is the motivation for both Chapter 3 and Chapter 4 of this thesis.

Triggerless NTMs are often seen near the no wall limit [97], which is where the Resistive Wall Mode is destabilised. Coupling the NTM to the RWM allows us to explore the interaction between the two instabilities, and analyse whether their coupling can provide a model to investigate the triggerless NTM phenomenon.

3.3 Analytic Coupling Of Resistive Wall Mode To Neoclassical Tearing Mode

Suppose an ideal, toroidally rotating plasma is surrounded by a thin wall at $r = r_w$ with finite conductivity σ_w, and contains a resistive layer in the vicinity of an internal rational surface at $r = r_s$ where a magnetic island can form. The regions outside the resistive layer are assumed to be described by linear ideal MHD. Within the layer, resistivity and non-linear effects associated with magnetic islands are retained. The plasma geometry is shown in Figure 3.5. In the following analysis, geometrical factors are neglected to obtain a simpler model which nevertheless retains the essential physics. In addition, more subtle effects such as the physics of rotation on the matching of the layer solution to the external ideal MHD solution are neglected [98].

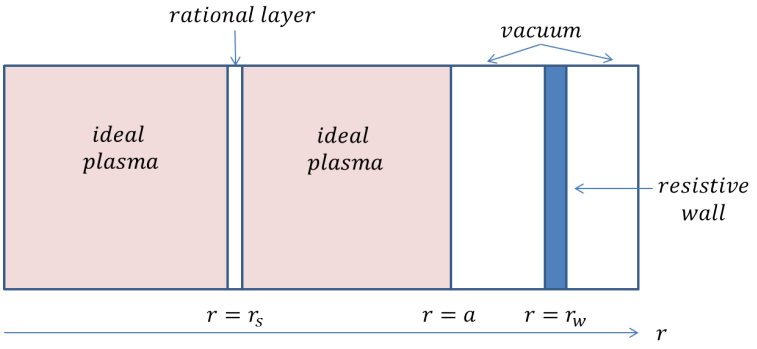

FIGURE 3.5: The plasma is assumed to be ideal apart from the narrow layer near a rational surface (the 'rational layer') where non-linear effects and resistivity are important. The plasma is surrounded by a resistive wall and vacuum.

3.3.1 Evaluating Discontinuities Across Wall And Layer

Due to skin currents in the resistive wall and at the rational surface, the component of the vector potential parallel to the equilibrium magnetic field has a discontinuous radial derivative at these locations. These discontinuities are parameterised by Δ_W and Δ_L respectively.

In a linear, ideal MHD cylindrical model using a complex representation of the perturbed fields, Δ_W and Δ_L can be related in a simple way[35, 99]. This is because the MHD eigenfunction in this situation is a second order differential equation [55].

$$\Delta_L = \frac{1 - \delta\Delta_W}{-\epsilon + \Delta_W} \tag{3.4}$$

ϵ and δ depend on the equilibrium, and are related to the stability properties of the plasma in the limit of no wall and a superconducting wall respectively. They can be derived for a given equilibrium by solving ideal MHD equations outside the wall and rational layer with appropriate boundary conditions at $r = 0$ and $r = \infty$, with the (dimensionless) definition

$$\Delta_{L,W} = \frac{r_{s,w}}{\psi_c}\frac{\partial\psi_c}{\partial r}\bigg|_{r_{s,w}^-}^{r_{s,w}^+} \tag{3.5}$$

Here, ψ_c is the complex representation of the magnetic flux function derived from linear ideal MHD. When no wall is present, $\Delta_W = 0$ and for an ideally unstable plasma (where an inertial response for the layer is appropriate and $\Delta_L < 0$ corresponds to instability to ideal MHD modes), ϵ is positive and small. For an ideal superconducting wall at $r = r_w$, $\Delta_W \to \infty$ and $\delta > 0$ provides stability to the internal kink mode, i.e. $\Delta_L < 0$. Thus, equilibria with small $\epsilon, \delta > 0$ are susceptible to a RWM but avoid the internal kink mode.

Whilst linear equations are solved in the outer region of the plasma, the need to anticipate matching to the non-linear solution at the rational layer can be anticipated. Assuming that the time dependence can be separated from the spatial dependence, the outer region solution can be expressed

$$\psi_c(r,t) = \tilde{\psi}e^{i\xi}e^{\int \rho dt} \tag{3.6}$$

where $\rho(t) = \gamma(t) - i\omega(t)$, with γ the instantaneous growth rate, ω the mode frequency relative to the wall, and $\xi = m\theta - n\phi$ the helical angle defined in terms of the poloidal (θ) and toroidal (ϕ) angles. It will be assumed that the toroidal mode number $n = 1$, with m the poloidal mode number.

Resistive Wall Response

Using Ampère's law in the thin resistive wall [100], the wall response can be calculated.

For Faraday's and Ohm's Laws,

$$\frac{\partial \mathbf{B}}{\partial t} = -\nabla \times \mathbf{E} = -\nabla \times \eta_w \mathbf{J} \tag{3.7}$$

where $\eta_w = 1/\sigma_w$ is the wall resistivity (taken as a constant). Ampère's Law implies that

$$\nabla \times \nabla \times \mathbf{B} = \mu_0 \nabla \times \mathbf{J} \tag{3.8}$$

Thus

$$\frac{\partial \mathbf{B}}{\partial t} = \frac{\eta_w}{\mu_0}(\nabla(\nabla \cdot \mathbf{B}) - \nabla^2 \mathbf{B}) \tag{3.9}$$

and it follows that, since $\nabla \cdot \mathbf{B} = 0$,

$$\frac{\partial \mathbf{B}}{\partial t} = -\frac{\eta_w}{\mu_0}\nabla^2 \mathbf{B} \tag{3.10}$$

Defining the complex magnetic flux function ψ_c as $\mathbf{B}_r = -\frac{1}{R}\frac{\partial \psi_c}{\partial Z}$ and $\mathbf{B}_Z = \frac{1}{R}\frac{\partial \psi_c}{\partial R}$, and taking the radial component of Equation 3.10, we obtain

$$\frac{\eta_w}{\mu_0}\nabla^2 \psi_c = \frac{\partial \psi_c}{\partial t} \tag{3.11}$$

Since the wall is assumed to be thin, $\nabla^2 \sim \partial^2/\partial r^2$.

$$\frac{\partial^2 \psi_c}{\partial r^2} = \mu_0 \sigma_w \frac{\partial \psi_c}{\partial t} \tag{3.12}$$

Now consider the form of ψ_c, the complex magnetic flux function given in 3.6:

$$\frac{1}{\psi_c}\frac{\partial \psi_c}{\partial t} = \rho \tag{3.13}$$

Integrating across the thin wall and recalling the definition of Δ_W given in 3.5, it is possible to obtain

$$\Delta_W = \rho \tau \tag{3.14}$$

where $\tau = \frac{\tau_w}{\tau_r}$, and $\tau_w = \mu_0 d \sigma_w r_w$ is the wall diffusion time, with the wall thickness $d << r_w$, the minor radius at which the wall is located. The instantaneous complex growth rate ρ is normalised to $\tau_r = \sigma \mu_0 a r_s$, the resistive plasma diffusion time where σ is the plasma conductivity at the rational surface. Combining these results, the linear cylindrical dispersion relation [35] is obtained

$$\Delta_L = \frac{1 - \delta\rho\tau}{-\epsilon + \rho\tau} \tag{3.15}$$

3.3.2 NTM Evolution

In the linearised ideal MHD region of the plasma, a complex representation for the magnetic flux is required to ensure that 3.4 holds [55]. The physical flux is denoted $\psi_L = Re[\psi_c]$. In the rational layer where non-linear physics is retained, the complex representation cannot be used, so the physical flux ψ_L is employed.

Assume a magnetic island exists at the rational surface. Transforming into the frame of reference where the rational surface is at rest, the wall is rotating. Analogously to the wall response, Ampère's law describes the current perturbations at the rational surface

$$\frac{\partial^2 \psi_L}{\partial r^2} = -\mu_0 J_{||} \tag{3.16}$$

where $J_{||}$ is the component of current density perturbation parallel to the magnetic field. There are two contributions to $J_{||}$ considered: an inductive component proportional to $\partial\psi_L/\partial t$, and the perturbation in the bootstrap current J_{bs} caused by the pressure flattening inside the island. For the induced current contribution, $E_{||}$ can be expressed as, firstly,

$$E_{||} = -\frac{\partial \mathbf{A}_{||}}{\partial t} \tag{3.17}$$

due to the equivalences of

$$\frac{\partial \mathbf{B}}{\partial t} = \frac{\partial}{\partial t}(\nabla \times \mathbf{A}) = \nabla \times \frac{\partial \mathbf{A}}{\partial t} = -\nabla \times \mathbf{E} \tag{3.18}$$

Then we consider that $\mathbf{A}_{||}$ is equal to ψ_L. Thus, $J_{||}^{induced} = \sigma E_{||} = -\sigma \frac{\partial \psi_L}{\partial t}$.

Assuming these current perturbations are localised within the layer, and integrating across the layer, we obtain

$$\left.\frac{\partial \psi_L}{\partial r}\right|_{r_s^-}^{r_s^+} = 2\sigma\mu_0 w \frac{\partial \psi_L}{\partial t} - 2\mu_0 w J_{bs} \tag{3.19}$$

where w is the half-width of the magnetic island. The discontinuity on the left hand side of 3.19, caused by the current sheet in the layer, can now be expressed in terms of Δ_L.

ψ_L is assumed to be of the form $\psi_L = \tilde{\varphi}\cos(\hat{\alpha} + \zeta)$, where $\hat{\alpha} = \xi - \int \hat{\omega} dt$, $\zeta(r)$ is a phase factor. The mode frequency in this rotating frame is $\hat{\omega} = \omega - \Omega_L$, where Ω_L is the toroidal plasma rotation frequency at $r = r_s$ relative to the stationary wall.

Evaluating $\left.\frac{\partial \psi_L}{\partial r}\right|_{r_s^-}^{r_s^+}$

The left hand side of 3.19 is evaluated by matching to the ideal MHD solution in the outer regions of the plasma.

The complex representation of the magnetic flux function 3.6 can be decomposed into its real and imaginary parts:

$$Re[\psi_c] = e^{\int \gamma dt}(Re[\tilde{\psi}]\cos\hat{\alpha} - Im[\tilde{\psi}]\sin\hat{\alpha}) \tag{3.20}$$

$$Im[\psi_c] = e^{\int \gamma dt}(Re[\tilde{\psi}]\sin\hat{\alpha} + Im[\tilde{\psi}\cos\hat{\alpha}]) \tag{3.21}$$

recalling that $\tilde{\psi}$ is the amplitude of the magnetic flux function in 3.6.

If $\psi_L = \tilde{\varphi}\cos(\hat{\alpha} + \zeta)$, then

$$\psi_L = \tilde{\varphi}(\cos\hat{\alpha}\cos\zeta - \sin\hat{\alpha}\sin\zeta) \tag{3.22}$$

Hence, if $Re[\psi_c] = \psi_L$, the coefficients of $\cos\hat{\alpha}$ and $\sin\hat{\alpha}$ can be matched between 3.20 and 3.22

$$Re[\tilde{\psi}]e^{\int \gamma dt} = \tilde{\varphi}\cos\zeta \tag{3.23}$$

$$Im[\tilde{\psi}]e^{\int \gamma dt} = \tilde{\varphi}\sin\zeta \tag{3.24}$$

Now, since Δ_L is defined in terms of ψ_c,

$$\left.\frac{\partial \psi_L}{\partial r}\right|_{r_s^-}^{r_s^+} = \frac{1}{r_s}(Re[\Delta_L]Re[\psi_c] - Im[\Delta_L]Im[\psi_c]) \tag{3.25}$$

Substituting for $Re[\psi_c]$ and $Im[\psi_c]$ using 3.20, 3.21, and then using 3.23, 3.24

$$\left.\frac{\partial \psi_L}{\partial r}\right|_{r_s^-}^{r_s^+} = \frac{\tilde{\varphi}}{r_s}(Re[\Delta_L]\cos(\hat{\alpha}+\zeta) - Im[\Delta_L]\sin(\hat{\alpha}+\zeta)) \tag{3.26}$$

Nonlinear Island Effects

Combining 3.26 with 3.19, and taking the time derivative of ψ_L yields

$$\frac{\tilde{\varphi}}{r_s}(Re[\Delta_L]\cos(\hat{\alpha}+\zeta) - Im[\Delta_L]\sin(\hat{\alpha}+\zeta)) = 2\sigma\mu_0 w\left(\frac{\partial\tilde{\varphi}}{\partial t}\cos(\hat{\alpha}+\zeta) + \hat{\omega}\tilde{\varphi}\sin(\hat{\alpha}+\zeta)\right) - 2\mu_0 w J_{bs} \tag{3.27}$$

Multiplying by $\cos(\hat{\alpha}+\zeta)$ or $\sin(\hat{\alpha}+\zeta)$, and the integrating over $\hat{\alpha}$ yields equations for w and $\partial\tilde{\varphi}/\partial t$. The island half-width w is related to $\tilde{\varphi}$ by [3]:

$$w^2 = \frac{4 r_s L_s \tilde{\varphi}}{B_\theta q R} \tag{3.28}$$

where $L_s = Rq/s$ is the shear length scale, q is the safety factor, s is the magnetic shear, R is the major radius, and B_θ is the poloidal magnetic field. Normalising the island half-width to the minor radius a, and time t to τ_r, we obtain two equations

$$4\dot{w} = Re[\Delta_L] + \frac{\hat{\beta}}{w}\left(1 - \frac{w_c^2}{w^2}\right) \tag{3.29}$$

$$2w(\omega - \Omega_L) + Im[\Delta_L] = 0 \tag{3.30}$$

where $\dot{w}$ refers to time derivatives of w with respect to $\hat{t} = t/\tau_r$, and $J_{bs} = (\beta_\theta B_\theta \sqrt{\hat{\varepsilon}}/L_p\mu_0)\cos(\hat{\alpha}+\zeta)$, where β_θ is the poloidal beta, $\hat{\varepsilon}$ the inverse aspect ratio, $1/L_p = (1/p)(dp/dr)$ the pressure length scale and w_c the seed island threshold width. This results in a definition of $\hat{\beta} = (8\sqrt{\hat{\varepsilon}}\beta_\theta r_s/L_p s)$.

It is important to note that $\gamma = 2\dot{w}/w$, ω and Ω_L have been normalised to τ_r also.

In addition to the bootstrap current J_{bs}, a heuristic threshold term $(1 - w_c^2/w^2)$ has been added. This introduces the essential non-linear seed island physics needed for

studying the NTM. As discussed briefly above, the threshold term can be attributed to the polarisation current effects [83].

Equation 4.1 is the same relation as found in [101] if the plasma toroidal rotation is not considered. The full expression for Δ_L in terms of γ, ω and Ω_L is given by

$$\Delta_L = \frac{(1-\delta\tau\gamma)(\epsilon+\tau\gamma)-\delta\tau^2\omega^2}{(-\epsilon+\tau\gamma)^2+\tau^2\omega^2} + i\frac{\tau\omega(1-\epsilon\delta)}{(-\epsilon+\tau\gamma)^2+\tau^2\omega^2} \tag{3.31}$$

3.4 Toroidal Torque Balance

The plasma toroidal rotation at the rational surface, Ω_L, has so far not been dealt with. In order to determine Ω_L self-consistently, the torque balance in the plasma must be calculated. Ideal plasma is torque-free [102], and so the torque exerted on the plasma is a delta-function at the rational surface, $\delta(r-r_s)$.

Consider the perturbed MHD momentum balance equation in the non-ideal layer, averaged over the flux surface

$$\langle \delta\mathbf{J} \times \delta\mathbf{B} \rangle + \rho\mu\nabla^2 v = 0 \tag{3.32}$$

where the angled brackets denote the average over a flux surface. Here ρ is the plasma density and μ the plasma viscosity. It can be assumed that the processes under consideration occur over many viscous diffusion times, and pressure is constant across the thin layer. The pressure gradient is neglected as it will not contribute once 3.32 is integrated across the layer (as follows).

Assume that v is continuous across the layer, but ∇v possesses a discontinuity at $r = r_s$ due to the localised torque at that location. For a perturbation $\delta\mathbf{B}$, $\nabla\times\delta\mathbf{B} = -\nabla^2\psi_L\mathbf{b}$. Only the toroidal component is required. Integrating 3.32 over the rational layer

$$\left\langle \frac{\tilde{\varphi}}{R\mu_0}\sin(\hat{\alpha}+\zeta)\frac{\partial\psi_L}{\partial r}\bigg|_{r_s^-}^{r_s^+} \right\rangle + \rho\mu\frac{\partial v_\phi}{\partial r}\bigg|_{r_s^-}^{r_s^+} = 0 \tag{3.33}$$

The discontinuity in the radial derivative of $\psi_L = Re[\psi_c]$ is evaluated as before. Integrating over $\hat{\alpha}$, all terms containing $Re[\Delta_L]$ disappear.

If $v_\phi = \Omega R$, then using the normalisations described above,

$$\frac{\partial\Omega}{\partial r}\bigg|_{r_s^-}^{r_s^+} = \frac{A}{a}w^4 Im[\Delta_L] \tag{3.34}$$

such that $A = s^2\hat{\varepsilon}^2 a^3 \tau_v \tau_r / 512 r_s^3 q^2 \tau_A^2$, with $\tau_v = a^2/\mu$ the momentum confinement time, a the minor radius, and $\tau_A = (a\sqrt{(\mu_0\rho)}/B)$ the Alfvén time, and taking $\sigma = T_e^{3/2}/1.65 \times 10^{-9} \ln\lambda$, with T_e expressed in keV. The safety factor q at $r = r_s$ will be taken as $q = 2$.

The electromagnetic torque is finite when $Im[\Delta_L] \neq 0$, and always acts to damp the plasma rotation [56]. $Im[\Delta_L]$ is related to the discontinuity in the derivative of the phase factor ζ [35]: the torque only acts on the plasma in the rational layer when $\frac{\partial\zeta}{\partial r}|_{r_s^-}^{r_s^+} \neq 0$.

In the outer ideal plasma, the momentum equation is simply

$$\frac{d^2\Omega}{dr^2} = 0 \tag{3.35}$$

The linear rotation profile in the ideal plasma regions $r < r_s$ and $r_s < r < a$ is continuous at $r = r_s$, but has a discontinuity in the first radial derivative there, caused by the torque. Imposing no-slip boundary conditions at the outer edge of the plasma $r = a$ (viscous drag effects) and a driving force at the inner edge at $r = 0$ that maintains $\frac{d\Omega}{dr} = -\Omega_0/a$, the toroidal rotation frequency profile can be constructed in the region of ideal plasma.

$$\Omega(r) = \begin{cases} \lambda(a - r_s) + \frac{\Omega_0}{a}(r_s - r) & 0 < r < r_s \\ \lambda(a - r) & r_s < r < a \end{cases}$$

for constant $\lambda > 0$. The discontinuity in the radial derivative is calculated to be $-\lambda + \Omega_0/a$. Hence, at $r = r_s$, using 3.34, the damping of the toroidal plasma rotation frequency is found to be given by

$$(\Omega_0 - f\Omega_L) = Aw^4 Im[\Delta_L] \tag{3.36}$$

where $f = a/(a - r_s)$.

Appendix B describes the similar model constructed by Gimblett and Hastie in [55], and its difference from this approach.

3.5 Summary Of Results

The theory of classical and neoclassical tearing modes was discussed, with particular emphasis on the threshold properties of both the island width and the value of β_θ. In addition, the phenomenon of triggerless NTMs is introduced. A system where an NTM is coupled to a RWM is derived. By coupling together the resistive wall and the rational layer where the magnetic island is located (and the respective discontinuities in the

magnetic flux function); and including a self consistent evaluation of the torque at the rational surface, a non-linear system of equations can be found.

Chapter 4

Solutions For Coupled NTM-RWM In A Rotating Plasma

In the previous chapter, the derivation of a system of non-linear equations which describes the evolution of a coupled NTM-RWM system was explained. The first step was to establish the coupling mechanism between the two modes- the link is provided by the respective parameters, $\Delta_{L,W}$, for the rational layer where the magnetic island is located, and the resistive wall surrounding the plasma. The island evolution in the rational layer was evaluated, with the contribution from the bootstrap current of particular importance. To close the system, the torque at the rational layer is also determined self-consistently. The resultant equations are shown below

$$4\dot{w} = Re[\Delta_L] + \frac{\hat{\beta}}{w}\left(1 - \frac{w_c^2}{w^2}\right) \tag{4.1}$$

$$2w(\omega - \Omega_L) + Im[\Delta_L] = 0 \tag{4.2}$$

$$(\Omega_0 - f\Omega_L) = Aw^4 Im[\Delta_L] \tag{4.3}$$

where Δ_L is a complex function of γ and ω.

For the following analysis, $\tau \sim 10^{-2}$, corresponding to a choice of $a = 1.0$m, $r_s = 0.5$m, $T_e = 1$keV, and Coulomb logarithm $\ln \lambda = 20$. The equilibrium parameters will be taken as $\epsilon = 0.1$, and $\delta = 5$, unless otherwise indicated.

4.1 No Wall Solution

If there is no wall surrounding the plasma, then this implies that $\tau = 0$. In this situation, the RWM is not a solution of the system- instead, an infinite growth rate is obtained as a solution, which can be interpreted as the ideal kink mode.

However, the NTM is still a solution in this limit, as shown in Figure 4.1. The NTM solutions exhibit the important threshold characteristics which are fundamental to the NTM, as described in Section 3.1.2. For a $\hat{\beta}$ below a critical value, $dw/dt < 0 \quad \forall w$, and so all islands will decay - and thus no islands exist in the plasma. For $\hat{\beta}$ greater than the critical value, there are two solutions for $dw/dt = 0$. These are the equilibrium points for the system. The first equilibrium point is unstable, in that any perturbations from this point cause the island either to shrink or to grow larger (away from the equilibrium point). This equilibrium point is a threshold for the island growth. The size of the island at this equilibrium point will be referred to as the *seed island width* or the *critical island island*. For an island larger than this threshold width, the island will grow because $dw/dt > 0$. It will continue to grow until it reaches the second equilibrium point, which is stable. This corresponds to a large, saturated NTM.

When τ is finite, both RWM and NTM branches are present. If the wall is thin, or has low conductivity, then it can be assumed that $\tau << 1$ and the equations can be solved analytically.

4.2 Limiting Solution For Small Islands

The behaviour of the solutions when the island is small, $w << w_c$, can be considered first. For a traditional NTM, an island of this size would not grow, as it is smaller than the threshold width required for a seed island, as discussed above. Terms can be ordered: $\tau\omega << \tau\gamma \sim \epsilon$ in order to analyse the small island limit.

The bootstrap term in Equation 4.1, which is $\sim \hat{\beta}$, is relatively large at $w < w_c$, and negative. This term must then be balanced by either a large $\dot{w}$ (ie, γ) on the left hand side of Equation 4.1, or by a large value of $Re[\Delta_L]$.

Neglecting $\tau\omega$ in Equation 4.1, the solution branch when γ is large and negative is the stable NTM root of the equations- as shown in Figure 4.1. Specifically, in this limit, $Re[\Delta_L] \sim \delta$ and $\gamma < 0$ for $w < w_c$.

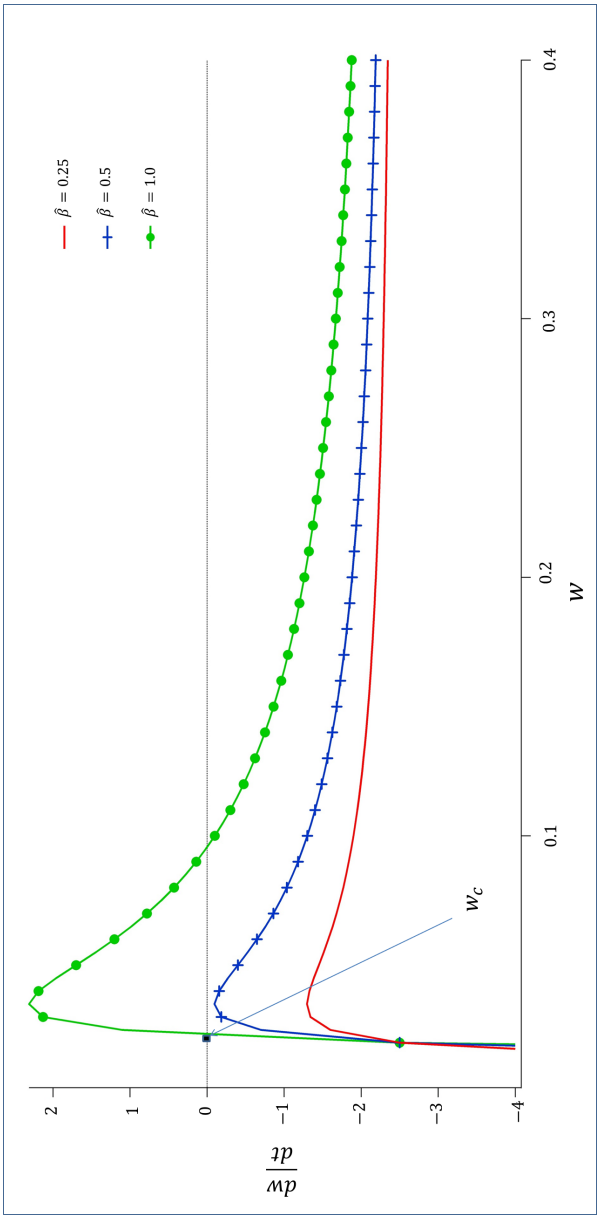

FIGURE 4.1: No RWM exists when the resistive wall is removed: only the NTM solution. The dependence of the island width evolution on $\hat{\beta}$ and w illustrates the behaviour expected for a NTM. This is same behaviour as seen in Section 3.1.2.

The alternative is the RWM solution branch, in which the denominator of $Re[\Delta_L]$ is small. Neglecting the left hand side of Equation 4.1, and balancing $Re[\Delta_L]$ against the bootstrap term, yields a RWM which grows at the rate

$$\tau\gamma = \epsilon - \frac{w}{\hat{\beta}}\left(1 - \frac{w_c^2}{w^2}\right)^{-1} \tag{4.4}$$

Thus, an island such that $w < w_c$ will have $\gamma > 0$ and will grow steadily despite being below the NTM threshold width.

When w approaches w_c, the growth rate is substantially enhanced by the coupling to the bootstrap term. Indeed, as $w \to w_c$, $\tau\gamma \to \infty$, but this is unphysical. The ordering breaks down.

Similarly, with the assumptions that $\omega << \Omega_L$ and $\tau\omega << 1$, the RWM frequency and toroidal rotation frequency can be found.

$$\tau\omega = \frac{2w^3\Omega_0}{(1-\epsilon\delta)\hat{\beta}^2}\left(\frac{w_c^2}{w^2} - 1\right)^{-2}(f + 2Aw^5)^{-1} \tag{4.5}$$

$$\Omega_L = \frac{\Omega_0}{f+2Aw^5} \tag{4.6}$$

Equation 4.6 shows that the plasma rotation at the rational surface, Ω_L, decreases steadily in time from its initial value of Ω_0/f as the island grows. The mode is initially locked to the wall ($\tau\omega = 0$ when $w = 0$), but as the island grows, the mode frequency ω gradually increases. Nevertheless, it remains very small, much less than Ω_L. This is a consequence of Equation 4.4, which implies that $Im[\Delta_L]$ is very large. Since $Im[\Delta_L]$ is directly proportional to the electromagnetic torque at the rational surface,, the electromagnetic torque at $r = r_s$ is very large. Hence there is no rotational stabilisation of the RWM in Equation 4.4. This is different to the model presented in [99], where the bootstrap term is not included. There, the RWM mode frequency rises faster with Ω_L, leading to a suppression of its growth rate as Ω_L increases (the increased mode frequency leads to a stabilising relative rotation between the wall and the mode).

It can be noted that ω is increasingly sensitive to the island width as w approaches w_c. This indicates an unlocking of the island and a dramatic spin-up. Again, as $w \to w_c$, Equation 4.6 predicts $\tau\omega \to \infty$ and the assumed ordering is again broken.

In conclusion, for $w < w_c$, a slowly growing mode which is locked to the wall is found. This is the RWM solution branch. As the island width w approaches w_c, there is a

substantial increase in the growth of the island, and the mode begins to spin up. The small $\tau\gamma$, small $\tau\omega$ ordering fails. As $\tau\gamma$, $\tau\omega$ grow, the full expansion of Δ_L

$$\Delta_L = \frac{(1-\delta\tau\gamma)(\epsilon+\tau\gamma)-\delta\tau^2\omega^2}{(-\epsilon+\tau\gamma)^2+\tau^2\omega^2} + i\frac{\tau\omega(1-\epsilon\delta)}{(-\epsilon+\tau\gamma)^2+\tau^2\omega^2} \tag{4.7}$$

implies that $Im[\Delta_L] \to 0$. The electromagnetic torque which locks the mode to the wall is reduced, and the mode will spin up to rotate with the plasma. Equation 4.3 then indicates that this forces $\Omega_0 - f\Omega_L \approx 0$, meaning that the plasma also spins up towards the initial rotation frequency profile.

4.3 Numerical Solutions To Non-linear System

The non-linear system can be integrated numerically such that the island width w, the mode frequency ω, and the toroidal rotation frequency at the rational surface Ω_L are functions of time. Since the island half width w is related to the mode growth rate by $\gamma = \frac{2\dot{w}}{w}$, the only variable with a time derivative in the non-linear system is w (there is no $\dot{\omega}$ term since inertia was neglected). Thus, the integration in time is carried out on w only. At time step t_i with the interval between time steps δt, the time integration scheme is simply $w(t_{i+1}) = w(t_i) + \delta t * \gamma(t_i)$.

Since the system is non-linear, it is solved numerically. The chosen method is by the Newton-Raphson method. By rearranging the equations such that a vector function F can be written as $\mathbf{F}(\mathbf{x})$, from an initial estimate of $\mathbf{x_0} = (t, w, \omega, \Omega_L)$, an iteration of the method will result in the accurate solution. The inverse Jacobian matrix $\mathbf{J}^{-1}(\mathbf{x})$ for $\mathbf{F}(\mathbf{x})$ is required, and the correction $\delta\mathbf{x}$ required at each iteration to improve the estimate of $\mathbf{x}$) is calculated by

$$\mathbf{J}(\mathbf{x}) \cdot \delta\mathbf{x} = -\mathbf{F}(\mathbf{x}) \tag{4.8}$$

The initial guess for $\mathbf{x}$ needs to be chosen carefully for the Newton-Raphson method to converge on the correct solution. This can be given by the limiting solution of the system, which is described in detail in Section 4.2.

Figure 4.2 shows the comparison between the limiting analytical solutions (Equations 4.4, 4.6 and 4.6) to numerical solutions of the full system, given in Equations 4.1, 4.2 and 4.3. There is good agreement between the analytical and the numerical solutions for small island widths, and then, as expected, the analytic theory fails. Nevertheless,

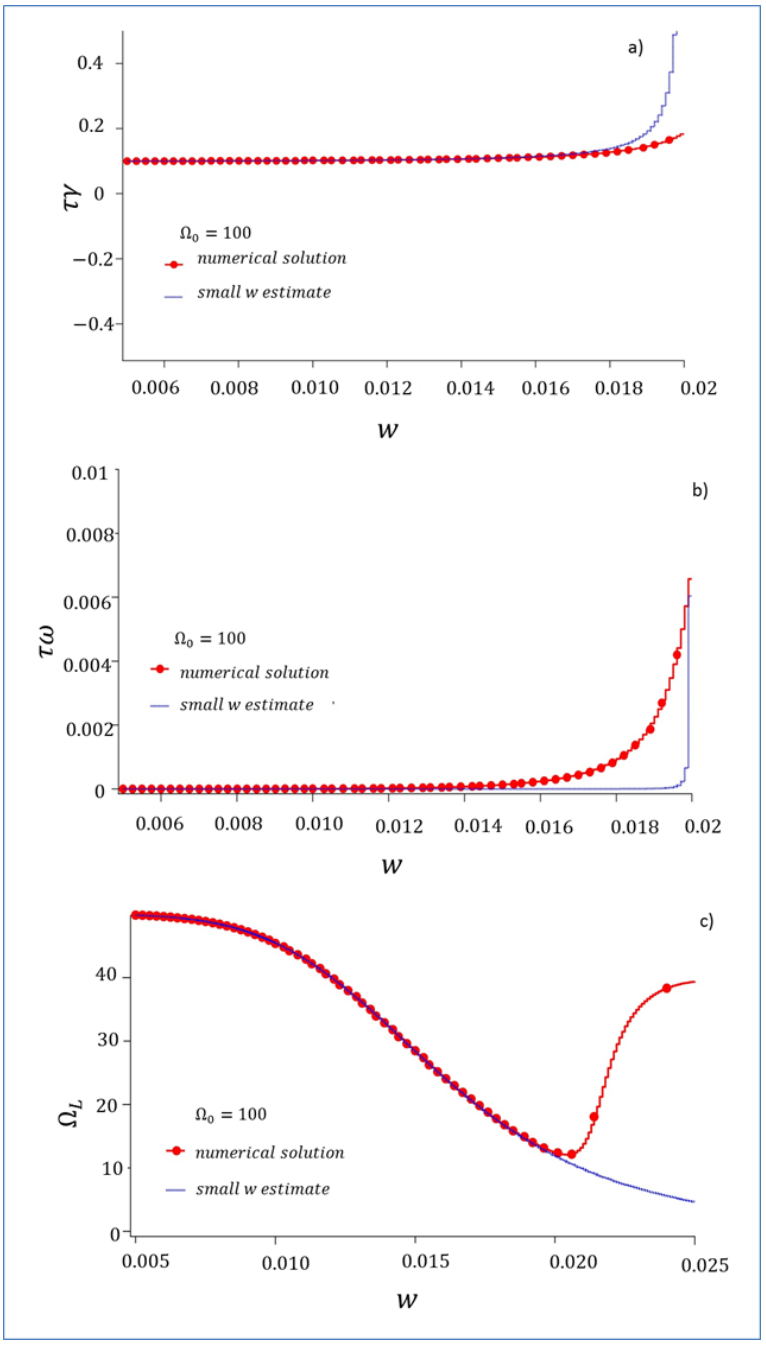

FIGURE 4.2: The comparison of the analytic solutions valid for $w < w_c$ with the numerical solutions of the full system: A and B show both $\tau\gamma$ and $\tau\omega$ increasing rapidly as w passes through w_c. In C, the forced plasma spin-up observed in the numerical solutions is not captured in the analytic approximation. Parameters are fixed at $\Omega_0 = 100$, $w_c = 0.02$ and $\hat{\beta} = 1.0$.

there is strong qualitative agreement, both approaches showing a stronger growth and mode spin-up of the coupled RWM-NTM system as w passes through w_c.

The dependence of the system behaviour on system parameters is also examined numerically.

4.3.1 Dependence on $\hat{\beta}$

If there is zero β, then the NTM has zero drive. In this case, the system finds a conventional RWM as the solution. The mode rotates at a fraction of the plasma rotation, but acting to slow the plasma. The mode eventually locks to the wall. Rotation is expected to be stabilising in this situation [99]. This qualitative behaviour is shown in Figure 4.3 for the lowest value of $\hat{\beta}$: in this model, the RWM behaviour is prevalent for a sufficiently small $\hat{\beta}$.

At sufficiently large $\hat{\beta}$, the RWM couples to a NTM, and takes on a different character.

Numerical solutions for a range of $\hat{\beta}$ values are shown in Figure 4.3. The seed island is given a width $w_{seed} = w_c/4$, such that the NTM solution is stable. However, the solutions show no threshold seed width for the coupled RWM-NTM mode: the mode growth rate is positive for all island widths, however small. In Figure 4.3A, the seed island grows steadily independent of $\hat{\beta}$ as expected for a 'classic' RWM, until it reaches a width w_c. This is consistent with the analytic solution in Equation 4.4, $\gamma = \epsilon/\tau$.

When w increases above w_c, the island growth rate increases dramatically for high $\hat{\beta}$ as the bootstrap term becomes destabilising, providing an additional drive for the mode. This is not captured in the analytic results. If $\hat{\beta}$ is reduced, then the NTM drive is reduced and its effect on the island growth is either reduced or insignificant. The plasma rotation frequency at $r = r_s$, Ω_L, is damped by torque exerted by the unstable RWM, until the island reaches w_c, as shown in Figure 4.3D. The plasma then briefly spins up as the RWM couples to the NTM drive, before again slowing to lock to the wall at large w. Throughout the period for which $w \geq w_c$, the plasma and mode are locked- the mode rotates with the plasma, which is a characteristic of NTMs.

The magnitude of the spin-up in plasma rotation is variable. It depends on the magnitude of $\hat{\beta}$. Since the NTM is driven by $\hat{\beta}$, it is clear that increasing the NTM drive affects the behaviour of the RWM branch. It is possible to remove the plasma spin-up by decreasing $\hat{\beta}$ sufficiently - i.e. by removing drive for the NTM. This is consistent with the picture that the NTM drive is the underlying physics. In Figure 4.3, it can be observed that removing the NTM drive by reducing $\hat{\beta}$ causes the solution to behave

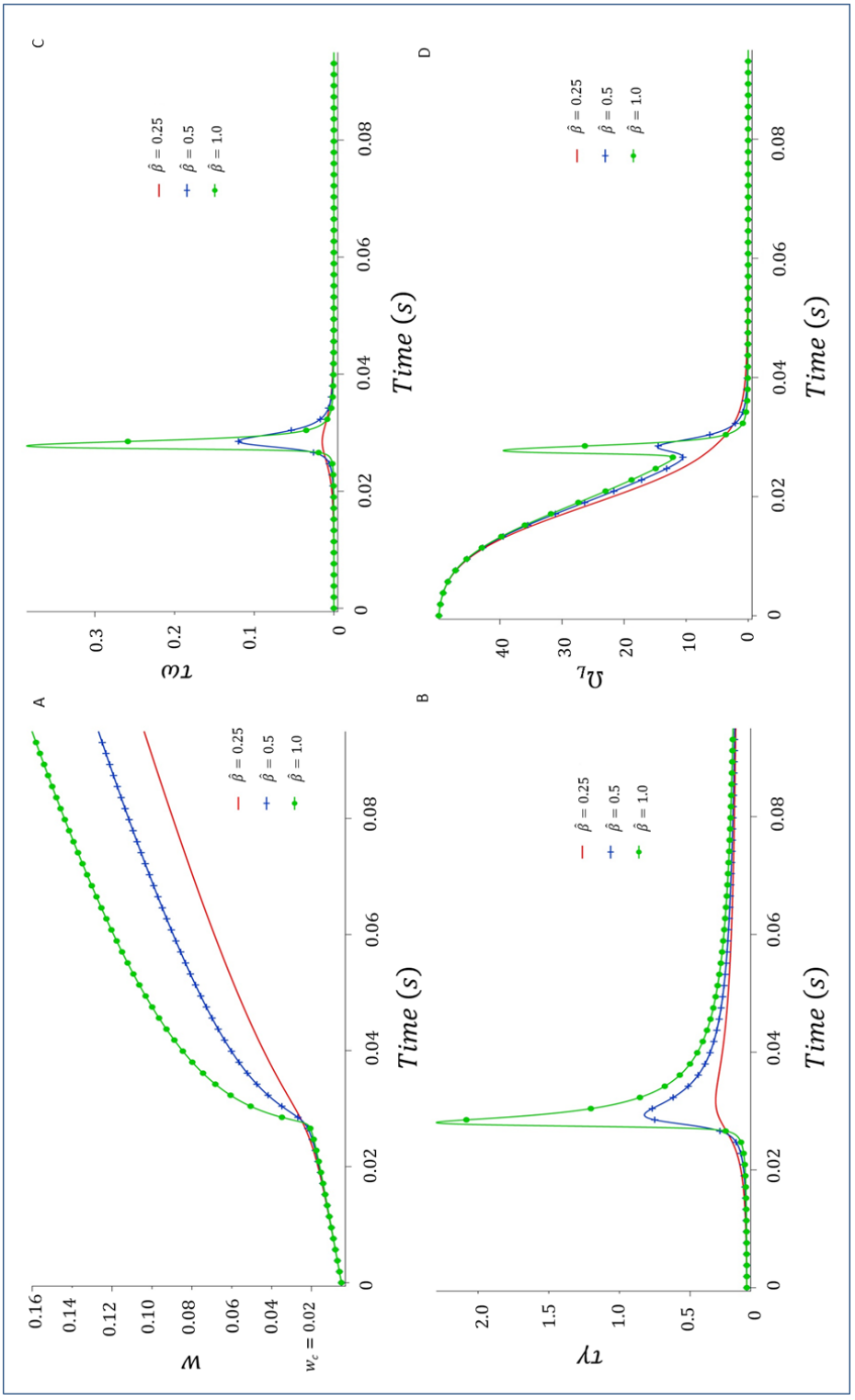

FIGURE 4.3: The initial island, $w(t = 0) = 0.005$, which is considerably smaller than the critical seed island width $w_c = 0.02$. The dependence of the island growth, growth rate γ, mode frequency and plasma rotation frequency at the rational surface on $\hat{\beta}$ is shown: increasing $\hat{\beta}$ increases the NTM drive and allows the island to grow faster and to a larger size.

more as a classic RWM. This would include features such as the wall locking of both the mode and the plasma.

The transient spin-up is a particular feature of the coupled NTM-RWM mode which would distinguish it from other interpretations of experimental observations. This spin-up takes place over a time scale of 3-4 milliseconds for the chosen parameters, which would be detectable: but the effects of including the plasma inertia (which has been neglected in the formulation of the non-linear equations) may be important in determining this time scale. Thus it may be that the actual time scale is rather different.

4.3.2 Dependence on Ω_0

The island evolution is also influenced by the amount of momentum injected into the plasma core, described here by the parameter Ω_0. The effects of the variation of Ω_0 is shown in Figure 4.4.

It is important to note that in this model, the RWM is not sensitive to the plasma rotation, as evidenced by the independence from Ω_0 of the initial evolution of the island width, until $w = w_c$. This is consistent with the analytic solution in Equation 4.4, but differs from models that do not include the NTM drive [99].

The coupling to the NTM is strongly influenced by torque, however. The dramatic increase of island growth rates for $w > w_c$ is only observed at the lowest Ω_0. At higher Ω_0 the mode evolves as a classic RWM which is locked to the wall, with a substantially reduced growth rate compared to the low Ω_0 cases when $w > w_c$.

4.3.3 Equilibrium Parameters

The equilibrium parameters ϵ and δ are determined by the equilibrium of the plasma. They are determined by the outer, ideal MHD region of the plasma. For an equilibrium which is unstable to the RWM but avoids the internal kink, small ϵ and $\delta > 0$ are chosen.

If the value of ϵ is changed, then the stability of the equilibrium to the RWM is altered. Figure 4.5 shows that if ϵ is increased to $\epsilon = 0.3$, then the NTM drive is not coupled to the initial RWM-driven growth of the mode. The island saturates at the NTM threshold width w_c, and the plasma locks to the wall.

If the equilibrium is altered to be stable to ideal modes ($\epsilon = -0.1$), then as expected the initial island shrinks, and is no longer a solution, demonstrated in Figure 4.6. This is because the unstable RWM is no longer present, and cannot drive the island growth.

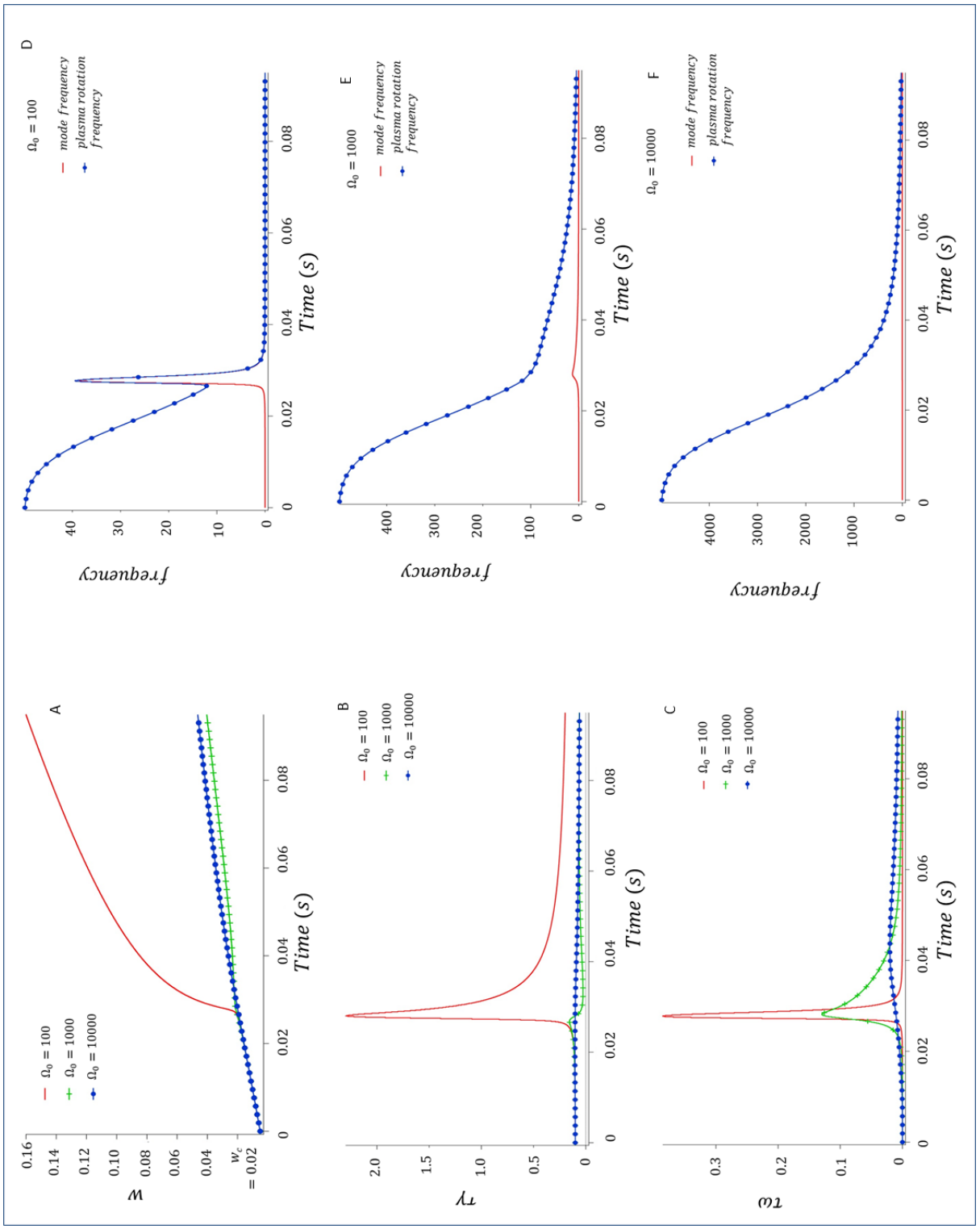

FIGURE 4.4: Initially, $w(t=0) = 0.005$, and $\hat{\beta} = 1.0$. A demonstrates that the initial plasma rotation frequency has a noticeable effect on the island evolution, whereas B and C contrast the mode growth rates and mode frequencies for differing values of Ω_0. D, E and F show the mode and rotation frequencies for the same values of Ω_0. $\Omega_0 = 10^4$ corresponds to the plasma rotating at about 5 % of the plasma sound speed. The spin-up of the plasma only occurs for very small plasma rotation frequencies.

Since the island is below the NTM threshold width, the NTM drive is also inaccessible. The rotation frequency remains unchanged from its initial value, and the mode is locked to the wall.

The parameter δ can also be altered to change the plasma stability when it is surrounded by an ideal wall at $r = r_w$. The results are shown in Figure 4.7. According to Equation 4.4, δ doesn't alter the island behaviour for $w < w_c$, which can be clearly seen in Figure 4.7. The qualitative behaviour of the system for $w > w_c$ is similar, but the change in δ alters the time of onset of the increased growth rate and plasma spin-up. The island grows to its largest size when $\delta = -5.0$, which corresponds to instability to internal kink modes ($\Delta_L < 0$).

4.4 Summary of conclusions

The system of equations 4.1, 4.2 and 4.3 have two solution branches: a NTM with the characteristic thresholds in β and seed island width; and a coupled RWM-NTM branch which has no threshold.

Whilst the RWM-NTM island width is small, below the NTM threshold width, the mode is a 'classic' RWM. The mode grows slowly on a timescale characterised by the wall resistive diffusion time, and is locked to the wall. The plasma rotation gradually slows during this phase.

As the island width exceeds the NTM threshold width, there is a dramatic increase in growth as the mode couples to the NTM drive. This is particularly noticeable at high $\hat{\beta}$. At the same time, the mode unlocks from the wall and instead rotates with the plasma. The plasma rotation increases at this time. The island continues to grow, locked to the plasma flow, which gradually slows to lock to the wall at large island width, This phase has the characteristics of an NTM.

4.4.1 Experimental Observations

In order to be a worthwhile model, the behaviour predicted here should be experimentally testable, as well as distinguishable from other models. Only tokamaks which have a resistive wall and which are capable of demonstrating a resistive wall mode would be able to test this model - for example, the design of spherical tokamaks places the wall sufficiently far from the plasma as to be at infinity. Tokamaks such as DIII-D (Figure 2.8) and JT-60U (Figure 2.9) are capable of analysing RWM behaviour, and DIII-D

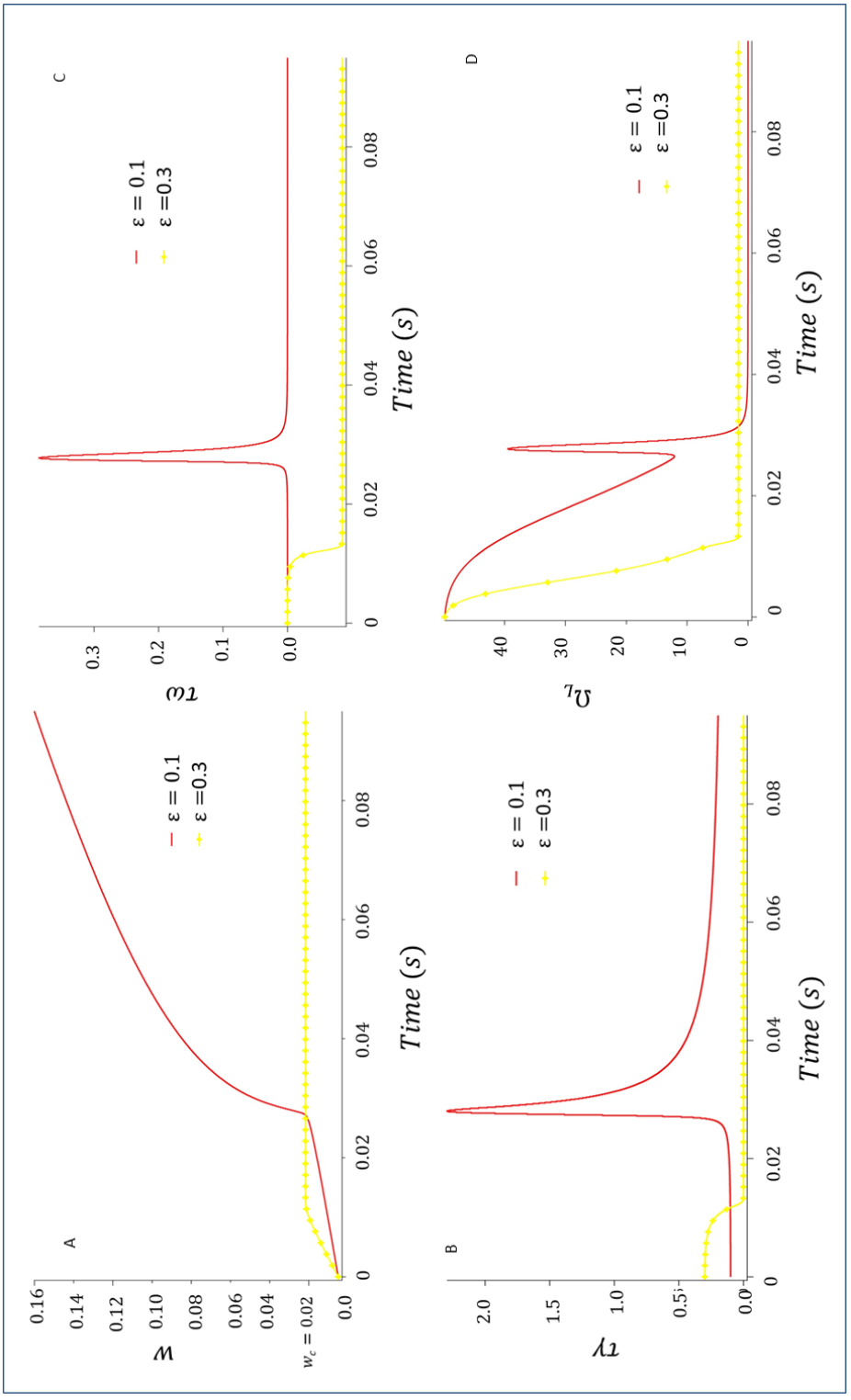

FIGURE 4.5: Comparison of $\epsilon = 0.1$ and $\epsilon = 0.3$ for $\Omega_0 = 100$ and $\hat{\beta} = 1.0$. Changing the equilibrium stability to the RWM changes the island behaviour.

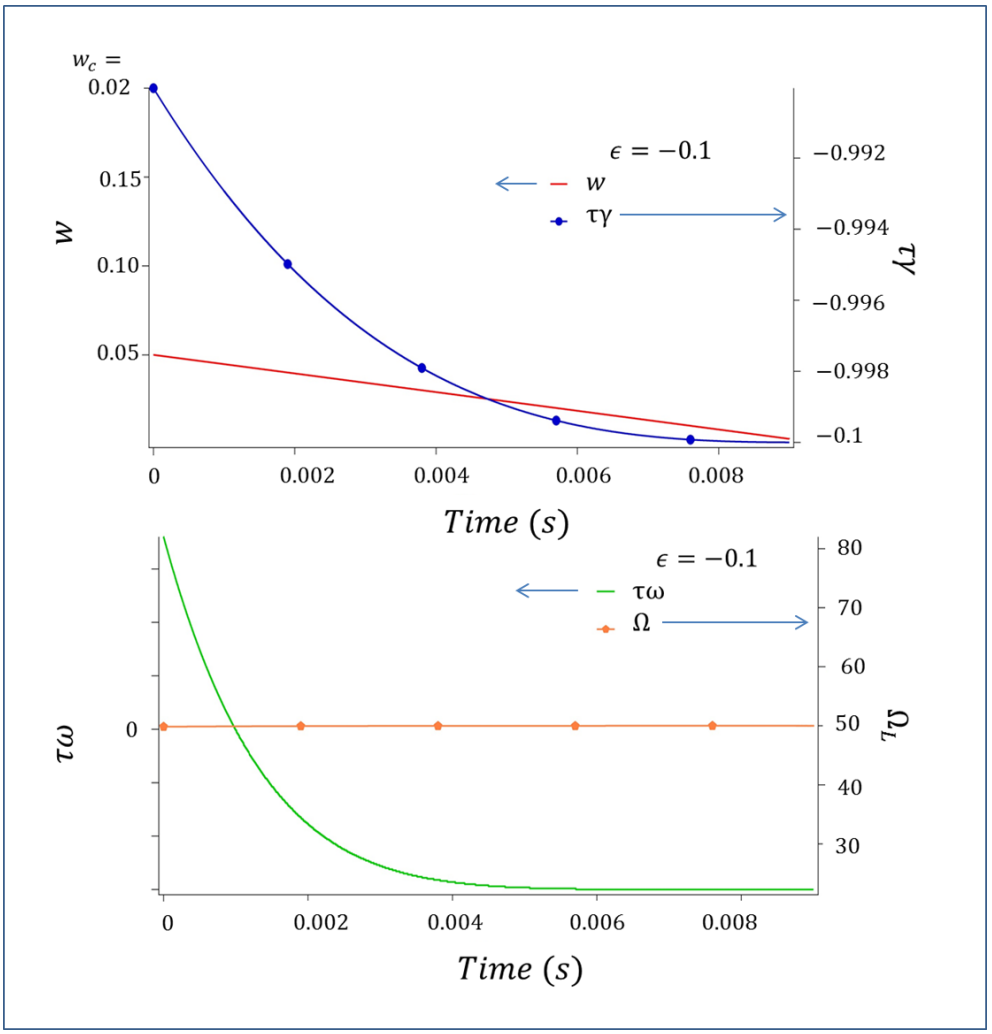

FIGURE 4.6: System behaviour for $\epsilon = -0.1$, and $\Omega_0 = 100$, $\hat{\beta} = 1.0$ The equilibrium is no longer unstable to the RWM, so the initial island shrinks.

is the tokamak where the triggerless NTM studies described above and in [96] were performed.

In the initial phase, the island is below the NTM island threshold ($w \sim 1$cm), and the island is locked to the wall. In this early evolution phase, the coupled RWM-NTM would be difficult to detect experimentally. Mirnov coils fixed to the wall of the tokamak would not observe a dB/dt if the island is locked to the wall.

However, once the island width exceeds the NTM threshold, the mode spins up. This mode spin-up would be detectable by Mirnov coils through the resulting dB/dt. Diagnostics at DIII-D have been used to interpolate island widths, as in Figure 3.4, in this way. At this time, the island would already have a width $w \sim w_c$ and so would have the appearance of a triggerless NTM- a 1cm island which does not appear to have been seeded by other MHD behaviour.

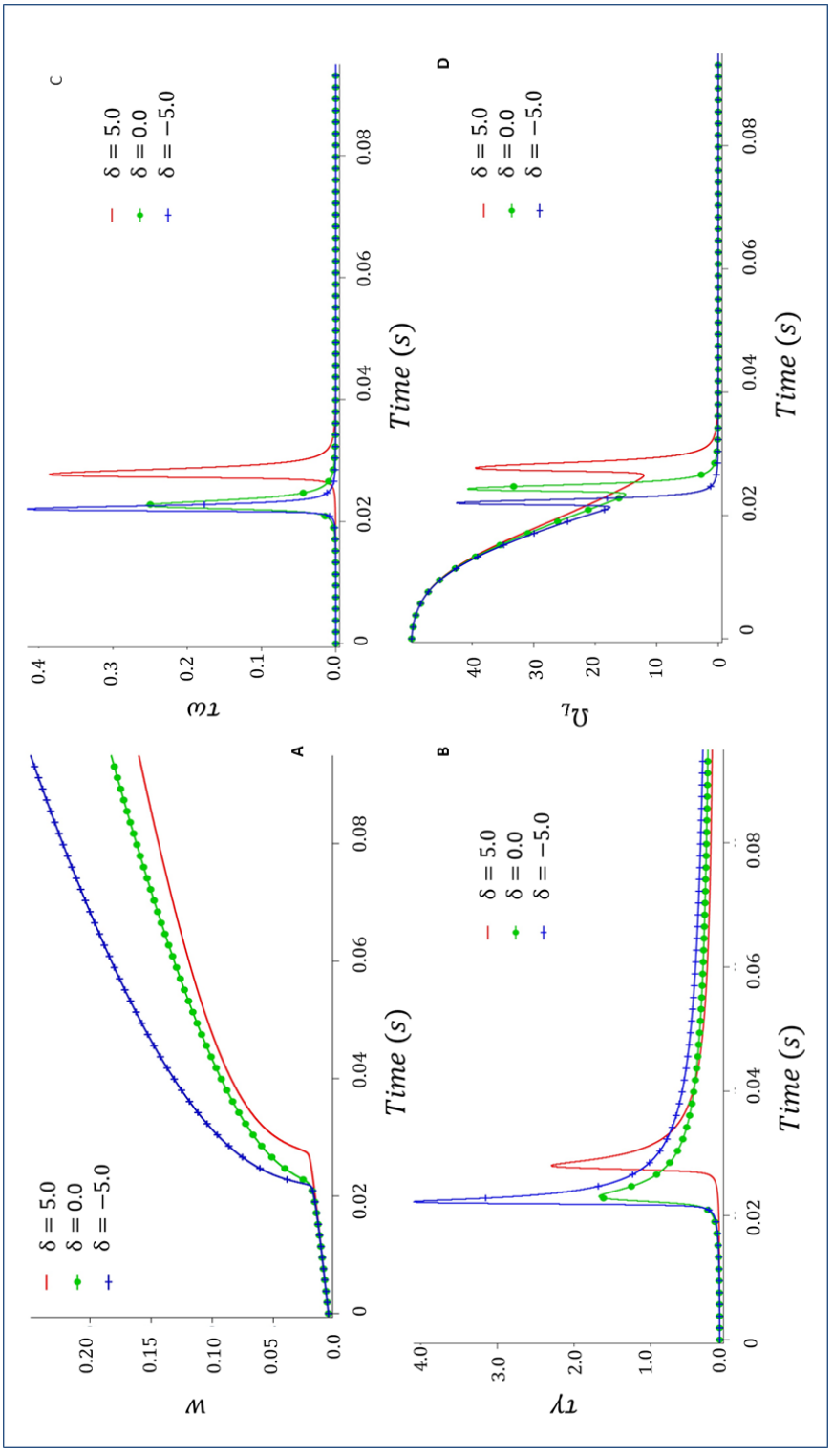

FIGURE 4.7: Scan of differing values of δ for $\Omega_0 = 100$ and $\hat{\beta} = 1.0$. Qualitative behaviour is unvaried but the onset of the NTM-like phase occurs at slightly different times.

One advantage of testing this model at DIII-D would be that existing experimental protocols and expertise for studying triggerless NTMs would be already in place, which would enable the difference between the model described in this thesis, and the model described in [96], to be compared effectively. The plasma β_N would increase towards the no-wall limit, as in [96], avoiding destabilising sawtooth activity. This model predicts that the destabilised RWM would drive island growth until the island width $w \sim w_c$, when the neoclassical bootstrap current would begin to drive the island until saturation. Observations of the island unlocking and subsequent locking would need to be combined with detailed analysis of plasma rotation at the rational surface: although the plasma spin-up may be too fast to be detected, since this model neglects plasma inertia. Control of the plasma rotation in a sequence of experiments would also be beneficial in order to capture any plasma spin-up behaviour.

4.4.2 Contrasting Interpretations Of Triggerless NTMs

The phenomenon of triggerless NTMs near $\beta_N^{no-wall}$, the ideal no-wall β_N limit, can also be explained by using the concept of $\Delta^{'}$. In particular, the behaviour of $\Delta^{'}$ near the no-wall limit, where $\Delta^{'}$ is implemented here as Δ_L/r_s.

As $\beta_N \rightarrow \beta_N^{no-wall}$, then $\Delta^{'} \rightarrow \infty$ ($\Delta_W = 0$ since there is no wall, and $\epsilon \rightarrow 0$). This can cause an NTM to grow, either because a classical tearing mode is destabilised, which in turn destabilises the neoclassical tearing mode when at sufficiently large amplitude; or the threshold island width is lowered for non-linear NTM destabilisation, so that smaller seed islands produced by forced magnetic reconnection at the rational surface caused by other modes are able to grow [96]. This is because the growth rate of the mode becomes very sensitive to equilibrium parameters when $\Delta^{'}$ becomes large, leading to rapid changes in mode stability [103].

In the model derived in this thesis, this would be equivalent to allowing $\Delta_w \rightarrow 0$ and $\epsilon \rightarrow 0$, corresponding to the no-wall ideal MHD stability boundary. The RWM is destabilised for $\beta_N > \beta_N^{no-wall}$, but the pole in Δ_L is resolved by a dependence on the wall response. The physics interpretation is thus somewhat different to that given in [96]. A distinguishing prediction is that, contrary to the model dependent on a pole in $\Delta^{'}$, the plasma is expected to slow in the few tens of milliseconds before the island width reaches the threshold width. Additionally, the plasma spin-up coincident with the appearance of the mode on Mirnov coils, would manifest and last a few milliseconds. However, if the plasma rotation is sufficiently fast, the characteristic mode spin-up does not occur (Figure 4.4F).

4.5 Summary Of Results

The system of non-linear equations found in Chapter 3 is solved for a variety of situations. For a plasma surrounded by no wall, the NTM is found as a solution, and exhibits the typical threshold physics expected of an NTM. If the magnetic island width is small, the equations can be solved analytically. This provides an initial guess for solving the system of equations numerically. In varying system parameters, the behaviour of the coupled mode is seen to be similar to that of a triggerless NTM. Thus, a RWM coupled to an NTM is a possible explanation for observations of triggerless NTMs in tokamak experiments.

Chapter 5

Benchmarking Resistive Walls in JOREK

5.1 Nonlinear MHD Simulations With JOREK

JOREK is a nonlinear code which solves the reduced MHD equations in toroidal geometry. It was developed by G. T. A. Huysmans [104] and originally intended to aid the understanding of ELMs [105, 106]. In the poloidal plane, third order Bézier finite elements are used as the spatial discretisation [107], whereas in the toroidal direction a Fourier decomposition is employed. Thus a 3D model of the plasma can be simulated.

The code is OpenMP and MPI parallelised. The libraries needed include PASTIX [108], Scotch [109] and MUMPS [110].

5.1.1 JOREK Equilibrium

JOREK incorporates the HELENA equilibrium solver [111]. The code requires primarily the density, temperature and FF' profiles (where $F = RB_\phi$ [3]) and the plasma geometry as inputs. In addition to minor and major radii, the computational boundary is defined by either (R,Z,Ψ) coordinates (Ψ is poloidal flux) or ellipticity, triangularities and quadrangularities.

After initialisation, JOREK defines the computational boundary and the initial grid for solving the equilibrium. JOREK then solves the Grad-Shafranov equation in weak form. The weak form of Equation 5.1 is found my multiplying 5.1 by a test function (usually a basis function to simplify integration) and integrated over the calculation domain. This technique allows for higher order derivatives to be reduced by integration by parts, such

that the equation to be solved does not include any derivative of the function that is being solved for. This allows solutions which may not be smooth to be found.

$$R\frac{\partial}{\partial R}\left(\frac{1}{R}\frac{\partial \Psi}{\partial R}\right)+\frac{\partial^2 \psi}{\partial Z^2}=-R^2\frac{\partial p}{\partial \Psi}-F\frac{\partial F}{\partial \Psi} \tag{5.1}$$

where (R,Z) are coordinates in the poloidal plane and p is pressure.

When the flux surfaces have been calculated, the grid is adjusted to align with the flux surfaces.

5.1.2 Reduced MHD Equations

JOREK evolves the equilibrium in time, solving the reduced MHD equations. The reduced MHD equations are as follows:

- Poloidal Flux Equation,

$$\frac{1}{R^2}\frac{\partial \Psi}{\partial t}=\eta(T)\nabla\cdot\left(\frac{1}{R^2}\nabla_\perp\Psi\right)=\frac{1}{R}[u,\Psi]-\frac{F_0}{R^2}\frac{\partial u}{\partial \phi}$$

- Poloidal Momentum Equation,

$$\hat{\mathbf{e}}_\phi\cdot\nabla\times\left(\rho\frac{\partial \mathbf{v}}{\partial t}=-\rho(\mathbf{v}\cdot\nabla)\mathbf{v}-\nabla(\rho T)+\mathbf{J}\times\mathbf{B}+\mu\Delta\mathbf{v}\right)$$

- Toroidal Current Equation,

$$j=\Delta^*\Psi$$

- Vorticity Equation,

$$\omega=\nabla_\perp^2 u$$

- Density Equation,

$$\frac{\partial \rho}{\partial t}=-\nabla\cdot(\rho\mathbf{v})+\nabla\cdot(D_\perp\nabla_\perp\rho)+S_p$$

- Temperature Equation

$$\rho\frac{\partial T}{\partial t}=-\rho\mathbf{v}\cdot\nabla T-(\kappa-1)\rho T\nabla\cdot\mathbf{v}+\nabla\cdot(K_\perp\nabla_\perp T+K_\parallel\nabla_\parallel T)+S_T$$

- Parallel Momentum (only if selected by choice of JOREK model)

$$\mathbf{B} \cdot \left(\rho \frac{\partial \mathbf{v}}{\partial t} = -\rho(\mathbf{v} \cdot \nabla)\mathbf{v} - \nabla\rho + \mathbf{J} \times \mathbf{B} + \mu\Delta\mathbf{v} \right)$$

where η is plasma resistivity, T is plasma temperature, u is the stream function, $\mathbf{v}$ is velocity, ρ is density, $\mathbf{J}$ is current density, $\mathbf{B}$ is magnetic field, $\Delta^* = R^2\Delta \cdot (R^{-2}\nabla)$, j is toroidal current density, ω is vorticity, S_ρ is a density source, κ the ratio of specific heats, and S_T is a temperature source. K is the transport coefficient, and D is particle diffusivity.

The magnetic field is defined as

$$\mathbf{B} = \frac{F_0}{R}\hat{\mathbf{e}}_\phi + \frac{1}{R}\nabla\Psi \times \hat{\mathbf{e}}_\phi$$

and the flow as

$$\mathbf{v} = -R\nabla u \times \hat{\mathbf{e}}_\phi + v_\parallel \mathbf{B}$$

The weak form of each equation is calculated: as with Equation 5.1, test functions equivalent to the JOREK basis functions - Bézier and Fourier basis functions [112]- are chosen, and any higher derivatives can be reduced by partial integration. The physical quantities are also expanded in the basis functions. Integrals are carried out by Gauss quadrature in element-local coordinates in the poloidal plane and by Fast Fourier Transform toroidally. This results in a linear system of equations, which can be represented as a large sparse matrix. The time stepping is a Crank-Nicholson scheme.

5.2 Coupling JOREK And STARWALL

The default boundary conditions for simulations using JOREK are fixed: the JOREK computational domain is surrounded by an ideally conducting wall. In the equations solved by JOREK, the only place the boundary response is invoked is in the current equation. Fixed boundary conditions cause the integral around the boundary in the current equation to disappear. When implementing the free boundary conditions, this boundary integral remains finite.

5.2.1 STARWALL

The STARWALL code [113] solves the magnetic field equation in a vacuum (as a Neumann-like problem). The code can do this in the presence of 3D conducting structures (generally referred to collectively as the "wall") which can include holes, coils and other 3D structures. This allows the inclusion of realistic wall geometry, and modelling MHD stability in machine-specific configurations.

The wall is modelled as infinitely thin triangles with the wall current potentials assumed to be constant over each wall triangle. The wall is also characterised by its effective resistance η_w/d_w where η_w is the wall resistivity (JOREK-normalised) and d_w the wall thickness. Since the wall current potentials are assumed to be constant over a wall triangle, they can be described by the wall current potentials Y_k on the triangle nodes.

STARWALL has also been coupled to the CASTOR MHD code to perform linear stability studies with a resistive wall [114].

5.2.2 Boundary Conditions

In the coupling of STARWALL to JOREK, the boundary condition is given by the component of the magnetic field normal to the boundary of the JOREK computational domain in the poloidal plane. This boundary is often referred to as the *interface* [115]. STARWALL generates response matrices for the specified 3D wall structure which can be used to express the magnetic field component tangential to the interface in terms of the normal component.

5.2.3 Implementing The Boundary Integral

The implementation of the boundary integral in JOREK was carried out by M. Hölzl. The vacuum response provided by STARWALL is needed only when implementing the current equation

$$j = \Delta^* \Psi \tag{5.2}$$

where the operator $\Delta^* = R^2 \nabla \cdot (R^{-2} \nabla)$. The equations are written in weak form, with the basis functions acting as the test functions j_*. These basis functions are the 1D Bezier basis function in the poloidal direction on the interface, or the Fourier basis function in the toroidal direction. From the weak form (Equation 5.3) of the current equation,

$$\int dV \frac{j_*}{R^2}(j - \Delta^*\Psi) = 0 \tag{5.3}$$

integration by parts of the Δ^* term obtains

$$\int dV \frac{j_*}{R^2} j + \int dV \frac{1}{R^2} \nabla j_* \cdot \nabla\Psi - \oint dA \frac{j_*}{R}\left(\nabla\Psi \cdot \frac{\hat{\mathbf{n}}}{R}\right) = 0 \tag{5.4}$$

where $\hat{\mathbf{n}}$ is the unit vector normal to the interface.

The definition of the magnetic field in JOREK is given by

$$\mathbf{B} = \frac{F_0}{R}\hat{\mathbf{e}}_\phi + \frac{1}{R}\nabla\Psi \times \hat{\mathbf{e}}_\phi \tag{5.5}$$

B_{tan} can be expressed as $(\mathbf{B} \times \hat{\mathbf{n}}) \cdot \hat{\mathbf{e}}_\phi$, and substituting Equation 5.5 into this expression gives [115]

$$B_{tan} = -\frac{1}{R}\hat{\mathbf{e}}_\phi \cdot [\hat{\mathbf{n}} \times (\nabla\Psi \times \hat{\mathbf{e}}_\phi)] \tag{5.6}$$

Since $(\hat{\mathbf{n}} \cdot \hat{\mathbf{e}}_\phi) = 0$,

$$B_{tan} = \frac{1}{R}\hat{\mathbf{n}} \cdot \nabla\Psi \tag{5.7}$$

Hence the final term of Equation 5.4 contains B_{tan} in the integrand.

$$\oint dA \frac{j_*}{R}\Bigg(\underbrace{\nabla\Psi \cdot \frac{\hat{\mathbf{n}}}{R}}_{=B_{tan}}\Bigg) = 0 \tag{5.8}$$

In fixed boundary conditions, this boundary integral vanishes.

Ideal Wall Boundary Condition

When the wall is ideal, the wall current potentials can be expressed directly as functions of the poloidal flux boundary values. The poloidal flux boundary values are used for practical reasons instead of the normal field component. The normal field component can be calculated from Ψ, which at the interface is $\Psi = \sum_j b_j \Psi_j$, where b_j are the basis functions and Ψ_j the poloidal flux coefficients. Then B_{tan} can be written

$$B_{tan} = \sum_i b_i B_{tan,i} = \sum_i b_i \sum_j \hat{M}^{id}_{i,j} \Psi_i \tag{5.9}$$

with $\hat{M}^{id}$ the STARWALL-calculated ideal wall response matrix. The wall current potentials Y_k are not considered explicitly.

Resistive Wall Boundary Condition

For a resistive wall, the wall current potentials are considered.

$$B_{tan} = \sum_i b_i \Big(\sum_j \hat{M}^{ee}_{i,j} \Psi_j + \sum_k \hat{M}^{ey}_{i,k} Y_k \Big) \tag{5.10}$$

$\hat{M}^{ee}$ and $\hat{M}^{ey}$ are the STARWALL resistive response matrices. The wall current potentials also evolve in time,

$$\dot{Y}_k = -\frac{\eta_w}{d_w} \hat{M}^{yy}_{k,k} Y_k - \sum_j \hat{M}^{ey}_{i,k} \Psi_j \tag{5.11}$$

with $\hat{M}^{yy}$ and $\hat{M}^{ey}$ also STARWALL matrices.

By taking $\eta_w \to 0$, it is clear that $\hat{M}^{id}_{i,j} \equiv \hat{M}^{ee}_{i,j} - \sum_k \hat{M}^{ey}_{i,k} \hat{M}^{ye}_{k,j}$. Similarly, by letting $Y_k \to 0$, the no-wall response matrix $\hat{M}^{nw}_{i,j}$ can be found to be identical to $\hat{M}^{ee}_{i,j}$.

Equations 5.10 and 5.11 are discretised in time to be evaluated at the next time step. The boundary integral is integrated, as all the integrals, with Gauss quadrature.

Poloidal Field Coil Contribution

To incorporate poloidal coils, which is necessary for correctly assessing the n=0 component, Equation 5.10 is replaced by

$$B_{tan} = \sum_i b_i \Big(\sum_j \hat{M}^{ee}_{i,j} (\Psi_j - \Psi^{coil}_j) + \sum_k \hat{M}^{ey}_{i,k} Y_k + B^{coil}_{tan,i} \Big) \tag{5.12}$$

where Ψ^{coil}_j and $B^{coil}_{tan,i}$ are time independent coil contributions to the poloidal flux and B_{tan} at the interface.

Free Boundary In The Grad-Shafranov Equation

A boundary integral similar to Equation 5.4 is found in the weak form of the Grad-Shafranov equation. In solving the Grad-Shafranov equation to establish the plasma equilibrium, only the n=0 component (poloidal field coil contribution) needs to be considered. This is due to the axisymmetric JOREK equilibrium. Also, no time discretisation is needed for this particular use of the STARWALL coupling.

5.3 Benchmarking JOREK-STARWALL

The implementation of the JOREK-STARWALL coupling necessitated rigourous benchmarking of the treatment of the resistive wall [115]. Benchmarking against the linear MHD code CEDRES++ [116], was carried out by Hölzl et al. In order to validate the n=0 component, the free boundary equilibrium of an ITER-like limiter plasma was computed by JOREK and compared to the same equilibrium computed by CEDRES++. It was found that the results agreed well, with small differences ascribed to the discretisation of the poloidal field coils.

Additionally, an n=2, m=1 tearing mode in a circular, large aspect ratio plasma with uniform plasma resistivity and surrounded by an ideally conducting wall was investigated [117]. Very good agreement between JOREK and CASTOR was observed. In addition, treating the problem as a resistive wall with zero resistivity as opposed to an ideal wall- the same problem but different implementation- achieved exactly the same results, showing the consistency of the code coupling.

Benchmarking of the resistive wall implementation against an analytical treatment of the Resistive Wall Mode was also carried out, and is described in the following sections.

5.3.1 Linear Analysis Of RWM

The growth rate of the ideal kink in a cylindrical plasma of circular cross section, can be calculated analytically [118]. The calculation for ideal kink stability in a cylindrical equilibrium with the following characteristics is fairly well known. It is a typical equilibrium for studying RWMs: both the control of the mode as well as stability. The wall is assumed to be resistive, of thickness d at radius $r_w > a$, where a is the plasma minor radius.

The plasma current is a channel, where $\mathbf{J} = J_z\hat{z}$. The step function is characterised by the parameter r_0 such that

$$J_z(r) = \begin{cases} J_0 & r \leq r_0 \\ 0 & r > r_0 \end{cases}$$

where $r_0 < a$ is the width of the current channel. We also assume zero pressure in the plasma, and a step function for the plasma density with the step located at the same r_0 as the current density profile. From the expression of the current density, the poloidal magnetic field and the safety factor profile can be calculated (with a constant toroidal field $B_z(r) = B_0$). The safety factor is constant at $q_0 = 2B_0/(R\mu_0 J_0)$ within the radius of the current channel, and then increases parabolically to the edge of the plasma.

$$q(r) = \begin{cases} q_0 & r \leq r_0 \\ q_0 \frac{r^2}{r_0^2} & r > r_0 \end{cases}$$

Following the calculation found in [118], and assuming modes of the form

$$\psi(r, \theta, z) = \psi(r) \exp^{im\theta - inz/R}$$

with m, n the poloidal and toroidal mode numbers respectively, and ψ the perturbed flux. The torque balance equation can be calculated from the z component of the curl of the perturbed momentum balance equation.

$$\nabla_\perp^2 \psi - \frac{\mu_0 m}{B_\theta (m - nq)} \frac{dJ_z}{dr} \psi = i\gamma \frac{\mu_0 r}{B_\theta (m - nq)} \nabla \times (\rho \mathbf{v}) \cdot \hat{z} \tag{5.13}$$

where ρ is the plasma density and $\mathbf{v}$ the plasma velocity. Assuming an incompressible, ideal plasma, and using Faraday's law, it is possible to expand the right hand side of Equation 5.13 to obtain

$$\nabla_\perp^2 \psi - \frac{\mu_0 m}{B_\theta (m - nq)} \frac{dJ_z}{dr} \psi = i\gamma \frac{\mu_0 r}{B_\theta (m - nq)} \rho \nabla_\perp^2 \left[\frac{r\psi}{B_\theta (m - nq)} + \frac{d\rho}{dr} \frac{d}{dr} \left(\frac{r\psi}{B_\theta (m - nq)} \right) \right] \tag{5.14}$$

Equation 5.14 is reduced to $\nabla_\perp^2 \psi = 0$ for $0 \leq r < r_0$ and $r_0 < r \leq a$: this is the vacuum equation for ψ. The jump condition

$$\frac{r\psi'}{\psi}\bigg|_{r_0} + \frac{2m}{m - nq_0} = (\gamma \tau_A)^2 \frac{q_0^2}{(m - nq_0)^2} \frac{r\psi'}{\psi}\bigg|_{r_0^-} \tag{5.15}$$

is calculated by integrating Equation 5.14 across the jump at $r = r_0$, where $\tau_a = \sqrt{\mu_0 \rho_0} R/B_0$, and ρ_0 is the plasma density at the plasma centre.

For a resistive wall located at $r_w > a$, the second jump condition is given by

$$\left.\frac{r\psi'}{\psi}\right|_{r_w} = 2\gamma\tau_w \tag{5.16}$$

where $\tau_w = \mu_0 \sigma r_w d/2$, σ the wall conductivity. τ_w is defined [118] as the field penetration time for the m=1 mode.

Equations 5.14, 5.15, and 5.16 combine to give an equation for the growth rate of the RWM [118]

$$\frac{\nu}{m - nq_0} - \frac{1}{1 - \frac{\gamma\tau_w}{(\gamma\tau_w + \mu)}\left(\frac{r_0}{r_w}\right)^{2\mu}} = \frac{(\gamma\tau_A)^2}{2}\frac{q_0^2}{(m - nq_0)^2} \tag{5.17}$$

where ν =sgn(m), $\mu = |m|$.

It is possible to neglect the effect of plasma inertia with the ordering $\gamma\tau_A << 1$, $\gamma\tau_w \sim 1$. However, the inertia contribution will be included in the benchmarking. The inertia contribution is essential to capture the behaviour of the plasma when the wall radius is large. Equation 5.17 is cubic, with one primary root corresponding to the RWM, and two complex conjugate roots to the plasma mode.

No-Wall Limit

In the no-wall limit, $\tau_w = 0$ (or $r_w \to \infty$). The ideal kink should be unstable, which leads to the condition

$$m - \nu < nq_0 < m \tag{5.18}$$

Ideal Wall Limit

In the ideal wall limit, $\tau_w \to \infty$, with the wall location at $r = r_w$. The wall radius r_w^{ideal} at which the ideal kink is found to be marginally stable (i.e. $\gamma = 0$) is given by

$$r_w^{ideal} = r_0\left(1 - \frac{(m - nq_0)}{\nu}\right)^{-\frac{1}{2\mu}} \tag{5.19}$$

For wall radii $r_w > r_w^{ideal}$, the ideal kink will be unstable. For these radii, the plasma inertia contribution to Equation 5.17 is necessary.

The toroidal mode number will be taken as $n = 1$, and $m = 2$ was discovered to be the most unstable poloidal mode number for this analytic equilibrium.

5.3.2 JOREK Equilibrium

The equilibrium used in the derivation of the dispersion relation 5.17 was reproduced in JOREK. The linear growth rate is calculated by JOREK in JOREK-normalised units during the linear growth phase of the simulation.

The plasma has a circular cross section, and an aspect ratio $R/a = 10$. The aspect ratio is sufficiently large for a comparison to Equation 5.17, which was derived in a cylindrical plasma.

As an input parameter profile, JOREK accepts the FF' profile. To reproduce the current channel, a stepped FF' profile is used. The profile is not fully a step function since the discontinuity at $r = r_0$ would be difficult numerically. Thus, the step is slightly smoothed to avoid this difficulty. The level of smoothing employed was tested, but the simulations were found to be insensitive to the smoothing.

The poloidal cross section of the plasma, showing the current channel, is shown in Figure 5.1.

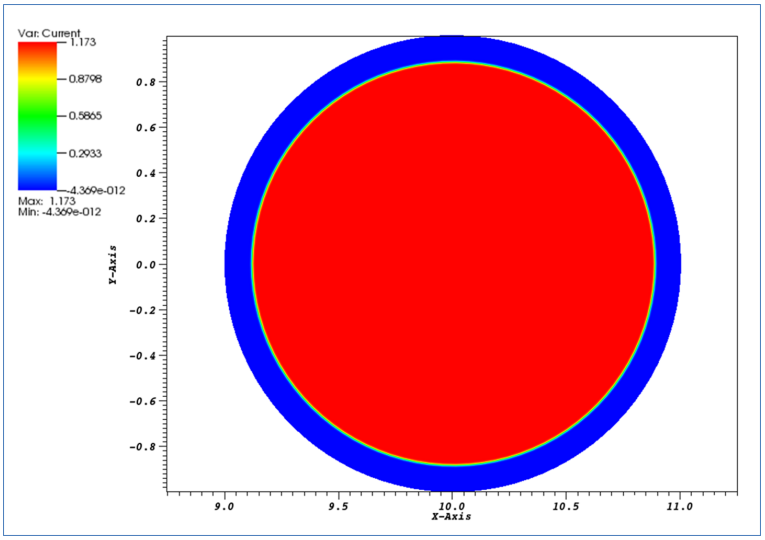

FIGURE 5.1: The poloidal cross section of the current density in the JOREK equilibrium showing the current channel.

Similarly for the stepped density profile, the discontinuity in the simulated step function is smoothed to avoid numerical problems. The temperature profile is very close to zero. This is to approximate the zero pressure assumption used in the analytical analysis, however the temperature profile is also stepped. The vacuum in the implementation of

JOREK is sensitive to the plasma resistivity on the boundary, and it is preferable to have a higher resistivity at that location. The resistivity profile, which is dependent on the temperature profile, is thus ensured to have low resistivity in the centre of the plasma, and higher resistivity at the boundary. The other dissipation terms in the JOREK input are small.

As a measure of how accurate the JOREK equilibrium is, the safety factor profiles in both the analytical equilibrium and the JOREK equilibrium can be compared. This is shown in Figure 5.2. Although the JOREK profile is not constant for $r < r_0$, the variation is small. The safety factor at the edge does not quite match the analytical calculation.

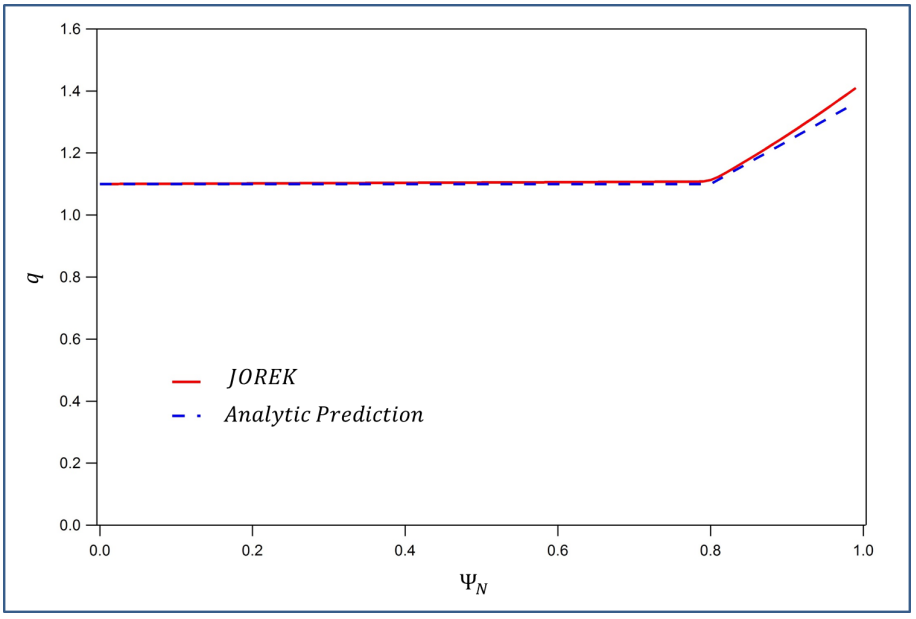

FIGURE 5.2: The comparison between the safety factor profile in JOREK and the analytic profile shows a good agreement between the two.

An individual STARWALL response matrix is required for each of ten wall radii from $r_w = 1.1$m to $r_w = 8.0$m, whereas the wall resistivity can be chosen separately in the JOREK input. Only n=1 modes are included in the simulations. The time taken to enter the linear growth phase is dependent on the wall radius.

5.4 Benchmarking Results

When comparing the JOREK and the analytic growth rates, it is important to take into account both the JOREK normalisation of the growth rates, and also the coordinate system being used. In the construction of the parameter profiles in Section 5.3.1, the

radial coordinate is r. However, in JOREK the parameter profiles are specified with ψ_N, the normalised poloidal flux, as the radial coordinate. Thus a step in the current at $r = r_0$ in the analytic equilibrium needs to be matched to a step at the correct $\psi_N = \psi_{N,0}$ in JOREK. In the following results, $q_0 = 1.1$ and the current and density steps are located at $\psi_{N,0} = 0.8$.

Ideal Wall Benchmarking

The radius at which an ideal wall will stabilise the ideal kink for the choice of equilibrium parameters used in the JOREK simulations can be calculated using Equation 5.19. This radius is found to be $r_w^{ideal} \sim 1.59$. JOREK simulations with an ideal wall at varying wall radii were performed: the results are shown in Figure 5.3.

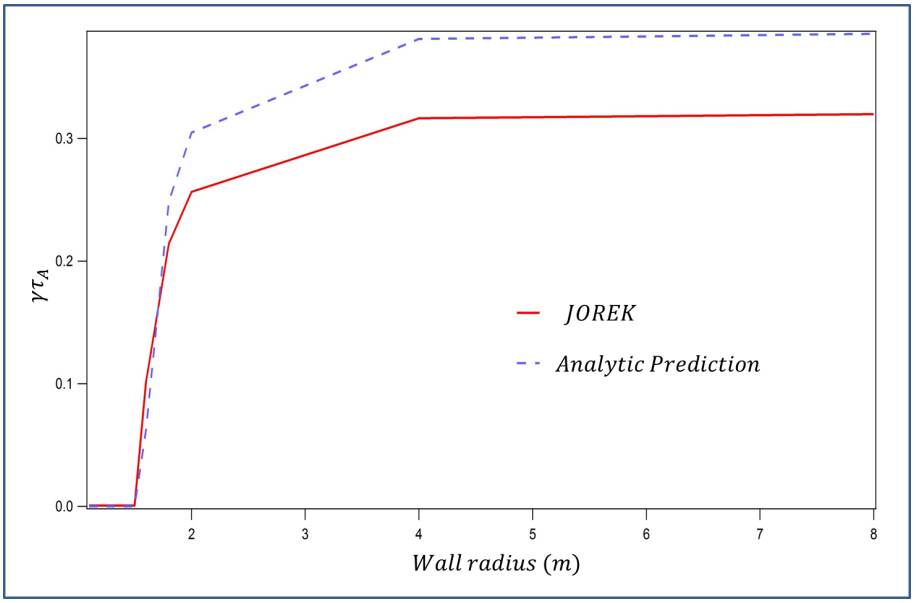

FIGURE 5.3: Comparison of JOREK and analytic predictions for ideal kink growth rates. The marginal wall radius at which the ideal kink is stabilised is found in JOREK.

The marginal wall radius r_w^{ideal} in JOREK is found to agree with Equation 5.19. The JOREK simulations calculate a slightly lower growth rate than the analytic prediction (especially at large wall radius), but exhibit the correct behaviour. This implies that JOREK does not agree with the analytic results in the absence of the wall, but does not imply that the implementation of the resistive wall in JOREK is incorrect. The difference between analytic and JOREK growth rate is not constant, so normalisation is not the issue here.

5.4.1 Resistive Wall Benchmarking

The ideal wall was replaced with a resistive wall, with resistivities ranging from $2.5 \times 10^{-1}\Omega$m to $2.5 \times 10^{-6}\Omega$m. Figure 5.4 shows the JOREK growth rates for the full range of wall radii. The growth rates show the expected behaviour for a RWM as the resistive wall is moved further from the plasma: the stabilising influence of the wall is reduced and the growth rate increases, levelling out as the wall moves to infinity. Additionally, the more resistive the wall is, the greater the stabilising influence it exerts on the plasma, as the perturbed magnetic flux is increasingly unable to penetrate the wall.

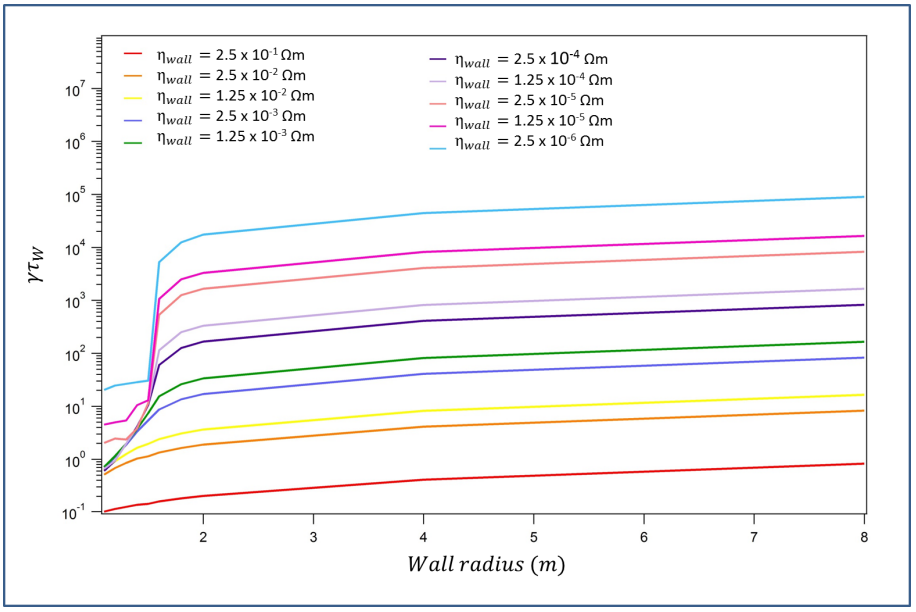

FIGURE 5.4: Full benchmarking results over a range of wall resistivities and radii

The JOREK growth rates can be compared to the calculated growth rates, using Equation 5.17. A comparison between the analytical and JOREK growth rates can be seen for two different wall resistivities in Figures 5.5 and 5.6. The agreement is reasonably good: it can be noticed in Figure 5.6, at the lower wall resistivity, a lack of agreement when the wall is located close to the plasma edge.

This deviation from the analytical growth rate calculation can be attributed to the resolution of STARWALL. However, doubling the resolution of STARWALL from 16 to 32 poloidal grid points had no effect on the linear growth rate in JOREK, so we cannot be sure this is the explanation.

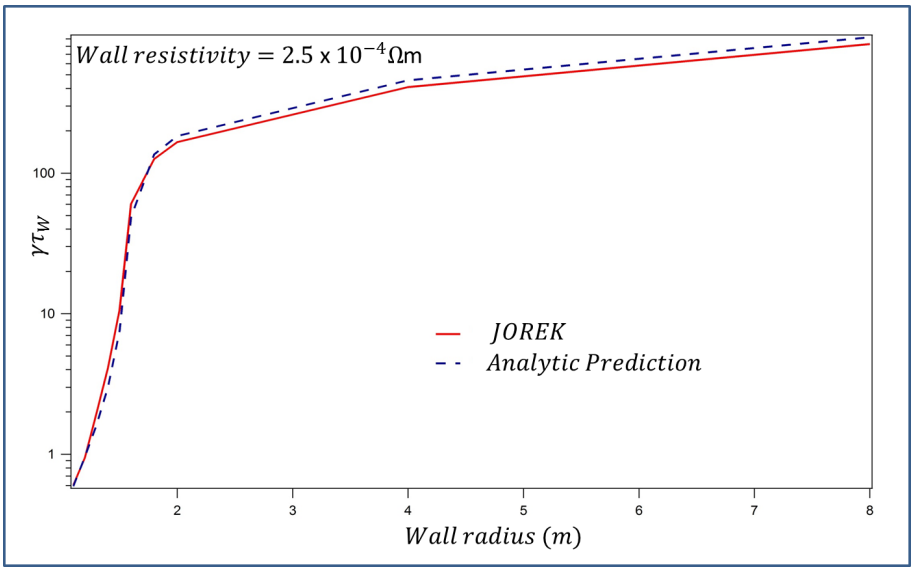

FIGURE 5.5: The analytic and JOREK simulation growth rates are, for this wall resistivity, very good.

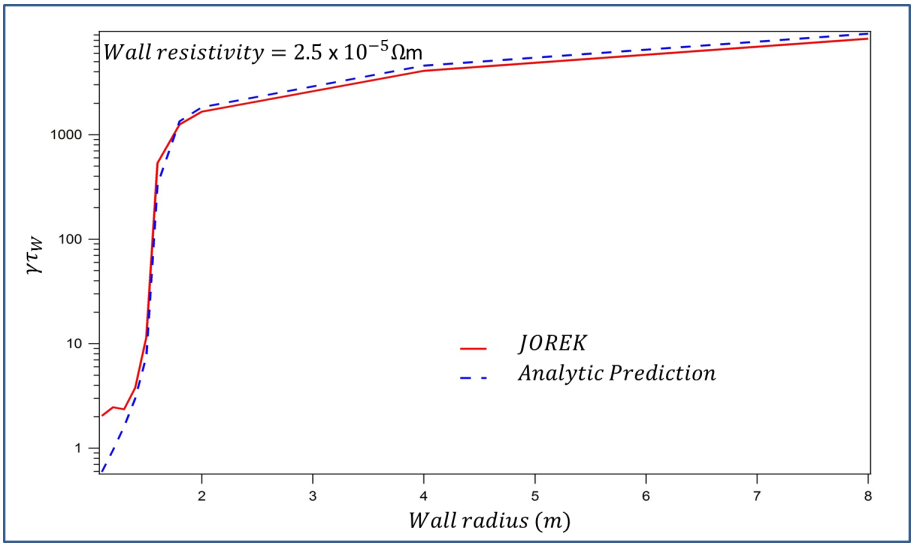

FIGURE 5.6: At smaller wall radii, JOREK finds larger growth rates than the analytic estimate, but only when the resistivity is low.

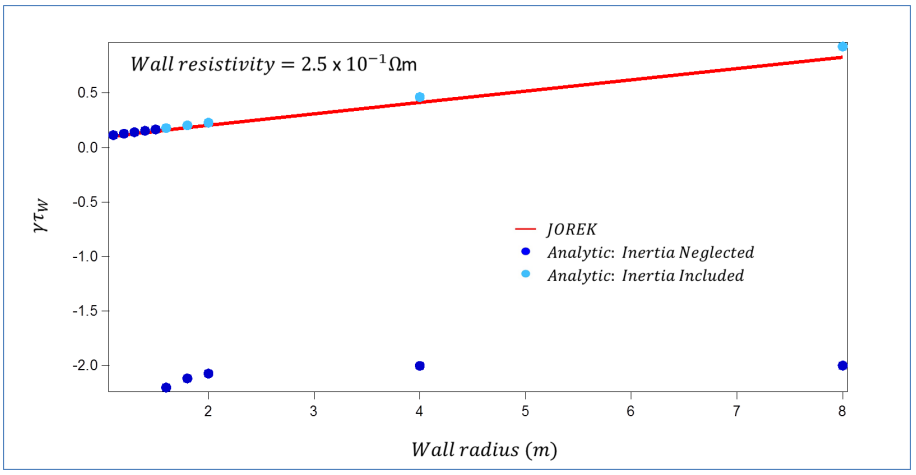

FIGURE 5.7: The inclusion of the inertia correction into the analytic growth rate equation is crucial for calculating the growth rate for larger wall radii.

Inclusion Of Plasma Inertia

When the resistive wall is located at $r_w > r_w^{ideal}$, the inertia contribution is necessary for predicting the correct growth rate. The right hand side of Equation 5.17 describes the inertia contribution to the mode growth rate. Neglecting the right hand side of Equation 5.17 will allow the growth rate of the RWM to be found when the inertia contribution is negligible.

The inertia is important for larger wall radii, where $r_w > r_w^{ideal}$. The stability of the resistive wall mode is determined by the wall eddy currents, not the plasma inertia; the inertia term can be neglected for close-fitting walls. However, the plasma inertia is important for ideal kink stability. The ideal kink is unstable when $r_w > r_w^{ideal}$, as described above in Section 5.3.1.

Without the inertia contribution, the dispersion relation is linear, and thus straightforward to solve for the growth rate of the mode. With the inclusion of the inertia term, the equation is cubic in γ. One solution will correspond to the RWM, and the two complex conjugate solutions correspond to the plasma mode. The three roots of the cubic Equation 5.17 can be found numerically. The initial guess for a solution is provided by solving Equation 5.17 with the inertia contribution set to zero. Then, an iteration with this value of γ as an initial guess is used to find the first root of the equation. Once the first root is known, Equation 5.17 can be reduced to a quadratic and solved directly for the remaining roots.

Figure 5.7 shows the results of including the inertia term for a range of wall radii. For wall radii such that $r_w < r_w^{ideal}$, inertia is not a significant contribution to the calculation of the growth rate of the mode. As shown by the dark blue markers, the JOREK growth

rate and the analytic calculation excluding the inertia term agree well. For larger wall radii, the dark blue markers showing the analytic growth rate without inertia included disagree substantially with the JOREK results. The inclusion of inertia resolves the discrepancy.

5.5 Summary Of Results

In this chapter, the implementation of the resistive wall in JOREK was discussed. The inclusion of the resistive wall is achieved by coupling JOREK to STARWALL. By using a linear model for a RWM, the growth rates found in JOREK simulations could be compared against calculated rates. This benchmark was successful. JOREK agreed with the linear model as to the wall radius at which an ideal wall would stabilise the ideal kink. There was also good agreement when the wall was resistive: though when the wall resistivity is low, some disagreement was found which is as yet fully unaccounted for. This benchmark supports the work described in [115].

Chapter 6

ITER simulations with JOREK and realistic wall

6.1 ITER Equilibrium

The inclusion of the resistive wall is useful while investigating the non-linear MHD physics in ITER advanced scenarios. The key features that need to be included in the equilibrium are the reversed safety factor profile and a sufficiently high β_N (above the no-wall limit). The plasma current should be around 9MA, and β_N projected to be ~ 2.9. Previous simulations of the advanced scenarios for ITER can be found in [119, 120].

The walls are modelled as thin shells. The first is an approximation to the ITER first wall, whilst the second is closer-fitting than the ITER first wall. The two walls used are shown in Figure 6.1. A no wall situation can be simulated by setting the wall resistivity very high ($\sim 10^9$) - the JOREK default without STARWALL coupling is an ideal wall at the plasma separatrix. The following simulations are carried out with the only toroidal mode number as n=1. The STARWALL matrix is generated for a particular set of mode numbers; changing the mode numbers requires a new STARWALL matrix.

6.1.1 Reducing The Edge Current

The initial equilibrium was set up with a reversed shear safety factor profile, with a minimum safety factor value of 1.5, a current of ~ 9 MA and $\beta_N = 2.2$. When the time stepping was implemented with the ITER-like wall, the eigenfunction of the unstable mode, shown in Figure 6.2, is highly localised at the edge of the plasma. In contrast, the RWM is a global mode and the displacement is expected to be across the whole plasma.

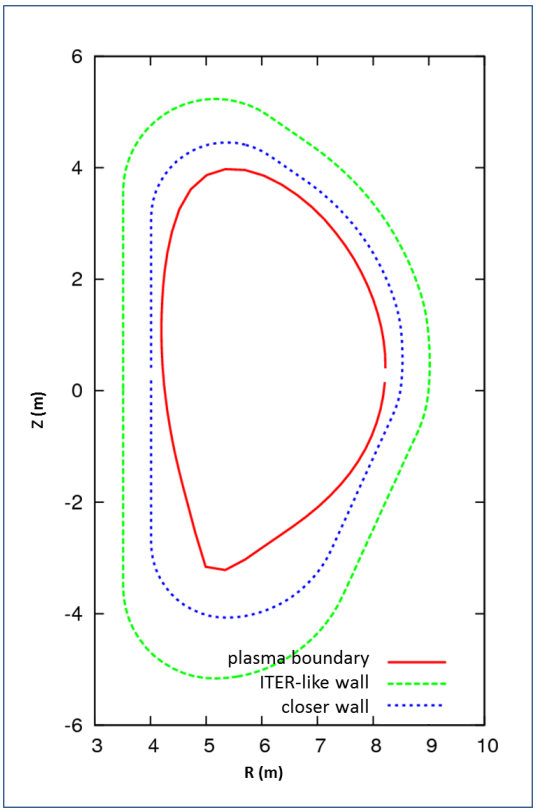

FIGURE 6.1: Location of the ITER-like wall in STARWALL (*courtesy of M. Hölzl*).

When the wall is moved closer to the plasma (the second wall in Figure 6.1), the edge mode has the same amplitude- the localisation of the displacement does not extend far enough outside the plasma to be affected by the resistive wall. It is difficult to move the wall even closer to the plasma, since the wall would interfere with the gridding process in JOREK.

Since the location of the wall does not affect the unstable edge mode, the stability and structure of the mode can be affected by altering its drive. The drive for the edge mode is the edge current. The current profile across the plasma is shown in Figure 6.4a). The current density is prescribed by two variables: the radial pressure gradient $\mathrm{p}'(\psi)$ and the $\mathrm{FF}'(\psi)$ profile, where $F(\psi) = RB_\phi$. The FF' profile is a direct JOREK input, however the radial pressure gradient cannot be manually set, and must be manipulated via the temperature and density input profiles. Altering the FF' profile is ineffective in reducing the edge current- the FF' profile is shown in Figure 6.3 in blue. This is because here β_θ is close to unity.

The temperature pedestal at the edge is changed instead. This will then change the p' at the edge, and thus the current density at that location. If the pedestal is sharpened,

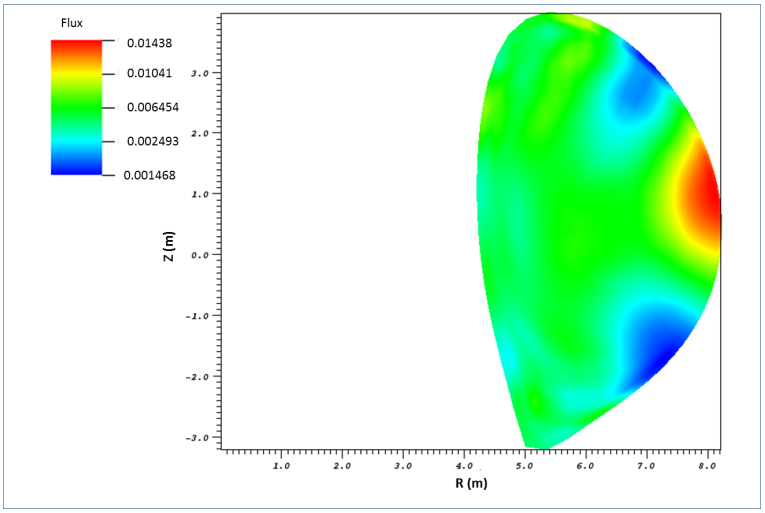

FIGURE 6.2: The $n = 1$ flux displacement for the first simulations, with $\beta_N = 2.2$. This unstable mode is located at the edge of the plasma. The RWM is, however, a global mode.

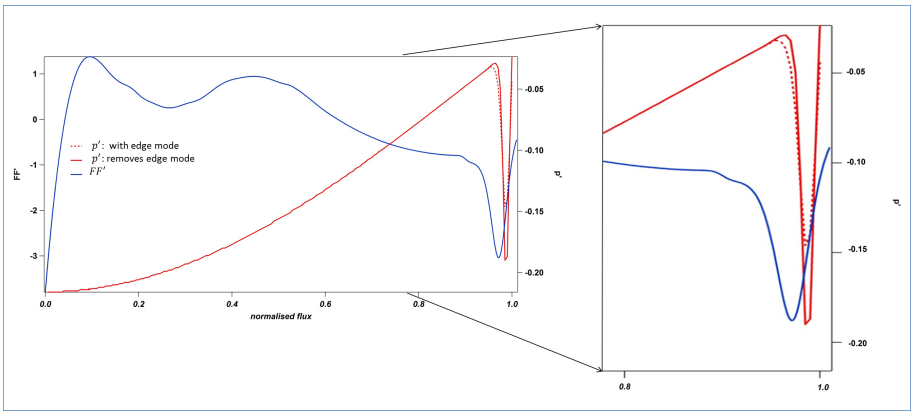

FIGURE 6.3: FF′ and p′ profiles for the first simulations. Changing the p′ profile at edge is necessary to alter the mode structure at that location.

then the p′ profile is deeper and the edge current is reduced. The remainder of the profile is unchanged. Figure 6.4A shows the difference between the two current profiles.

It can be noted in Figure 6.4B that the current profile is hollow. This is necessary to form the reversed shear safety factor profile, and is a key feature of advanced tokamak scenarios.

With the edge current reduced, the previous edge mode is stabilised and a global mode can be found. However, the β_N in this simulation is low, at $\beta_N = 2.2$. The β_N can be raised by scaling the magnetic field. This also results in translating the safety factor profile, as shown in Figure 6.5. It is crucial to keep the minimum safety factor greater than 1, to avoid MHD instabilities at the $q = 1$ rational surface. Scaling the toroidal

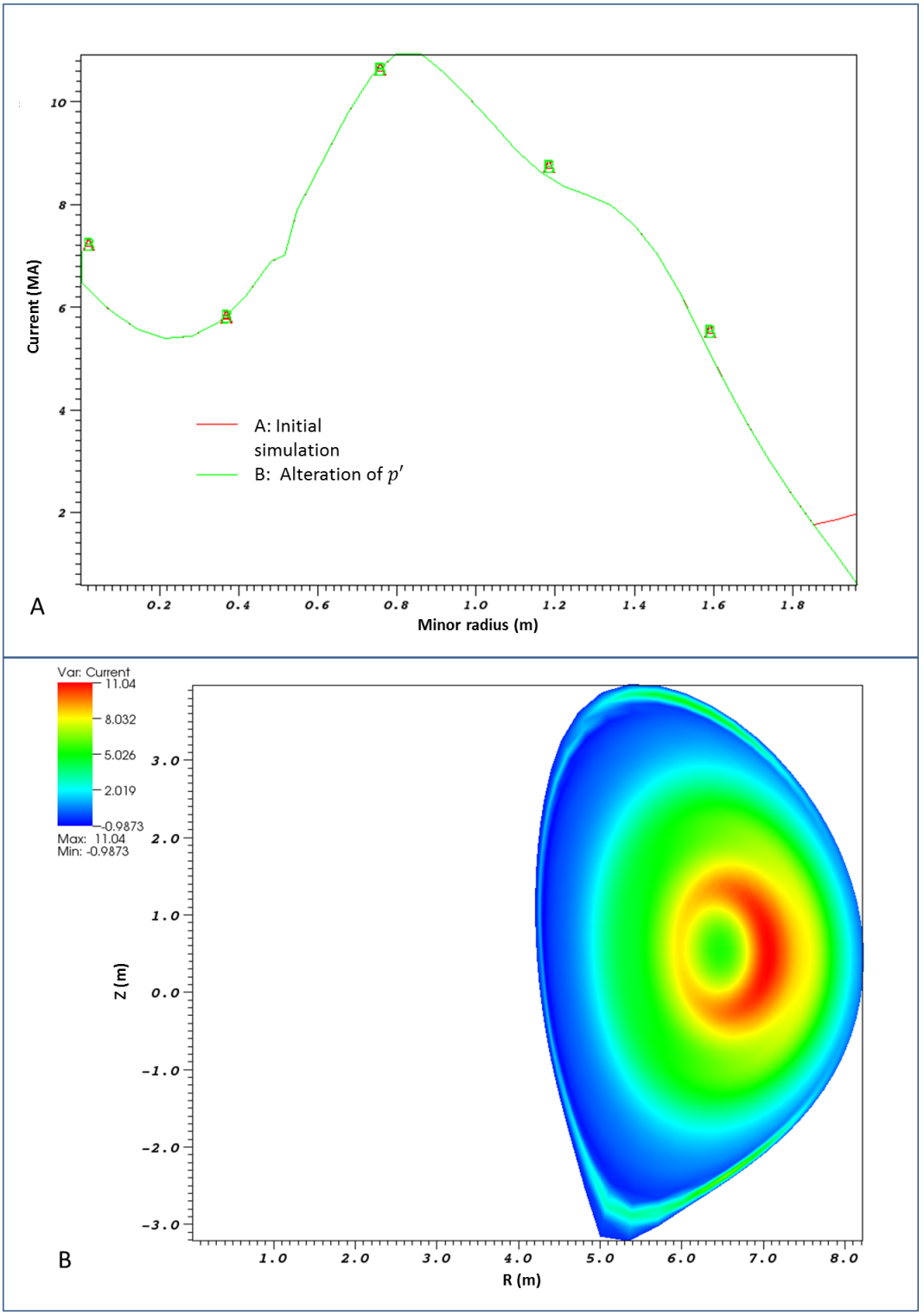

FIGURE 6.4: Figures showing the current profiles in the simulations. a) The reduction in edge current is shown in this figure. This is sufficient to stabilise the edge mode manifesting in the simulations; and b)the poloidal cross section shows the hollow current profile necessary for a reversed shear q profile.

magnetic field through the parameter $F_0 = RB_\phi$ changes β_N to $\beta_N = 2.6$. This is still not as high as many advanced scenarios, but substantially closer to them.

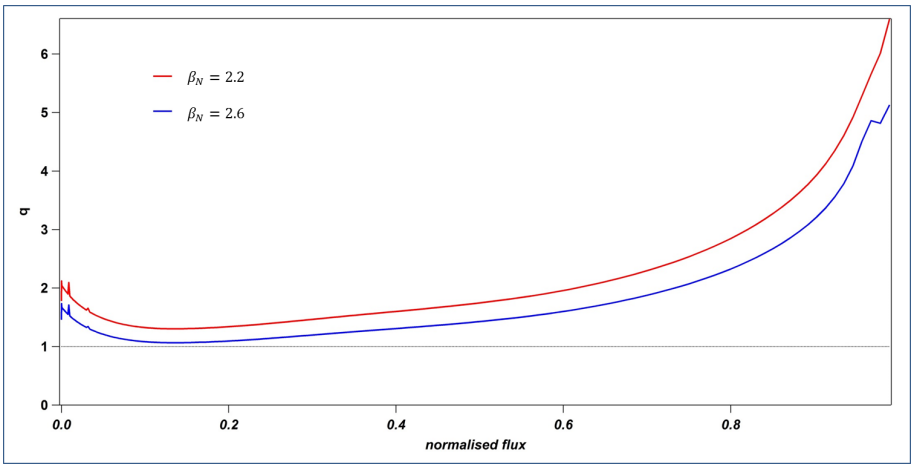

FIGURE 6.5: Scaling the magnetic field increases β_N to 2.6, but also translates the safety factor profile. The poloidal β remains constant when the q profile is changed - it is the toroidal β which is increased.

6.2 Features Of The Unstable Mode

After establishing an equilibrium with suitable parameters, the equilibrium can be evolved in time. However, after a certain number of time steps, a numerical instability prevents further evolution. Instead of entering a linear growth phase after an initial period of energy oscillation, the energy contained by the n=1 perturbation is subject to a numerical instability, which grows until it dominates the evolution. A discontinuity is seen in the time evolution of the n=1 energy and no further time steps are possible - JOREK is unable to converge on the next time step. This numerical instability is shown in Figure 6.6, where the $n = 1$ component of the kinetic energy has been plotted.

JOREK calculates the magnetic and kinetic energies as a function of time, for each Fourier harmonic. The energy can be used as an indication of the instability of the mode: an exponential growth in the energy corresponds to a constant growth of the mode. This growth rate can be calculated from the slope of the logarithm of the energy. At time steps t_1, t_2 with energies E_1, E_2 respectively, the growth rate (in JOREK units) is found by $\gamma_{JOREK} = (\ln(E_2) - \ln(E_1))/(t_2 - t_1)$.

The energy is calculated as two components: magnetic and kinetic energies. These are calculated respectively from the poloidal magnetic field B_θ, and the product of the density ρ with the poloidal velocity v_θ. B_θ is calculated from the poloidal magnetic flux function, and v_θ from the stream function u. The kinetic energy is the energy used

in this thesis: to calculate the kinetic energy, JOREK integrates ρv_θ^2 over the poloidal plane. Note that the toroidal field and the parallel velocity are not included in the calculations.

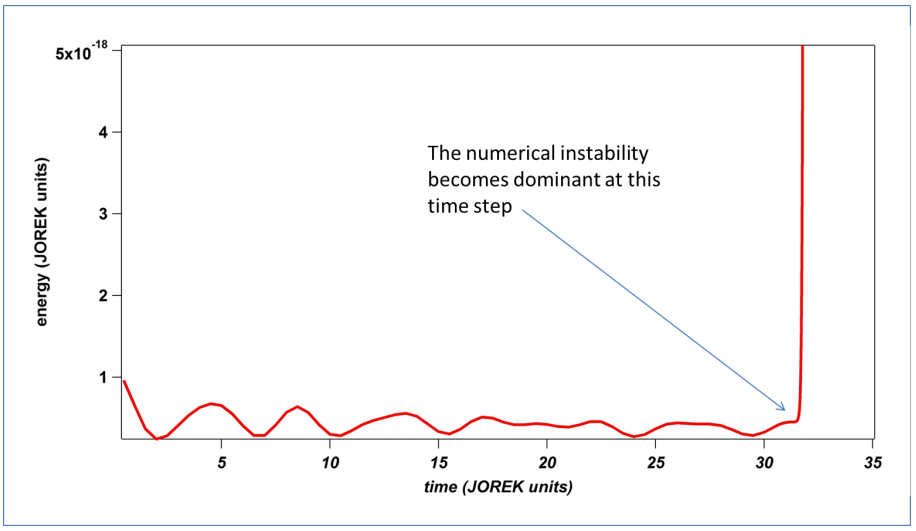

FIGURE 6.6: This simulation, with $\beta_N = 2.6$ and the ITER-like wall boundary condition, is prevented by a numerical instability from further time stepping.

In order to remove the numerical instability, the plasma resistivity and viscosity can be altered. By allowing both the plasma resistivity and viscosity to have profiles across the plasma instead of being fixed, the instability can be avoided. Without dissipation in the plasma, small scale structures which may develop cannot be resolved by the code. Dissipation will limit how fine these structures become. This allows further evolution, through a linear phase to saturation of the mode. The mode found is a global mode, with displacement across the whole poloidal cross section.

Comparison Of Mode Features For Different Boundary Conditions

Figure 6.7 shows the mode in the saturation phase, for $\beta_N = 2.6$ and plasma resistivity $\eta_p = 2.6 \times 10^{-6}$. This phase of the simulation is only accessible because JOREK is a non-linear code. The plots show the $n = 1$ flux perturbation to the equilibrium plasma in the poloidal cross section. The three plots A, B, and C show the mode with an ITER-like wall (with the corresponding real value of the ITER wall resistivity), the second, more closely-fitting, wall (of the same resistivity as the ITER-like wall), and an ideal wall at the plasma separatrix. An ideal wall on the plasma separatrix is the default JOREK boundary condition without the free boundary condition for STARWALL coupling. The final plot shows the eigenfunction of the flux perturbation for each plot. Comparing plots A and B clearly shows that moving the wall closer to the plasma will partially stabilise

the mode: the eigenfunction amplitude is smaller and the poloidal cross sections show that although the displacement has a similar structure, it has been reduced by the closer-fitting wall. Comparison with the mode when an ideal wall is placed at the ITER wall location in plot C of Figure 6.7 shows that the ideal wall stabilises the global mode, with perturbations localised at the vertical extremes of the plasma. These structures at the top and bottom of the plasma shown in Figure 6.7 for the ideal wall on the separatrix are also seen in the linear phase of growth for the simulation. The flux perturbation is again much smaller with this wall, as shown in the eigenfunction plot D. These plots show that firstly, the mode is external as the wall boundary condition affects its evolution; and secondly, that it is a global mode. This provides evidence that the mode we are simulating is indeed a RWM. In addition, in Figure 6.7, Plot D contains the $n = 1$ eigenfunction extracted from the poloidal flux perturbation plots A-C. The flux eigenfunction is taken at the location of the horizontal lines in the poloidal plots - the same location for each case. Plot D shows the relative magnitude and extent of the eigenfunctions - the perturbation is shown to extend over the poloidal plane for Plots A and B.), and the magnitude of the eigenfunction is smaller for the closer wall. The growth rate of the mode for different wall resistivities is discussed below in Section 6.2.2.

6.2.1 Plasma Resistivity Scan

The plasma resistivity is an important parameter to bear in mind whilst performing these large-scale MHD simulations, as can be seen in Section sec:featuresunstable where altering the plasma resistivity can resolve the numerical difficulties associated with inappropriate dissipation levels in the simulation. Although the RWM is not a resistive instability and its growth rate should not depend on the plasma resistivity, the use of plasma resistivity should be investigated in order to find how the simulation will be affected by it.

In order to investigate the mode stability, the plasma resistivity can be scanned while keeping $\beta_N = 2.6$ and using the ITER-like wall as the boundary condition. Previous simulations were carried out at a plasma resistivity $\eta_p = 2 \times 10^{-6}$ (this is given in JOREK-normalised units, which are given by $\eta_{SI} = \eta_{JOREK}\sqrt{\mu_0/\rho_0}$ where ρ_0 is the central density of the plasma). This results in a range of growth rates. The point where the plasma becomes stable can be seen in Figure 6.8. For plasma resistivities less than $\sim \eta_p = 1.4 \times 10^{-7}$, the plasma is stable, and the energy only oscillates instead of entering the linear growth phase. For plasma resistivities greater than this value, the plasma is unstable and the mode is able to grow. Figure 6.9 shows the growth rates for the simulations which vary plasma resistivity. It can be seen that for small plasma

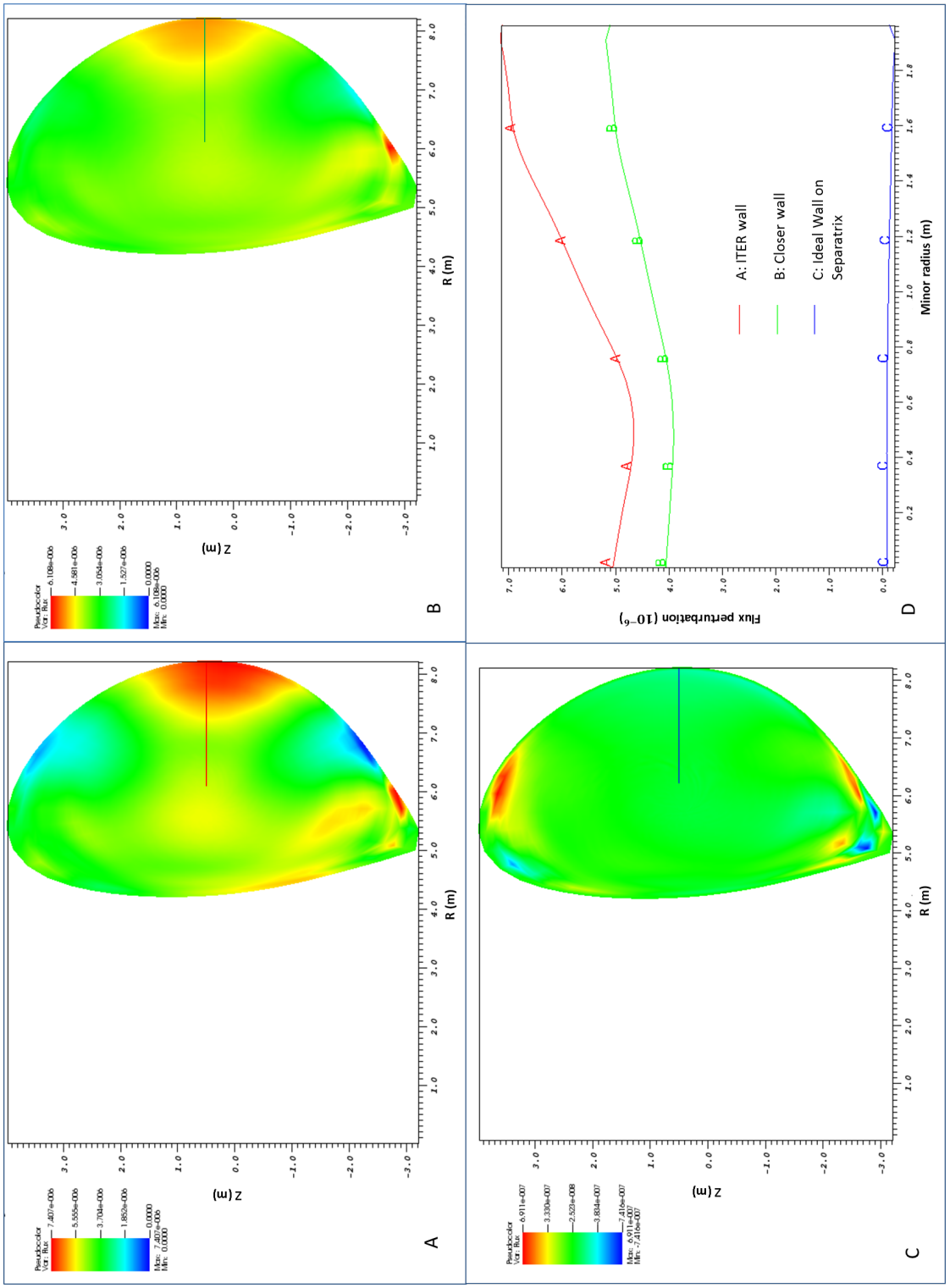

FIGURE 6.7: Comparison of saturated modes for $\beta_N = 2.6$ and different wall configurations A, B, and C: ITER-like wall, closely-fitting wall and ideal wall on the separatrix, respectively. Plots A and B have the same wall resistivity.The poloidal plots show the $n = 1$ flux perturbation. Moving the wall closer to the plasma partially stabilises the mode, whilst the ideal wall seems to stabilise global perturbations. Plot D shows the $n = 1$ flux eigenfunction plotted across the poloidal cross section (indicated by the horizontal lines in Plots A, B and C).

resistivities, the growth rate is negative: increasing the plasma resistivity increases the growth rate. For sufficiently large plasma resistivity, the growth rate becomes positive.

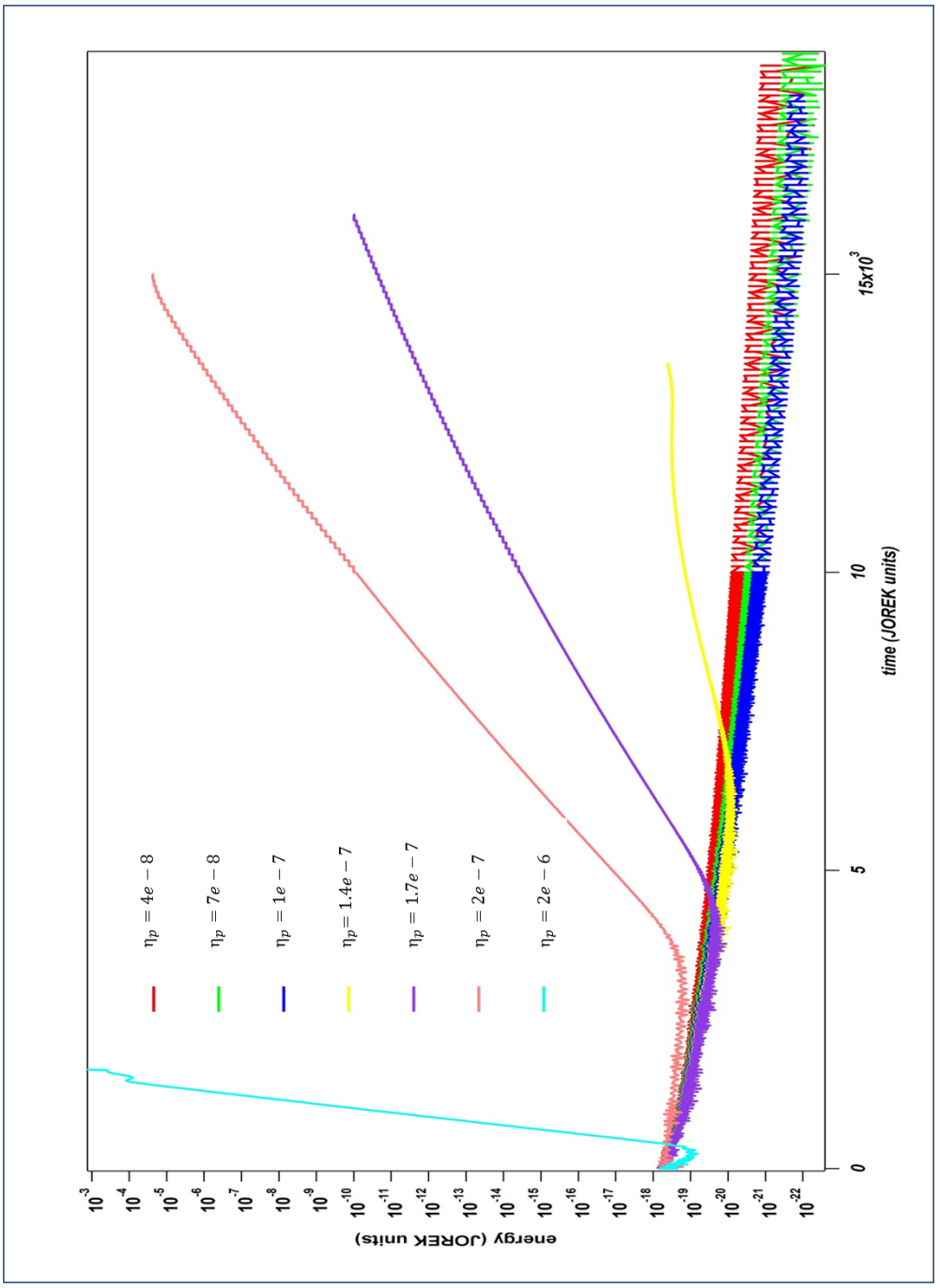

FIGURE 6.8: Energies for $n = 1$ (kinetic) for different plasma resistivities, with the ITER-like wall as a boundary condition and $\beta_N = 2.6$. Reducing the plasma resistivity reduces the mode drive and the results in a slower growth rate. The marginal stability point in plasma resistivity is an order of magnitude smaller than the value used in preceding simulations.

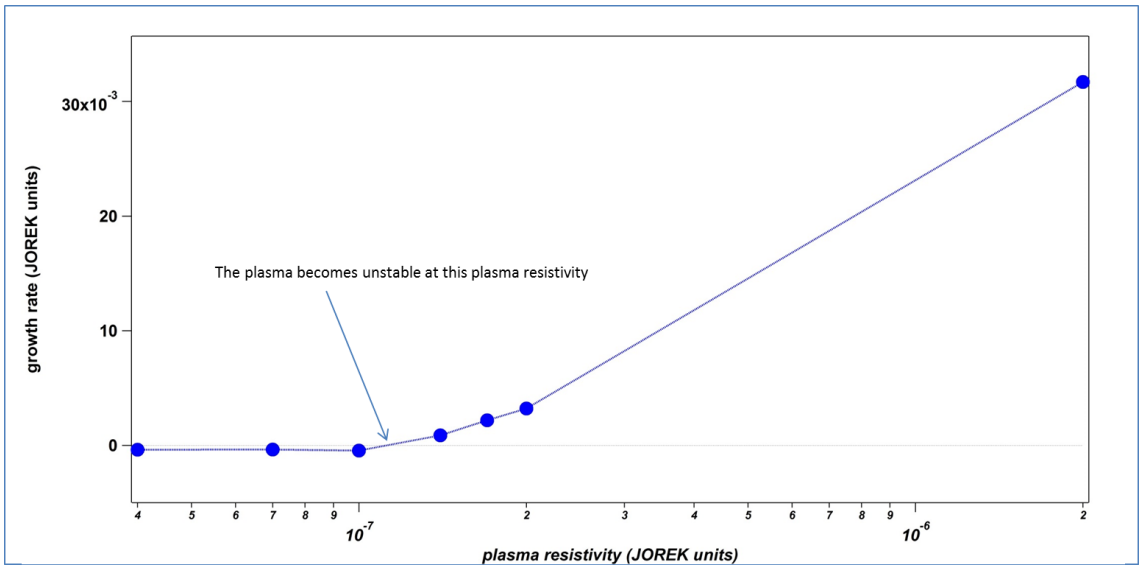

FIGURE 6.9: The plot shows the growth rates for the different values of plasma resistivity for $\beta_N = 2.6$, with the ITER-like wall included. The marginal stability point can be seen when the growth rates become positive.

6.2.2 Wall Resistivity Scan

With plasma resistivity fixed at $\eta_p = 1.4 \times 10^{-7}$ (in JOREK units) and $\beta_N = 2.6$, the effect of the wall on the growth of the mode can be seen in the kinetic $n = 1$ energies for each wall resistivity. The wall used is the ITER-like wall, as in Figure 6.1, and the wall resistivity is modified in the JOREK input file. The n=1 kinetic energy is used as a measure of the strength of the instability- and we can see a linear growth phase when the energy time trace grows linearly in time. A mode saturation phase is also seen when the n=1 energy saturates at some value (this is non-linear physics not captured by a linear code). We would expect the resistive wall mode to be increasingly stabilised by an increasingly ideal wall. In Figure 6.10, the ideal wall (at the ITER wall location) and a resistive wall of $\eta_w = 1.0 \times 10^{-4}$ (in JOREK units) are very similar, but the ideal wall is slightly more stabilising. In contrast, the mode with no wall surrounding it is more unstable.

An ideal wall placed on the separatrix would be expected to be the most stable situation. However, Figure 6.10 shows that it has the strongest growth (measured by the gradient of the logarithm of the kinetic energy of the n=1 perturbation). In the simulations comparing an ideal wall at the ITER wall location and an ideal wall on the separatrix, the magnetic flux perturbations are of a similar magnitude. However, the perturbation in potential for the ideal wall at the ITER wall location is an order of magnitude smaller than for an ideal wall on the separatrix. This suggests that the electromagnetic fluctuations may not be important compared to the electrostatic perturbations, and that the

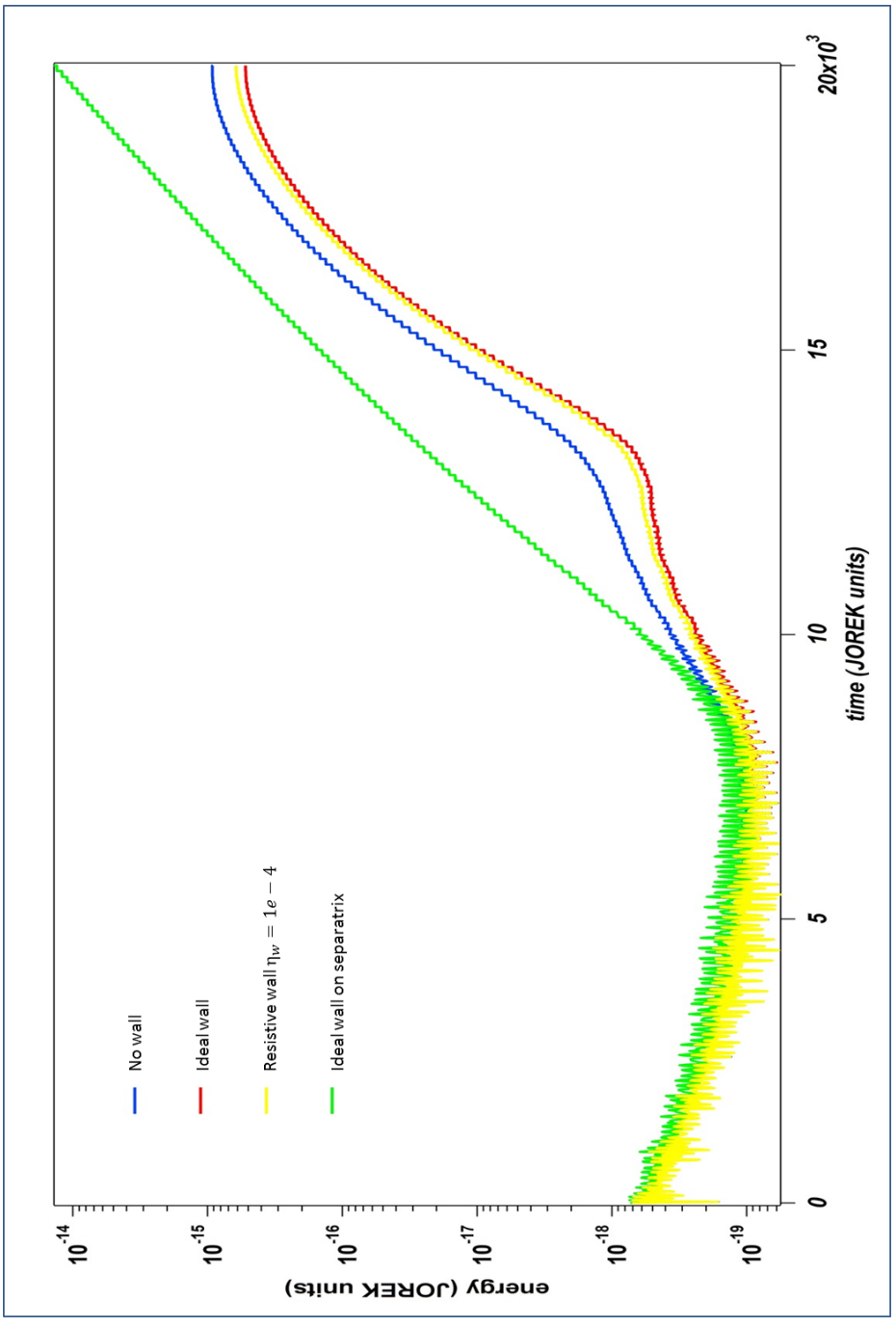

FIGURE 6.10: Scan of wall resistivities for $\eta_p = 1.4 \times 10^{-7}$ and $\beta_N = 2.6$, showing the kinetic energy for the n=1 perturbation. The resistive wall can stabilise the mode, compared to the simulation with no wall.

mode found when the ideal wall is placed on the separatrix is not essentially an MHD mode.

6.2.3 β_N Scan

The mode stability can be also be explored by changing β_N, and keeping the ITER-like wall as the boundary condition. Increasing β_N would be expected to increase the mode growth rate, since it corresponds to increasing the pressure. As β_N is not a direct JOREK input parameter, but calculated by JOREK after solving the plasma equilibrium, β_N must be indirectly manipulated by varying the toroidal magnetic field in the plasma. This changes the safety factor profile, which also affects the mode drive. The parameter $F_0 = RB_\phi$ in the JOREK input file is used to scale the toroidal magnetic field.

The first attempt to scan β_N was made only by scaling the magnetic field. This creates a family of safety factor profiles, with identical shapes but with the minimum safety factor value at different distances from $q = 1$. This alters the drive of the mode for each value of β_N found, which means the growth rates for each case were incomparable. Instead, it proved to be more useful to scale the magnetic field by changing F_0, and then to scale the magnitude of the plasma pressure profile. Changing these two parameters can together scale β_N, and retain a constant minimum safety factor profile. Although the safety factor profiles are not identical for each separate β_N case, they are similar, and vary over a small enough range, that the growth rates can be compared over a small range of β_N.

Figure 6.11 shows the JOREK growth rate for a range of β_N with the same boundary condition of the ITER-like wall. As expected, an increase in β_N corresponds to an increase in the growth rate of the mode. Thus, in tokamak operating regimes where β_N is ramped up in order to maximise power generation, the growth rate of the RWM would be increased also. For $\beta_N = 3.5$ (not shown in the figure), JOREK obtains a growth rate of $\gamma_J = 4.6$, which is 4 orders of magnitude higher than the growth rate for $\beta_N = 2.6$.

6.3 Adding Parallel Velocity Profile

JOREK is capable of modelling parallel (to magnetic field lines) velocity by changing the physics model. The additional equation to be solved is Equation 5.1.2.

A key difference to using the parallel velocity model is the initial simulation of the equilibrium. In previous simulations, the equilibrium is solved at time $t = 0$, and

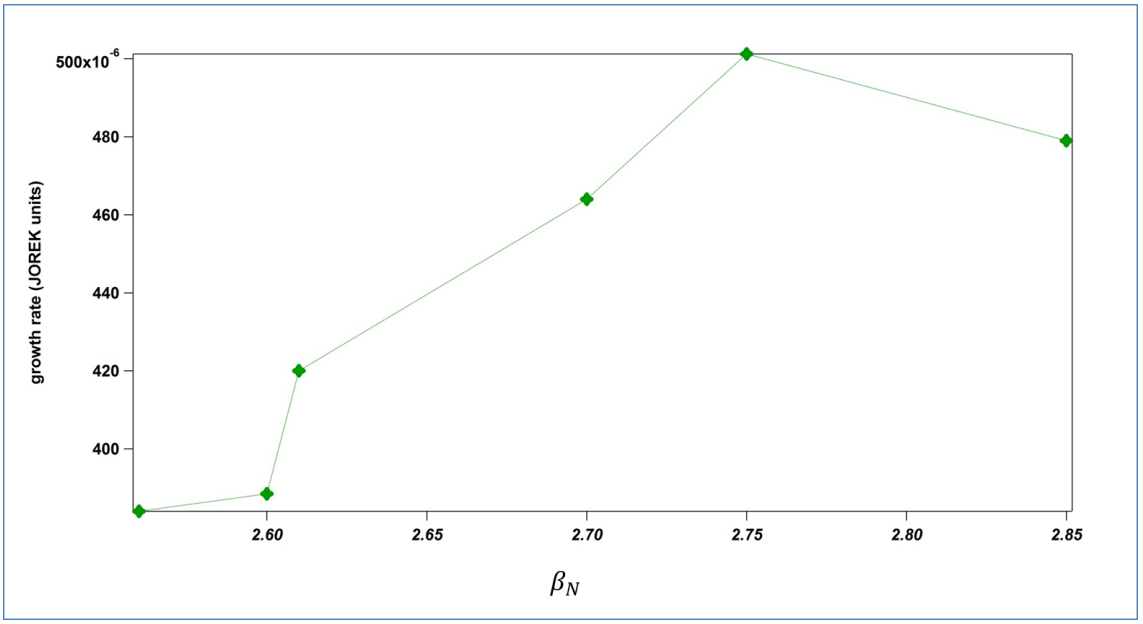

FIGURE 6.11: The scan over β_N with the ITER-like wall, and at the marginal plasma resistivity of 1.4×10^{-7}, is carried out by adjusting B_ϕ and the plasma pressure in order to keep the minimum safety factor constant but change β_N. As would be expected, increasing β_N increases the growth rate of the mode. A larger range in β_N is difficult to access without changing the minimum safety factor significantly, hence the growth rate of the highest β_N is lower than would be expected from the trend.

the time stepping with the relevant toroidal mode numbers is commenced immediately. When using the model with parallel velocity included, the equilibrium should be evolved in time, with only $n = 0$ included, until the energy of the $n = 0$ harmonic has become stable. The $n = 0$ energy will oscillate for a time, and incorrect results are found if the simulation equilibrium is not allowed to settle before adding the $n = 1$ perturbation.

6.3.1 Unspecified Velocity Profile

If no parallel rotation profile is specified, then JOREK will assume a profile with zero parallel velocity. However, this variable is still evolved by the code whilst time stepping. The input profiles of previous simulations which do not include parallel velocity can be used as input for this model, but JOREK will produce different results due to the extra field. In the first simulations using this physics model, a numerical instability prevented simulations progressing further than a few hundred JOREK timesteps. This was solved by changing the grid within JOREK, and then implementing regenerated STARWALL matrices.

For a plasma resistivity of $\eta_p = 1.4 \times 10^{-7}$ and $\beta_N = 2.6$, which we showed above to be the marginal stability point in plasma resistivity, with no parallel velocity profile

specified, JOREK now finds an instability that initially grows but then shrinks away. This suggests that in this model where the parallel flow is evolved, the plasma resistivity is not sufficiently large enough to observe the mode grow and saturate. The parallel velocity perturbation plot is shown in Figure 6.12.

Increasing the plasma resistivity should increase the drive of the instability. If the plasma resistivity is increased to $\eta_p = 2.0 \times 10^{-7}$, then the instability is again found. as shown in Figure 6.13. After the initial simulation period, when only the $n = 0$ equilibrium component is included to allow the equilibrium with parallel flow to establish, the instability begins to grow. Instead of dying away as in Figure 6.12, the instability has sufficient drive to begin to grow exponentially. Unfortunately, a numerical instability at the end of the simulation prevents the simulation proceeding sufficiently far for the saturation of the mode to be found. When a rotation profile is added, the numerical instability ends the simulation in even fewer timesteps. Further work is required to remove this numerical problem, and complete a simulation through to saturation of the mode.

6.4 Summary Of Results

JOREK is used to simulate advanced tokamak plasmas in an ITER geometry. Coupled to STARWALL, the wall is modelled as the ITER first wall with the corresponding resistivity. A plasma equilibrium is constructed which is unstable to the Resistive Wall Mode. The effects of changing both the plasma resistivity and the wall resistivity are shown. The β_N of the plasma can also be varied by scanning the toroidal magnetic field. Initial simulations with a physics model which includes parallel (to the magnetic field line) velocity are carried out, which show that the different physics model affects the mode stability boundaries. A slightly higher plasma resistivity is required to find an unstable mode, but numerical problems during the linear growth phase prevent the simulations entering the saturation phase.

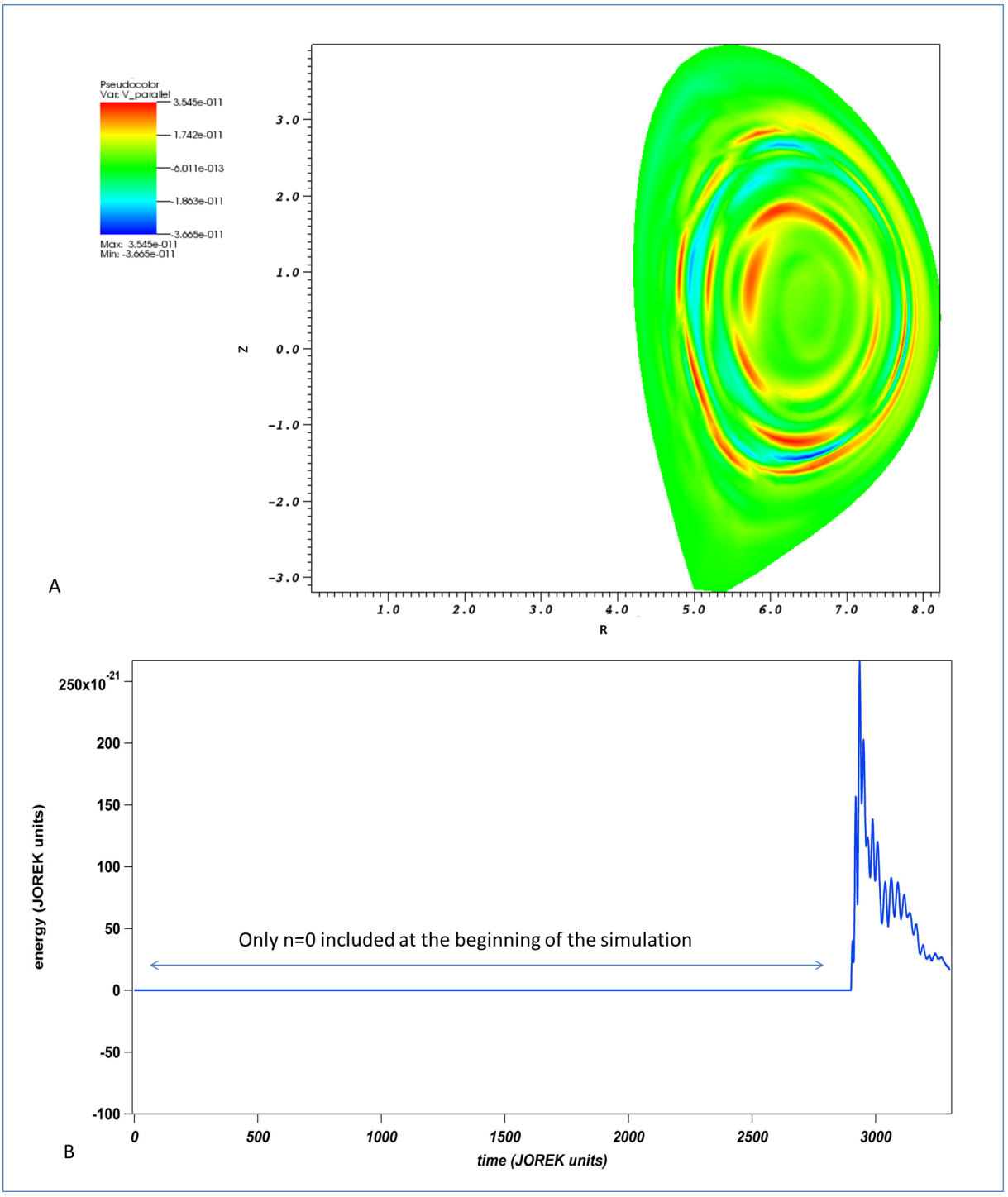

FIGURE 6.12: Plot A shows the parallel velocity perturbation for a JOREK simulation with $\eta_p = 1.4 \times 10^{-7}$ and no initial velocity profile chosen. For the previous physics model, this value of plasma resistivity was at marginal stability. With parallel velocity included, the mode is not unstable and so does not enter a linear growth phase. The energy plot in B shows that the $n = 1$ mode does not enter a linear growth phase, and in fact shrinks away.

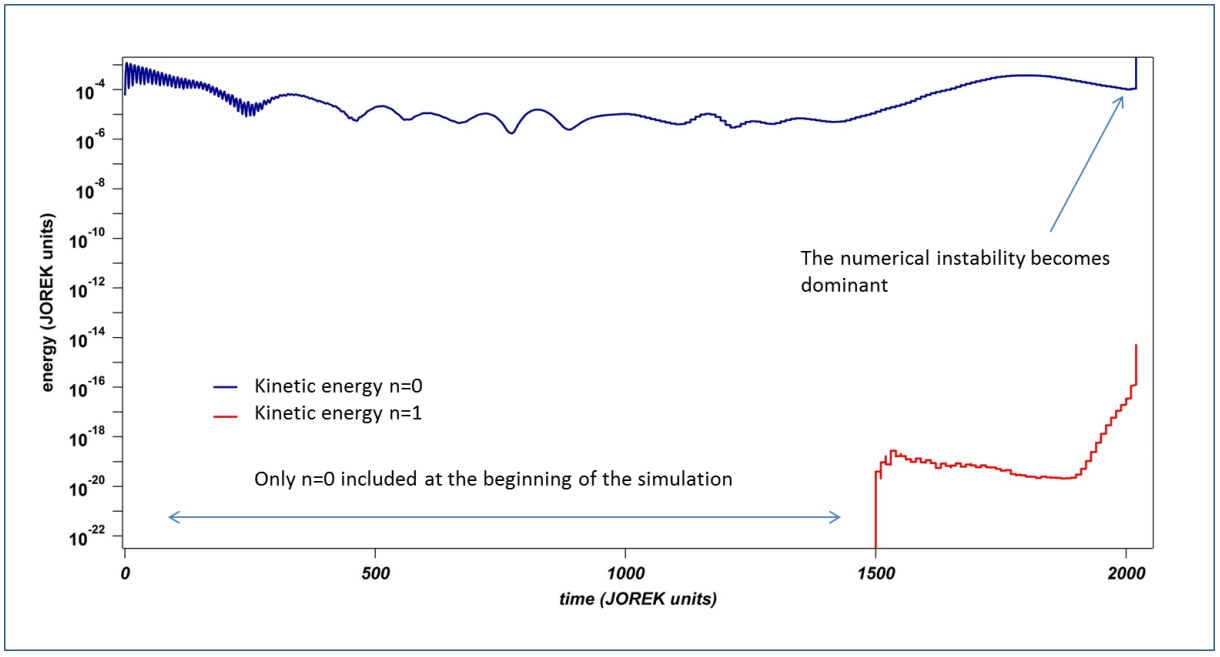

FIGURE 6.13: The figure shows both the $n = 0$ and $n = 1$ kinetic energy components of the simulation, which has $\eta_p = 2.0 \times 10^{-7}$ and $\beta_N = 2.6$. The simulation is run with $n = 0$ only until the equilibrium becomes stable, then the $n = 1$ perturbation is included. The instability grows, and begins to enter the linear phase at $t \sim 1900$. However, the numerical instability, seen most clearly in the $n = 0$ component, prevents the simulation progressing.

Chapter 7

Conclusions And Outlook

Conclusions

In order for nuclear fusion to become a viable power generation method, the development of cost-competitive and reliable reactors is necessary. A step towards this goal is the conception of advanced tokamak scenarios. These operating scenarios aim to optimise the non-inductive current, and achieve steady state tokamak operation.

However, the optimised profiles (such as current and density profiles) in advanced scenarios position the operating scenarios close to MHD stability boundaries; and it is expected that without mitigation, MHD modes may become unstable. This would result in plasma degradation, and possibly costly disruptions. In addition, the use of negative ion sources in the neutral beams (which is required to meet energy needs) will result in high energy beams, with less momemtum in the beam for a given power than current beams. This development in operating conditions from present to future tokamaks presents a challenge to the fusion community. Thus, a better understanding of the stability of modes whose stability is affected by the level of plasma rotation, such as the Resistive Wall Mode, will be needed in order to understand the results of future experiments, and to try to mitigate or stabilise the modes.

Non-linear effects are very important for studying MHD modes. The inclusion of non-linearity is necessary for modelling mode saturation, as well as the coupling of MHD modes. Non-linear modelling is also needed to understand the interaction of plasma rotation with the growth of MHD modes. In this thesis, non-linear modelling is carried out both analytically and with simulations.

In Chapters 3 and 4, the analytic model coupled two MHD instabilities: the Neoclassical Tearing Mode and the Resistive Wall Mode. A set of coupled non-linear equations was

derived by considering three regions in the system: the ideal plasma regions, the resistive wall, and the rational layer where the magnetic island is located. These equations were solved, firstly by finding a limiting analytic solution for small islands, and secondly numerically. The equations could also be integrated numerically in order to obtain mode growth rates, frequencies, and plasma rotation frequencies as a function of time.

Chapters 5 and 6 describe non-linear simulations using JOREK. The inclusion of the code STARWALL into JOREK allows for simulations of plasmas with resistive wall boundary conditions. Chapter 5 describes the benchmarking carried out against a linear RWM dispersion relation, which successfully shows the agreement between JOREK and the linear model. Chapter 6 shows JOREK simulations in an ITER geometry using a resistive wall which is based on the ITER first wall. An equilibrium is found which is unstable to the RWM, and initial simulations are carried out showing the features of the mode with respect to plasma resistivity, wall resistivity and β_N. Attempts to include a more complex physics model in JOREK, which incorporates plasma flow parallel to the magnetic field lines, are also briefly included. These simulations for a plasma with flow show that the plasma marginal stability is located at slightly different parameters when the physics model is changed.

Future Work

Substantial scope for future work can be found in the work presented in this thesis, both in the analytic modelling and JOREK simulations.

In the analytic modelling, it is possible to extend the model to include error field effects on the NTM. Error fields are small variations in the magnetic field which are unintended, but result from misaligned field coils. The misalignment could be caused by manufacturing or engineering issues. Error fields can be resonant with modes in the plasma, and are known to exacerbate mode instability. They are also responsible for exerting a drag on the plasma, slowing the plasma rotation. There are a number of theoretical works which study the link between RWMs and error fields: including that of Gimblett and Hastie detailed in Appendix B. In [35], it can be seen that the equivalent to Δ_W at the wall for the error field coil is $\Delta_{coil} = -imI/\psi_E$ where ψ_E is the helical flux at the coil location (and is a function of the plasma equilibrium), and I is the measure of the helical current responsible for the error field. The system would be solved for the amplitude and phase of ψ_E. Additionally, the relationship between the layer Δ_L and the error field coil Δ_E is identical to that between Δ_L and Δ_W. The implemetation of the coupling between rational layer and error field coil would be thus similar to that of the coupling between rational layer and resistive wall. It could be expected that the

magnitude of the error field affects the NTM island threshold width, and it may provide another explanation for the observation of triggerless NTMs.

The implementation of the JOREK-STARWALL coupling, and the ability to model 3D resistive walls in a realistic geometry, is a foundation for simulating not only RWMs but also other modes such as ELMs, and Vertical Displacement Events (discussed in [115]). In terms of modelling Resistive Wall Modes, the addition of the wall is important for understanding the interaction of resistive wall and rotating plasma. In particular, the simulations with ideal walls on the separatrix, which produced growth rates much higher than expected, should be investigated to understand the reasons why the simulations are not as would be expected.

Using JOREK with a physics model that includes parallel (i.e. along magnetic field lines) flow allows for exploring this interaction. Simulations of advanced tokamak plasmas (specifically for ITER scenarios) with plasma flow included, can assist with understanding the effects of the low rotation rate in these scenarios. Once the numerical instability is removed from the simulations, further work would include modelling the effects of varying the parallel rotation profile on the growth of the RWM; and conversely, the effect of the growth of the RWM on the parallel rotation profile.

Furthermore, it could be possible to investigate the analytic model explored in Chapter 3 and Chapter 4. This could be achieved by seeding a magnetic island at a rational surface using the $FF^{'}$ input profile. A spike in this profile would result in an island forming in the plasma, which would remain unstable to the RWM also. The effect of plasma rotation could then be examined in JOREK with the resistive wall included.

Appendix A

RWM Dispersion Relation Using Variational Principle

The following derivation is given in Haney and Freidberg [30]. Using the Energy Principle, Haney and Freidberg [30] derived a dispersion relation for the RWM, requiring only knowledge of the behaviour of the system with the ideal wall.

The stability of a plasma is calculated by using the Energy Principle. A plasma is stable if, for all plasma displacements ξ, the plasma energy $\partial W > 0$. The plasma is unstable if there exists a physically allowed displacement such that $\partial W < 0$.

Ideal Wall At Infinity

Suppose an ideal wall is located at infinity: then the plasma energy can be expressed as

$$\partial W_\infty = \partial W_F + \partial W_V^\infty \tag{A.1}$$

where ∂W_F is the fluid energy integrated over the volume of the plasma, and ∂W_V^∞ is the vacuum energy integrated over the vacuum region surrounding the plasma.

$$\partial W_F = \tfrac{1}{2}\int_{V_p}\left(\tfrac{|\partial\mathbf{B}|^2}{\mu_0} - \xi\cdot(\mathbf{J}\times\partial\mathbf{B}) + \gamma p|\nabla\cdot\xi|^2 + (\xi\cdot\nabla p)\nabla\cdot\xi\right)dV \tag{A.2}$$

$$\partial W_V^\infty = \tfrac{1}{2}\int_V \tfrac{\partial\mathbf{B}_\infty}{\mu_0}dV \tag{A.3}$$

It has been assumed that no surface currents flow in the plasma boundary so there is no contribution from the surface energy. ∂W_F can be found easily given a trial function ξ. To deal with ∂W_V, the vacuum magnetic field is expressed as a vector potential:

$\nabla \times \partial\mathbf{A}_\infty$, with $\partial\mathbf{A}_\infty$ satisfying $\nabla \times \nabla \times \partial\mathbf{A}_\infty = 0$. The boundary conditions used are $\partial\mathbf{A}_\infty|_\infty = 0$ and, if $\mathbf{e_n}$ is the outward facing unit normal to the surface of the plasma, S_p, $\mathbf{e_n} \times \partial\mathbf{A}_\infty|_{S_p} = -(\mathbf{e_n} \cdot \xi)\mathbf{B}|_{S_p}$. This is the linearised jump condition for the electric field across the plasma surface. (The pressure jump condition is considered to be 'as good as' satisfied as part of the variational method.)

Equation A.3 can be rewritten as

$$\partial W_V^\infty = \frac{1}{2\mu_0}\int_{S_p} (\mathbf{e_n} \times \partial\mathbf{A}_\infty) \cdot \mathbf{e_n} \times (\mathbf{e_n} \times \nabla \times \partial\mathbf{A}_\infty) dS \tag{A.4}$$

Assume that the system is unstable with the wall at infinity: that it, $\partial W_\infty < 0$.

Ideal Wall At Finite Radius

Now consider a closed, ideal wall of arbitrary shape, a finite distance from the plasma, where the surface of the wall is S_b. The plasma displacement ξ (i.e. the trial function in the variational method) is identical to the displacement with a wall at infinity.

The potential energy can now be written $\partial W_b = \partial W_F + \partial W_V^b$, where ∂W_F has the same value as when the wall is at infinity. Assume that the potential energy $\partial W_b > 0$, such that the system is stabilised by the ideal wall at a finite distance from the plasma. In addition,

$$\partial W_V^b = \frac{1}{2\mu_0}\int_{S_p} (\mathbf{e_n} \times \partial\mathbf{A}_b) \cdot \mathbf{e_n} \times (\mathbf{e_n} \times \nabla \times \partial\mathbf{A}_b) dS \tag{A.5}$$

such that $\nabla \times \nabla \times \partial\mathbf{A}_b = 0$ with the analogous boundary conditions $\mathbf{e_n} \times \partial\mathbf{A}_\infty|_{S_b} = 0$, and $\mathbf{e_n} \times \partial\mathbf{A}_\infty|_{S_p} = -(\mathbf{e_n} \cdot \xi)\mathbf{B}|_{S_p}$. The boundary conditions are slightly different due to the presence of the ideal wall at finite radius.

Assume that the system is stable with the ideal wall at this finite radius: that is, $\partial W_b > 0$.

Resistive Wall At Finite Radius

The ideal wall at S_b is replaced by a resistive wall of conductivity σ and thickness d,whilst keeping the same trial function ξ. Now $\partial W_b = \partial W_F + \partial W_V^b$, where ∂W_F has the same value as above. The analysis hinges on the assumptions: firstly that the growth rate of the RWM is comparable to the characteristic wall diffusion time $\tau_w = \mu_0\sigma d\bar{b}$, where $\bar{b}$ is the average radius of the vacuum chamber. Thus

$$\gamma << \gamma_{MHD} \tag{A.6}$$

where $\gamma_{MHD} = -\partial W_\infty / K$ is the characteristic ideal MHD growth rate with the wall at infinity. Additionally, the wall is assumed to be 'thin': $d << \bar{b}$. These assumptions imply that plasma inertia effects are negligible on relevant timescales. Thus the linearised ideal MHD force operator as a function of the plasma displacement is $\mathbf{F}(\xi) = 0$. This can be used to write a Lagrangian for the plasma surrounded by a resistive wall:

$$L = \int_{V_p} \xi \cdot \mathbf{F}(\xi) dV = 0 \tag{A.7}$$

or

$$L = \partial W_F + \frac{1}{2} \int_{S_p} (\mathbf{e_n} \cdot \xi) \left(\frac{\hat{\mathbf{B}} \cdot \partial \hat{\mathbf{B}}}{\mu_0} \right) dS \tag{A.8}$$

By calculating jump conditions over the resistive wall, L can be written

$$\partial W_F + \partial W_V^i + \partial W_V^o + \frac{\sigma \gamma d}{2} \int_{S_b} |\mathbf{e_n} \times \partial \hat{A}|^2 dS \tag{A.9}$$

where $\hat{A}$ refers to vacuum quantities, and the subscripts i, o refer to the inner (between wall and plasma) and outer (beyond wall) vacuum regions. In the limit of marginal stability, $\gamma \to 0$, the Lagrangian reduces the ideal MHD potential energy, with a wall at infinity ∂W_∞.

Using properties of the vacuum solutions, and the variational variable c, L is expressed as [30]

$$L = \partial W_\infty + c^2 (\partial W_b - \partial W_\infty) + \frac{\sigma \gamma d (1-c)^2}{2} \int_{S_p} |\mathbf{e_n} \times \hat{\mathbf{A}}_\infty|^2 dS \tag{A.10}$$

This is quadratic in c, which can be eliminated by solving $\partial L / \partial c = 0$. Setting $L = 0$, the dispersion relation

$$\gamma \tau_w = -\frac{\partial W_\infty}{\partial W_b} \tag{A.11}$$

can be found, where $\tau_w = \mu_0 \sigma \hat{b} d$, such that $\hat{b}$ is the average radius of the vacuum chamber.

Equation A.11 shows that, for a system unstable with the wall at infinity, but stable with an ideal wall sufficiently close to the plasma, is always unstable to a slowly growing mode (RWM) if the ideal wall is replaced by a resistive wall.

Appendix B

Gimblett And Hastie RWM Model

The analytical model in [35, 55] is similar to that used in Chapters 3, 4. The technique of linking resistive, rational layers together through ideal MHD regions is used extensively in the literature (as in [121], for example).

In this case, the use of the rational layer, and the growth of a magnetic island there, is necessary to allow the inclusion of the torque balance relation. Analogously to the model developed in this thesis, the wall response is modelled as the thin wall approximation [100]. However, in the Gimblett and Hastie model, the layer response differs that used in this thesis. In this thesis, the growth of the magnetic island is determined by the non-linear NTM physics, in [55] the layer response is visco-resistive [122].

$$\Delta^{'} = (p\tau_L)^{\frac{5}{4}} \tag{B.1}$$

where τ_L is the characteristic resistive layer time [77]. This response can be compared to the layer response obtained in Chapter 3

$$4\dot{w} = Re[\Delta_L] + \frac{\hat{\beta}}{w}\left(1 - \frac{w_c^2}{w^2}\right) \tag{B.2}$$

$$2w(\omega - \Omega_L) + Im[\Delta_L] = 0 \tag{B.3}$$

which describes the NTM evolution.

Gimblett and Hastie also note that the inclusion of torque balance must a non-linear process because the electromagnetic torque is quadratic to the magnetic perturbation

$$T_{em} \propto (\partial B_r)^2 Im[\Delta\prime] \tag{B.4}$$

which can also be seen in the torque balance equation obtained in Chapter 3

$$(\Omega_0 - f\Omega_L) = Aw^4 Im[\Delta_L] \tag{B.5}$$

since the island width w is quadratic in the perturbation.

The final torque balance equation obtained by Gimblett and Hastie is

$$\Omega_0 - \Omega = C\omega \tag{B.6}$$

where Ω is the plasma rotation frequency, Ω_0 the rotation frequency of the unperturbed plasma equilibrium, and ω the mode frequency. The constant C contains the balance between electromagnetic and viscous forces on the plasma, and represents the amplitude of the mode. The apparent simplicity of Equation B.6 is deceptive: the model has in fact as multi-valued structure. This structure has been found in other problems [123, 124].

Figure B.1 shows the RWM trajectories in parameter space. The stability window in Ω is shown.

For an initial plasma rotation $\Omega < \Omega_1$, the RWM is unstable. The RWM grows (accompanied by a growing magnetic island) and the plasma rotation decreases asymptotically to zero. For $\Omega_0 > \Omega_2$, the RWM is again unstable. The RWM grows, and the plasma rotation decreases slowly until it reaches Ω_2. At this point, the growth stops, but a large magnetic island remains. If $\Omega_1 < \Omega < \Omega_2$, then the RWM is stable, and the system remains in the stability window.

Finally, the last option is shown more clearly in Figure B.2 [35]. If the initial Ω is very large, such that the 'knee' of the curve occurs above the stability window, then the RWM is initially unstable. The RWM grows, as does the magnetic island, whilst the rotation decreases. It has been previously established [57, 125] that the system does not follow the trajectory backwards, but is forced to drop down to rejoin the trajectory curve at the lower rotation value. We see a sudden flip to a lower rotation value when Ω reaches a critical value, accompanied by more rapid RWM growth.

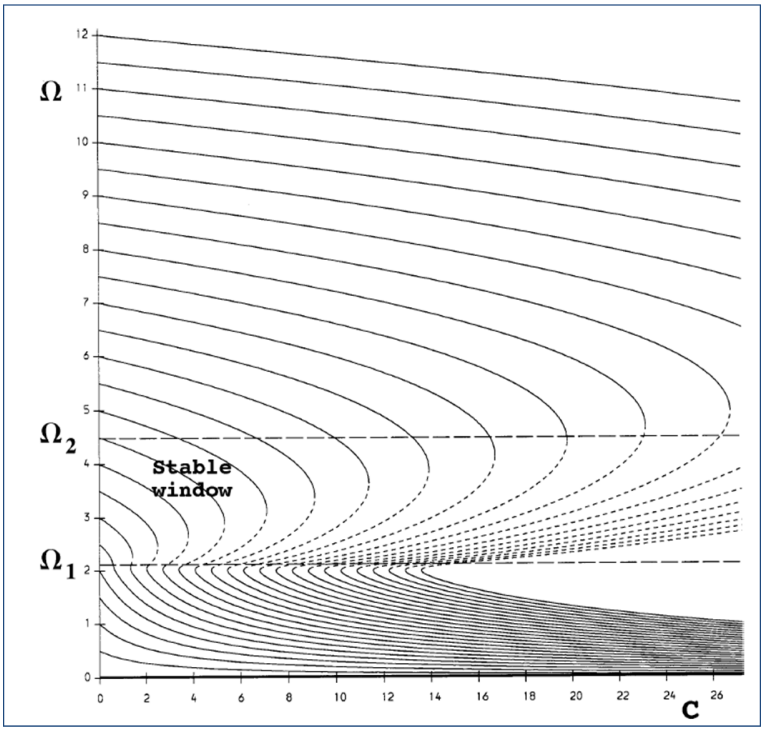

FIGURE B.1: RWM trajectories in parameter space [55]. The graph shows the multi-valued structure of the model system. The stable window for the RWM is indicated.

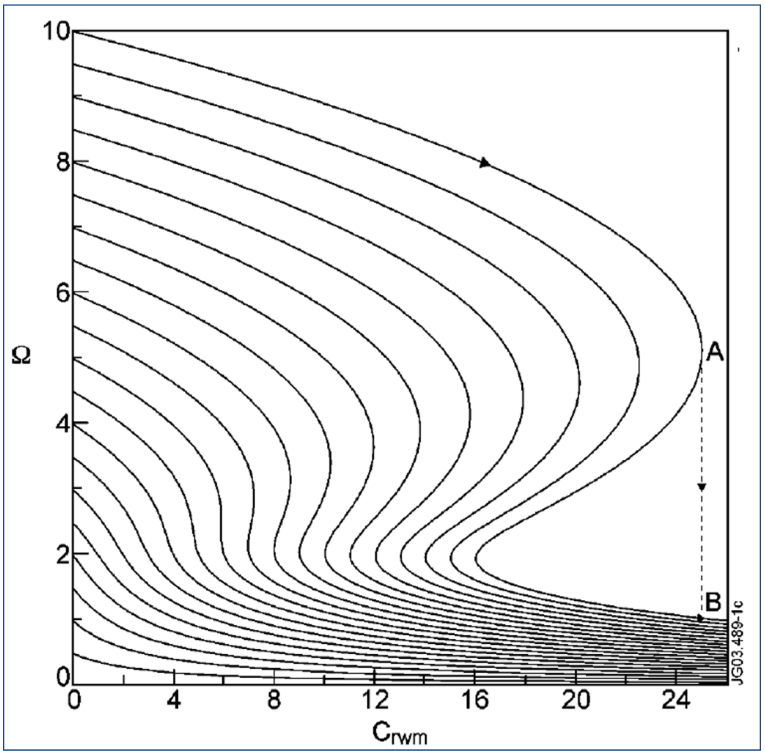

FIGURE B.2: S curves for the RWM are shown [35]. The characteristic behaviour of the rotation drop from A to B is illustrated.

The s-curve behaviour is not seen in the model developed in this thesis. As discussed in Chapter 4, the resistive wall mode is not sensitive to the plasma rotation - the electromagnetic torque is very large at the rational surface.

Bibliography

[1] International Energy Agency. World Energy Outlook. 2013. URL http://www.worldenergyoutlook.org/pressmedia/recentpresentations/LondonNovember12.pdf.

[2] International Energy Agency. World Energy Outlook. 2012. URL http://www.iea.org/newsroomandevents/speeches/130326FutureEnergyTrendsWEO2012NZrev.pdf.

[3] J. Wesson. *Tokamaks*. Clarendon Press, 3rd edition. ISBN 978-0198509226.

[4] J. D. Lawson. Some criteria for a power producing thermonuclear reactor. *Proceedings of the Physical Society. Section B*, 70(1):6, 1957.

[5] R. J. Bickerton and et al. *Nature Phys, Sci,*, 229:110, 1971.

[6] C.E. Kessel. Bootstrap current in a tokamak. *Nucl. Fusion*, 34(9):1221, 1994.

[7] ITER physics basis. *Nucl. Fusion*, 39:2137, 1999.

[8] Summary of the ITER final design report. *ITER EDA Documentation Series No 22 (Vienna: IAEA)*, 2001.

[9] F Wagner and et al. Regime of improved confinement and high beta in neutral-beam-heated divertor discharges of the ASDEX tokamak. *Phys. Rev. Lett*, 49: 1408, 1982.

[10] C. Kessel, J. Manickam, G. Rewoldt, and W. M. Tang. Improved plasma performance in tokamaks with negative magnetic shear. *Phys. Rev. Lett.*, 72:1212–1215, 1994.

[11] A C C Sips, for the Steady State Operation, and the Transport Physics topical groups of the International Tokamak Physics Activity. Advanced scenarios for ITER operation. *Plasma Phys. Contr. Fusion*, 47(5A):A19, 2005.

[12] F. M. Levinson. Improved confinement with reversed magnetic shear in TFTR. *Phys. Rev. Lett*, 75:4417, 995.

[13] E. J. Strait and et al. Enhanced confinement and stability in DIII-D discharges with reversed magnetic shear. *Phys. Rev. Lett*, 75:4421, 1995.

[14] O. Gruber and et al. Stationary-mode discharges with internal transport barrier on ASDEX Upgrade. 83:1787, 1999.

[15] T Fujita and the JT-60 Team. High-performance experiments towards steady-state operation in JT-60U. *Plasma Phys. Contr. Fusion*, 39:B75, 1997.

[16] J. W. Connor. A review of internal transport barrier physics for steady-state operation of tokamaks. *Nucl. Fusion*, 44:R1, 2004.

[17] M. Kikuchi. Steady state tokamak reactor based on the bootstrap current. *Nucl. Fusion*, 30(2):265, 1990.

[18] R. C. Wolf and et al. Stationary advanced scenarios with internal transport barrier on ASDEX Upgrade. *Plasma Phys. Contr. Fusion*, 41:B93, 1999.

[19] T. C. Luce and et al. Long pulse high performance discharges in the DIII-D tokamak. *Nucl. Fusion*, 41:1585, 2001.

[20] A. C. C. Sips. Steady state advanced scenarios at ASDEX Upgrade. *Plasma Phys. COntr. Fusion*, 44:B69, 2002.

[21] M. R. Wade and et al. Integrated, advanced tokamak operation on DIII-D. *Nucl. Fusion*, 43:634, 2003.

[22] G. T. A. Huysmans and et al. Mhd stability of optimized shear discharges in JET. *Nucl. Fusion*, 39:1489, 1999.

[23] Yueqiang Liu, A. Bondeson, Y. Gribov, and A. Polevoi. Stabilization of resistive wall modes in ITER by active feedback and toroidal rotation. *Nucl. Fusion*, 44: 232, 2004.

[24] F. Troyon, R. Gruber, H¿ Saurenmann, S. Semenzato, and S. Succi. MHD-limits to plasma confinement. *Plasma Phys. Contr. Fusion*, 26:209, 1984.

[25] R. D. Stamburgh and et al. *Plasma Phys. Contr. Fusion Research Conf. (London 1984)*, 1:217, 1984.

[26] E. J. Strait. Stability of high beta tokamak plasmas. *Phys. Plasmas*, 1:1415, 1994.

[27] D. Pfirsch and H. Tasso. A theorem on MHD-instability of plasmas with resistive walls. *Nucl. Fusion*, 11:259, 1971.

[28] A. M. Garofalo and et al. Stabilization of the external kink and control of the resistive wall mode in tokamaks. *Proc. 40th APS Conf. New Orleans*, 1998.

[29] M. S. Chu and M. Okabayashi. Stabilization of the external kink and the resistive wall mode. *Plasma. Phys. Contr. Fusion*, 52:123001, 2010.

[30] S. W. Haney and J. P. Freidberg. Variational methods for studying tokamak stability in the presence of a thin resistive wall. *Phys. Fluids B*, 1:1637, 1989.

[31] A. M. Garofalo and et al. Direct observation of the resistive wall mode in a tokamak and its interaction with plasma rotation. *Phys. Rev. Lett.*, 82:3811, 1999.

[32] H. Reimerdes and et al. Cross-machine comparison of resonant field amplification and resistive wall mode stabilization by plasma rotation. *Phys. Plasmas*, 13: 056107, 2006.

[33] A. C. Sontag and et al. Resistive wall mode stabilization of high-β plasmas in the National Spherical Torus Experiment. *Phys. Plasmas*, 12:056112, 2005.

[34] A. M. Garofalo and et al. Resistive wall mode dynamics and active feedback control in DIII-D. *Nucl. Fusion*, 41:1171, 2001.

[35] C. G. Gimblett and R. J. Hastie. The interaction of error fields and resistive wall modes. *Phys. Plasmas*, 11(3):1019, 2004.

[36] A. Bondeson and D. J. Ward. Stabilization of external modes in tokamaks by resistive walls and plasma rotation. *Phys. Rev. Lett.*, 72:2709, 1994.

[37] V. D. Shafranov. *Sov. Phys. Tech*, 15:175, 1970.

[38] R. Betti and J. P. Freidberg. Stability analysis of resistive wall kink modes in rotating plasmas. *Phys. Rev. Lett*, 74:2949, 1995.

[39] R. Fitzpatrick and A.Y. Aydemir. Stabilization of the resistive shell mode in tokamaks. *Nucl. Fusion*, 36:11, 1996.

[40] J. M. Finn. Stabilization of ideal plasma resistive wall modes in cylindrical geometry: the effect of resistive layers. *Phys. Plasmas*, 2:3782, 1995.

[41] R. Betti. Beta limits for the n=1 mode in rotating-toroidal-resistive plasmas surrounded by a resistive wall. *Phys. Plasmas*, 5:3615, 1998.

[42] A. Bondeson and H. X. Xie. Stability of ideal and resistive modes in cylindrical plasmas with resistive walls and plasma rotation. *Phys. Plasmas*, 4:2081, 1997.

[43] B. Coppi, R. Galvao, R. Pellat, M. N. Rosenbluth, and P. H. Rutherford. *Sov. J. Plasma Phys.*, 2:533, 1976.

[44] J. E. Rice and et al. Toroidal rotation and momentum transport in alcator c-mod plasmas with no momentum input. *Phys. Plasmas*, 11:2427, 2004.

[45] J. S. deGrassie, J. E. Rice, K. H. Burrell, R. J. Groebner, and W. M. Solomon. Intrinsic rotation in DIII-D. *Phys. Plasmas*, 14:056115, 2007.

[46] M. F. F. Nave and J. A. Wesson. Mode locking in tokamaks. *Nucl. Fusion*, 30: 2575, 1990.

[47] T. C. Hender and et al. Effect of resonant magnetic perturbations on COMPASS-C tokamak discharges. *Nucl. Fusion*, 32:2091, 1992.

[48] T. H. Jensen, A. W. Leonard, and A. W. Hyatt. A simple model for driven islands in tokamaks. *Phys Fluids B*, 5:1239, 1993.

[49] R. Fitzpatrick. Interaction of tearing modes with external structures in cylindrical geometry (plasma). *Nucl. Fusion*, 33:1049, 1993.

[50] R. Fitzpatrick. Bifurcated states of a rotating tokamak plasma in the presence of a static error-field. *Phys. Plasmas*, 5:3325, 1998.

[51] R. J. LaHaye and et al. Scaling of the critical plasma rotation for stabilization of the n = 1 resistive wall mode (ideal kink) in the DIII-D tokamak. *Nucl. Fusion*, 44, 2004.

[52] E. J. Strait and et al. Wall stabilization of high beta tokamak discharges in DIII-D. *Phys. Rev. Lett.*, 74:2483, 1995.

[53] E. J. Strait and et al. Resistive wall mode stabilization by slow plasma rotation in diii-d tokamak discharges with balanced neutral beam injection. *Phys Plasmas*, 14:056101, 2007.

[54] M. Takechi and et al. Identification of a low plasma-rotation threshold for stabilization of the resistive-wall mode. *Phys. Rev. Lett*, 98:055002, 2007.

[55] C. G. Gimblett and R. J. Hastie. *Theory of Fusion Plasmas*. Editrice Compositori, Bologna, 1999.

[56] R. Fitzpatrick. A simple model of the resistive wall mode in tokamaks. *Phys. Plasmas*, 9:3459, 2002.

[57] D. A. Gates and T. C. Hender. Resistive wall induced forbidden bands of mode rotation frequency on the COMPASS-D tokamak. *Nucl. Fusion*, 36:273, 1996.

[58] C. M. Bishop. An intelligent shell for the toroidal pinch. *Plasma Phys. Contr. Fusion*, 31:1179, 1989.

[59] C. G. Gimblett. Stabilization of thin shell modes by a rotating secondary wall. *Plasma Phys. Contr. Fusion*, 31:2183, 1989.

[60] R. Fitzpatrick and T. H. Jensen. Stabilization of the resistive wall mode using a fake rotating shell. *Phys. Plasmas*, 3:2641, 1996.

[61] P. Merkel, C. Nuhrenburg, and E. Strumberger. vol 28G (European Physical Society p-i208. *Proc. 31st EPS Conf. on Plasma Phyics (London, UK 2004) Paper EX/p9-8*, 2004.

[62] B. Hu and R. Betti. Resistive wall mode in collisionless quasistationary plasmas. *Phys. Rev. Lett.*, 93:105002, 2004.

[63] A. M. Garofalo and et al. Stability and control of resistive wall modes in high beta, low rotation DIII-D plasmas. *Nucl. Fusion*, 47:1121, 2007.

[64] H. Reimerdes and et al. Resistive wall mode stabilization in slowly rotating high beta plasmas. *Plasma Phys. Contr. Fusion*, 49:B349, 2007.

[65] M. Okabayashi and et al. Comprehensive control of resistive wall modes in DIII-D advanced tokamak plasmas. *Nucl. Fusion*, 49:125003, 2009.

[66] G. Matsunaga and et al. Dynamics and stability of resistive wall mode in the JT-60U high-β plasmas. *Proc. 22nd IAEA Fusion ENergy Conf. (Geneva Switzerland)(Vienna: IAEA) Paper EX/5-2*, 2008. URL `http://www-pub.iaea.org/MTCD/Meetings/FEC2008/ex_5-2.pdf`.

[67] G. Matsunaga and et al. Observation of an energetic-particle-driven instability in the wall-stabilized high-β plasmas in the JT-60U tokamak. *Phys. Rev. Lett*, 103: 045001, 2009.

[68] H. Reimerdes and et al. Reduced critical rotation for resistive-wall mode stabilization in a near-axisymmetric configuration. *Phys. Rev. Lett.*, 98:055001, 2007.

[69] S. A. Sabbagh and et al. The resistive wall mode and feedback control physics design in NSTX. *Nucl. Fusion*, 44:560, 2004.

[70] S. A. Sabbagh. Resistive wall stabilized operation in rotating high beta NSTX plasmas. *Nucl. Fusion*, 46:635, 2006.

[71] S. A. Sabbagh and et al. Active stabilization of the resistive-wall mode in high-beta, low-rotation plasmas. *Phys. Rev. Lett*, 97:045004, 2006.

[72] I. T. Chapman and et al. *Proc. 36th EPS Conf. on Plasma Physics, Sofia, P-5.133*, 2009.

[73] R. Hawryluk. Principle physics developments evaluated in the ITER design review. *Proc. 22nd IAEA Fusion Energy Conf. (Geneva Switzerland)(Vienna:*

IAEA)Paper IT/1-2, 2008. URL `http://www-pub.iaea.org/MTCD/Meetings/FEC2008/it_1-2.pdf`.

[74] E. Strumberger, P. Merkel, M. Sempf, and S. Gunter. On fully three-dimensional resistive wall mode and feedback stabilization computations. *Phys. Plasmas*, 15: 056110, 2008.

[75] Yueqiang Liu and et al. Modelling resistive wall modes with self-consistent inclusion of drift kinetic resonances. *Proc. 22nd IAEA Fusion Energy Conf. (Geneva Switzerland)(Vienna: IAEA)Paper TH/P9-26*, 2008. URL `http://www-pub.iaea.org/MTCD/Meetings/FEC2008/th_p9-26.pdf`.

[76] Z. Chang, J. D. Callen, E. D. Fredrickson, R. V. Budny, C. C. Hegna, K. M. McGuire, M. C. Zarnstorff, and TFTR group. Observation of nonlinear neoclassical pressure-gradient-driven tearing modes in TFTR. *Phys Rev Lett*, 74:4663, 1995.

[77] H. P. Furth, J. Killeen, , and M. N. Rosenbluth. Finite resistivity instabilities of a sheet pinch. *Phys Fluids*, 6:459, 1963.

[78] P. H. Rutherford. Nonlinear growth of the tearing mode. *Phys. Fluids*, 16:1903, 1973.

[79] R. Fitzpatrick. Helical temperature perturbations associated with tearing modes in tokamak plasmas. *Phys. Plasmas*, 2:825, 1995.

[80] R. D. Hazeltine, P. Helander, and P. J. Catto. Plasma transport near the separatrix of a magnetic island. *Phys. Plasmas*, 4:2920, 1997.

[81] A. I. Smolyakov. Nonlinear evolution of tearing modes in inhomogeneous plasmas. *Plasma Phys. Contr. Fusion*, 35:657, 1993.

[82] J. W. Connor, F. L. Waelbroeck, and H. R. Wilson. The role of polarization current in magnetic island evolution. *Phys Plasmas*, 8:2835, 2001.

[83] H. R. Wilson, J. W. Connor, R. J. Hastie, and C. C. Hegna. Threshold for neoclassical magnetic islands in a low collision frequency tokamak. *Phys. Plasmas*, 3:248, 1996.

[84] F. L. Waelbroeck, J. W. Connor, and H. R. Wilson. Finite Larmor raduis theory of magnetic island evolution. *Phys. Rev. Lett*, 87:215003–1, 2001.

[85] A. Bergman, E. Poli, and A. G. Peters. Collisionality dependence of the polarization current. *Phys. Plasmas*, 12:072501, 2005.

[86] R. Fitzpatrick, F. L. Waelbroeck, and F. Militello. The influence of the ion polarization current on magnetic island stability in a tokamak plasma. *Phys. Plasmas*, 13:122507, 2006.

[87] E. Lazzaro G. B. Re A. I. Smolyakov, A. Hirose and J. D. Callen. Rotating nonlinear magnetic islands in a tokamak plasma. *Phys. Plasmas*, 2:1581, 1995.

[88] S. P. Gerhardt and et al. Relationship between onset thresholds, trigger types and rotation shear for the $m/n = 2/1$ neoclassical tearing mode in a high-β spherical torus. *Nucl. Fusion*, 49:032003, 2009.

[89] R. J. LaHaye. Neoclassical tearing modes and their control. 13:055501, 2006.

[90] R. J. LaHaye, B. W. Rice, and E. J. Strait. Increasing the beta limit due to neoclassical tearing modes by raising the axial safety factor $q(0) > 1$. *Nucl. Fusion*, 40:53, 2000.

[91] A. Gude, S. Günter, S. Sesnic, and ASDEX Upgrade Team. Seed island of neoclassical tearing modes at ASDEX Upgrade. *Nucl. Fusion*, (39):127, 1999.

[92] O. Sauter and et al. Control of neoclassical tearing modes by sawtooth control. *Phys. Rev. Lett*, 88:105001, 20002.

[93] Empirical scaling of sawtooth period for onset of neoclassical tearing modes. 50 (10):102001, 2010.

[94] R. J. LaHaye, R. J. Buttery, S. Guenter, G. T. A. Huysmans, M. Maraschek, and H. R. Wilson. Dimensionless scaling of the critical beta for onset of a neoclassical tearing mode. *Phys. Plasmas*, 7:3349, 2000.

[95] D.A. Kislov and et al. Beta limit due to resistive tearing modes in T-10. *Nucl. Fusion*, (41):1619, 2001.

[96] D. P. Brennan and et al. A mechanism for tearing onset near ideal stability boundaries. *Phys. Plasmas*, (10):1643, 2003.

[97] P. Maget and et al. Modelling of (2,1) NTM threshold in JET advanced scenarios. *Nucl. Fusion*, 50:045004, 2010.

[98] J. Shiraishi and S. Tokuda. Analytic dispersion relation for resistive wall modes in rotating plasmas by generalized matching theory. *Nucl. Fusion*, 51:053006, 2011.

[99] C. G. Gimblett and R. J. Hastie. Torque balance and rotational stabilisation of the resistive wall mode. *Phys. Plasmas*, 7(1):258, 2000.

[100] C. G. Gimblett. On free boundary instabilities induced by a resistive wall. *Nucl. Fusion*, (26):617, 1986.

[101] H. R. Wilson, J. W. Connor, C. G. Gimblett, R. J. Hastie, and F. L. Waelbroeck. Theoretical understanding of tokamak pressure limits. *Proc. 18th Int. Conf. Sorrento, IAEA, Vienna,*, 2000. URL `www.iaea.org/programmes/ripc/physics/fec2000/html/node1.htm`.

[102] J. B. Taylor. Torque on an ideal plasma. *Phys. Rev. Lett*, 11(91):115002, 2003.

[103] J. L. Luxon and L. G. Davis. *Fusion Technol.*, 8:441, 1985.

[104] G. T. A Huysmans. Implementation of an iterative solver in the nonlinear MHD code JOREK. 2006. URL `http://aster.gforge.inria.fr/reports/huysmans_report_aster_002.pdf`.

[105] G. T. A Huysmans and O. Czarny. MHD stability in X-pomit geometry: simulation of ELMs. *Nucl. Fusion*, 7(47):659–666, 2007.

[106] G. T. A. Huysmans, S. Pamela, E. van der Plas, and P Ramet. *Plasma Phys. Cont. Fusion*, 12(51):124012, 2009.

[107] O. Czarny and G. T. A. Huysmans. Bézier surfaces and finite elements for MHD simulations. *J. Comp. Phys.*, 16(227):7423–7445, 2008.

[108] P. Hénon, P. Ramet, , and J. Roman. PaStiX: a high-performance parallel direct solver for sparse symmetric definite systems. *Parallel Computing*, 2(28):301–21, 2002.

[109] F. Pellegrini. Static mapping by dual recursive bipartitioning of process and architecture graphs. *Proceedings of SHPCC'94, Knoxville, Tennessee, IEEE Press*, pages 486–493, 1994.

[110] P. R. Amestoy, I. S. Duff, and J.-Y. L'Excellent. Multifrontal parallel distributed symmetric and unsymmetric solvers. *Comput. Methods in Appl. Mech. Eng.*, (184): 501–520, 2000.

[111] G. T. A. Huysmans and et al. *in Proc. CP90 Conf. on Computational Physics Proc. (World Scientific 1991)*, page 371.

[112] C. Hirsch. *Numerical computation of internal and external flows.*, volume 1. J. Wiley. ISBN 09780471924524.

[113] P. Merkel and M. Sempf. Feedback stabilization of resistive wall modes in the presence of multiply connected wall structures. *Proceedings of the 38th EPS*

Conference On Plasma Physics (Strasbourg, France), page 5.082, 2006. URL `http://ocs.ciemat.es/EPS2011PAP/pdf/P5.082.pdf`.

[114] E. Strumberger, P. Merkel, C. Tichmann, and S. Günter. Linear stability studies in the presence of 3D wall structures. *Proceedings of the 21st IAEA Fusion Energy Conference (Chengdu, China), TH/P3-8*, 2011. URL `http://www-naweb.iaea.org/napc/physics/FEC/FEC2006/papers/th_p3-8.pdf`.

[115] M. Hölzl, P. Merkel, G. T. A. Huysmans, E. Nardon, E. Strumberger, R. McAdams, I. T. Chapman, S. Günter, and K. Lackner. Coupling JOREK and STARWALL codes for non-linear resistive-wall simulations. *J. Phys. Conf. Ser.*, 401:012010, 2012.

[116] P. Hertout, C. Boulbe, E. Nardon, J. Blum, S. Brémond, J. Bucalossi, B. Faugeras, V. Grandgirard, and P. Moreau. The CEDRES++ equilibrium code and its application to ITER, JT-60SA and Tore Supra. *Fusion Engineering and Design: Proceedings of the 26th Symposium of Fusion Technology (SOFT-26)*, 86(6-8): 1045–1048, 2011.

[117] W Kerner, J.P Goedbloed, G.T.A Huysmans, S Poedts, and E Schwarz. CASTOR: Normal-mode analysis of resistive MHD plasmas. *J Comput Phys*, 142(2):271–303, 1998.

[118] Yueqiang Liu, R. Albanese, A. Portone, G. Rubinacci, and F. Villone. An analytical demonstration of coupling schemes between magnetohydrodynamic codes and eddy current codes. *Phys. Plasmas*, 15(7):072516, 2008.

[119] A. R. Polevoi and et al. *J. Plasma Fusion Res. SERIES*, v.5:82–87, 2002.

[120] S. H. Kim and et al. CORSICA simulations of ITER advanced operation scenarios. *Proc. 39th EPS Conf. Stockholm*, P5.089, 2012.

[121] G. Urquijo, M. Persson, and E.K. Maschke. Wall interaction of tearing modes in configurations with multiple rational surfaces. *Nucl. Fusion*, 34:1299, 1994.

[122] R. Fitzpatrick. Stability of coupled tearing and twisting modes in tokamaks. *Phys. Plasmas*, 1:3308, 1994.

[123] M. Persson. Wall locking and multiple nonlinear states of magnetic islands. *Plasma Phys, Contr. Fusion*, 36:1775, 1994.

[124] J. M. Finn and C. R. Sovinec. Nonlinear tearing modes in the presence of resistive wall and rotation. *Phys. Fluids*, 5:461, 1998.

[125] C. G. Gimblett and R. S. Peckover. *Proc. R. Soc. London, Ser. A*, 368:75, 1979.